

NORTHWESTERN UNIVERSITY

Problems in phase change thermodynamics and fluid instability:
application to anti-icing, Leidenfrost collapse, interfacial temperature,
and aortic aneurysms

A DISSERTATION

SUBMITTED TO THE GRADUATE SCHOOL
IN PARTIAL FULFILLMENT OF THE REQUIREMENTS

for the degree

DOCTOR OF PHILOSOPHY

Field of Mechanical Engineering

By

Tom Y. Zhao

EVANSTON, ILLINOIS

August 2021

© Copyright by Tom Y. Zhao 2021

All Rights Reserved

ABSTRACT

Problems in phase change thermodynamics and fluid instability: application to anti-icing, Leidenfrost collapse, interfacial temperature, and aortic aneurysms

Tom Y. Zhao

My research goal is to develop first principles frameworks to interrogate multiphase, multiscale systems. One of my main focus areas is to consistently deconstruct highly nonequilibrium problems into their fundamental components. By using analytical, computational and experimental tools to grasp the key levers controlling such phenomenon, I aim to build pipelines of research projects from a foundation upwards approach.

Specifically, my work addresses the key thermodynamic, instability, and molecular mechanisms that drive the nonequilibrium evolution of mechanical phenomenon. In many cases, these problems defy straightforward description because nanoscale effects cannot be assumed to “average out”. Instead, features at the smallest length and time scales often provide vital, deterministic contributions to the system at large. By adopting a nano-to-macro mode of analysis, I seek to formulate ab-initio design and diagnostic principles to control these systems. This paves the way for collaborative conceptualization, validation and application of novel process-structure-function paradigms in the development of

diagnostic platforms that forecast cardiovascular disease; the fine, predictive control of engineered surfaces to control the adjacent fluid phase; and the rational design of heat transfer systems based on nonlinear thermodynamic frameworks.

Acknowledgements

My dissertation is a collection of work completed with the help of multiple collaborators. Chapter 1 was done under the auspices of Dr. Paul Jones and Prof Neelesh Patankar. This chapter was first published in the journal Scientific Reports as *Zhao, T.Y., Jones, P.R. and Patankar, N.A. Thermodynamics of sustaining liquid water within rough icephobic surfaces to achieve ultra-low ice adhesion. Sci Rep 9, 258 (2019). <https://doi.org/10.1038/s41598-018-36268-5>*. Chapter 2 was a multi-year effort with Prof Neelesh Patankar and first appeared in the journal PNAS as *Zhao, T.Y., and Patankar, N.A. The thermo-wetting instability driving leidenfrost film collapse. Proceedings of the National Academy of Sciences, 117(24):13321, 06 2020*. Chapter 3 comprises on-going work with Prof Neelesh Patankar. Lastly, I worked with Guy Elisha, Sourav Halder, Dr. Ethan Johnson, Dr. Brad Allen, Prof Michael Markl, and Prof Neelesh Patankar on Chapter 4. The research in Chapter 1 and Chapter 2 was supported in part by the computational resources from the high performance computing facility (QUEST) at Northwestern University.

I would like to express my sincere appreciation for the many folks who have helped me along the way. I am indebted to Bruce Lindvall for launching my graduate career. He ushered me into a research lab when I was at a lost for what to do and wholeheartedly supported my bid for a PhD position when I was uncertain of my chances. I am grateful to Paul Jones for showing me firsthand how to be a good collaborator, a good supervisor,

and a good friend. At the lab, he methodically guided me through research. During our midnight drives to Argonne, he patiently guided me through life. I thank my advisor, Neelesh Patankar, for being my mentor over many years. His fiery passion for discovery has nourished an inextinguishable desire in me to keep exploring new problems and tackling new challenges. He taught me how to refine my nascent ideas into useful theories and how to conceptualize clearly while reaching for that breakthrough just on the edge of thought. I would like to thank Sinan Keten and Kenneth K.-C Park for their excellent instruction and their insightful contribution to my research. A significant part of my graduate work was based on the knowledge I gained from courses I've taken and lengthy discussions I've had with them. I am thankful to Shashank Acharya, who joined the lab around the same time as I did and has been an irreplaceable fixture in my graduate career. His laid back demeanor and willingness to help at a moment's notice are qualities I strive to emulate. I thank Guy Elisha, Sourav Halder, Nishant Nangia, Brennan Sprinkle, Namu Patel and Walter Kou for their help in my professional and personal life. I am grateful to Hermann Riecke for his support over many years. He taught me about math, persistence, and standing up after a fall.

Lastly, I thank my family: Hannah Han and Michael Zhao. They have laid a hand on my shoulder when I have stumbled. They have taught me about empathy, humility and sacrifice. Everything that I am and will be is because of them. Thank you, dad, for being my rock. Thank you, mom, for being my beacon in the dark.

Dedication

For Mum, Dad, and all the folks who helped me take one more step forward.

Table of Contents

ABSTRACT	3
Acknowledgements	5
Dedication	7
Table of Contents	8
List of Tables	10
List of Figures	12
Chapter 1. Anti-icing surfaces	31
1.1. Results and Discussion	38
1.2. Conclusions	54
1.3. Computational Methods	56
1.4. Acknowledgements	58
1.5. Author contributions statement	59
Chapter 2. Leidenfrost point	60
2.1. Film Instability	61
2.2. Verification by experiment and simulation	77
2.3. Conclusion	84

2.4. Additional information regarding film boiling on a vertical plate	85
2.5. Supporting Information (SI)	86
Chapter 3. Interface temperature	103
3.1. Introduction	104
3.2. The missing interface condition	106
3.3. The entropy condition at the two-phase interface	111
3.4. Results	123
3.5. Discussion	134
3.6. Conclusion	140
3.7. Methods	142
3.8. Author contributions	145
Chapter 4. Cardiovascular disease	146
4.1. Introduction	148
4.2. Vessel Instability	150
4.3. Methodology	166
4.4. Results and Discussion	171
4.5. Conclusion	178
4.6. Author Contributions	181
References	182

List of Tables

- | | | |
|-----|---|-----|
| 4.1 | study cohort characteristics | 168 |
| 4.2 | <p>Each physiological term that contributes to measuring the stability parameter $N_{\omega,sp}$ is tabulated for both patients and normal subjects—the patient’s aorta diameter A_b, oscillatory acceleration due to blood pressure $\bar{\phi}_\omega$, pulsatile contribution to wall shear β_b, and pulse wave velocity c_{pw}. The one-tailed Wilcoxon rank sum test was used to determine whether the larger median of one population (e.g. patients, $N_{\omega,sp} > 0$) is significantly greater than the smaller median of the other (e.g. patients, $N_{\omega,sp} < 0$). The row of p-values comparing patient and normal subject cohorts is colored red, while the row of p-values comparing $N_{\omega,sp} > 0$ and $N_{\omega,sp} \leq 0$ is colored blue. Rejection of the null hypothesis at the 5% level is colored purple.</p> | 174 |
| 4.3 | <p>The stability parameter $N_{\omega,sp}$ stratified by age and gender. The one-tailed Wilcoxon rank sum test was used to determine whether the larger median of one population (e.g. patients, Age < 40, female) is significantly greater than the smaller median of the other (e.g. normal subjects, Age < 40, female). The row of p-values comparing patient and normal subject cohorts is colored red, while the row of p-values</p> | |

comparing genders is colored blue. The row of p-values comparing each age group is colored green; note that the p-value beneath $\text{Age} < 40$ tests the age groups $\text{Age} < 40$ and $40 \leq \text{Age} < 60$, the p-value beneath $40 \leq \text{Age} < 60$ tests the age groups $40 \leq \text{Age} < 60$ and $40 \leq \text{Age}$, and the p-value beneath $60 \leq \text{Age}$ tests the age groups $60 \leq \text{Age}$ and $\text{Age} < 40$. Rejection of the null hypothesis at the 5% level is colored purple. 179

List of Figures

- 1.1 The critical pore radii (R_{crit}^{IL} , R_{crit}^{LV} and R_{crit}^{IV}) for phase equilibrium between liquid, ice or vapor at $p_C = 1$ atm as a function of temperature. The critical confinement length scale for freezing R_{IL} is the most restrictive of the three possible two-phase equilibria; a robust anti-icing surface must therefore satisfy $R < R_{IL}$. To compare the order of magnitude values of the three critical confinement length scales, the material contact angles are taken to be the same for simplicity ($\theta_{LV} = \theta_{IV} = \theta_{IL} = 120^\circ$). The actual relationship among the intrinsic contact angles is established subsequently using molecular dynamics. 39
- 1.2 The intrinsic ice-liquid contact angle θ_{IL} of a material as a function of its intrinsic liquid-vapor contact angle θ_{LV} . θ_{IL} is computed at $T = 255$ K, $p_C = 1$ atm, while θ_{LV} is computed at $T = 300$ K, $p_C = 1$ atm, both using equations (1.11), (1.12). The error bars denote three standard errors. 40
- 1.3 Molecular dynamics simulation of confined liquid water stabilized in a 5 nm diameter cylindrical pore on a substrate with $\theta_{LV} = 120.2^\circ$ (computed at $T = 300$ K) and $\theta_{IL} = 134.0^\circ$ (computed at $T = 255$ K). $T = 255$ K, and $p_C = 1$ atm. Cross-sections of the simulations are

presented in **a** and **b**. In trajectory **a**, ambient ice (blue) is initially placed adjacent to a textured substrate (grey). In the cylindrical pore, the ice melts passively, producing amorphous glass (yellow) and liquid water (red) within the pore. In trajectory **b**, liquid water is initially placed adjacent to a textured substrate, where an ice nucleus is artificially introduced to initiate growth of the ice phase. The pore is initially empty with a liquid meniscus intruding from the bulk phase; the pore wall is curved compared to the adjacent substrate material. Inside the pore, the water does not freeze, instead remaining in the metastable liquid phase. Phases (lattice ice, amorphous glass, liquid) were colour coded using the CHILL algorithm [20].

44

1.4 Change in free energy ΔG as a function of the vertical distance between the centers of mass of the ambient ice and the substrate. Cross-sections of the corresponding states in the molecular dynamics simulations are included for clarity. For a flat surface, there is a single global energy minimum for which ambient ice is attached to the surface. For porous surfaces, there are multiple local energy minima and a global energy minimum corresponding to ambient ice detached from the substrate and the initially confined phase evacuated from the pore. The wall of the empty pore associated with the global energy minimum is curved compared to the adjacent substrate material. $T = 255$ K, $p_C = 1$ atm, $\theta_{LV} = 120.2^\circ$ (computed at $T = 300$ K), $\theta_{IL} = 134.0^\circ$ (computed at $T = 255$ K). The heights of the pores are 7 nm. Metadynamics is carried

out from 20 statistically independent initial conditions to reconstruct ΔG . The mean is the black curve and three standard errors is given by the cyan region. 46

1.5 Strength of ice adhesion for cylindrical pores embedded in an icephobic substrate, compared with that for a flat surface (radius = 0 nm). $T = 255$ K, $p_C = 1$ atm, $\theta_{LV} = 120.2^\circ$ (computed at $T = 300$ K), $\theta_{IL} = 134.0^\circ$ (computed at $T = 255$ K). The error bars denote three standard errors. Cross-sections of molecular dynamics simulations with the corresponding pore diameters are included for clarity; the visualized snapshots correspond to equilibrium conditions before shear is applied. 50

1.6 (a) Periodic array of cylindrical nanopillars arranged in a 5 by 5 grid. The radius of each pillar in this particular array is 2 nm, the spacing is 2.5 nm (defined as the radius of the inscribed circle in the projected area between four adjacent pillars). (b) A cross-sectional view of two adjacent nanopillars and the confined liquid water in the space between texture. $T = 255$ K, $p_C = 1$ atm, $\theta_{LV} = 120.2^\circ$ (computed at $T = 300$ K), $\theta_{IL} = 134.0^\circ$ (computed at $T = 255$ K). 52

1.7 Strength of ice adhesion vs. radius and spacing (defined as the radius of the inscribed circle in the projected area between four adjacent pillars) of pillars in a periodic array. The height of each pillar is 2 nm. $T = 255$ K, $p_C = 1$ atm, $\theta_{LV} = 120.2^\circ$ (computed at $T = 300$ K), $\theta_{IL} = 134.0^\circ$ (computed at $T = 255$ K). The strength of ice adhesion for a flat surface is 96.75 kPa. The red circles correspond to simulation results; design of

experiments was carried out using latin hypercubes. The exact strength of adhesion values are shown in Supplementary Fig. S13.

53

1.8 Strength of ice adhesion for pillars with and without defect (**a**) and as a function of pillar height (**b**). $T = 255$ K, $p_C = 1$ atm, $\theta_{LV} = 120.2^\circ$ (computed at $T = 300$ K), $\theta_{IL} = 134.0^\circ$ (computed at $T = 255$ K). The error bars denote three standard errors. A top down cross-section of the molecular dynamics simulation with a defect is included for clarity; the visualized snapshot corresponds to equilibrium conditions before shear is applied.

54

2.1 Film boiling on a vertical plate, with the coordinate system delineated. The film thickness is denoted by $\bar{\delta}(x)$

62

2.2 **The stability of the perturbed solution.** **a.** The variation of $\text{Re}(i\omega)$ with π_{LP} and the dimensionless wavenumber k'' for $\Pi_{LB\sigma_{LV}} = 2 \times 10^{-9}$ and $Ja = 0.1$. A critical $\pi_{LP,crit}$ can be defined, for which lower values lead to unconditional stability, and greater values allow the coexistence of stable and unstable zones. **b.** The Jakob number vs the critical $\pi_{LP,crit}$, as predicted by the numerical solution to the full stability solution (eqn. 2.37) and by taking $\pi_{LP,crit}$ to occur at $k'' = 1$ (eqn: 2.39). The agreement is excellent. **c** The marginal stability curves are calculated by taking the locus of points where the real value of $i\omega$ changes sign. The diffusive expression (eqn. 2.38) is a good approximation for small Jakob numbers.

74

- 2.3 The Leidenfrost temperature vs the contact angle for water, from experiments [58, 42, 59, 41, 60], the diffusive prediction of the LFP (eqn. 2.43) and molecular dynamics simulations from this work. The equilibrium separation H_{SVL} and its variation associated with changes in the contact angle $\frac{dH_{SVL}}{d\theta}$ can be estimated from experimental data [61, 53]. Typical errors in the LFP and the contact angle measured from experiment are around 5°C and 2° respectively, though many sources do not explicitly report an error value for either quantity. The data point corresponding to a contact angle of 160° from Vakarelski et al. corresponds to the only surface which was textured with nanoparticles to achieve superhydrophobicity; the other data points correspond to flat surfaces with random roughness. 79
- 2.4 Molecular dynamics simulation of vapor film formation adjacent to a heated surface. The system is pressurized at 1 atm. 80
- 2.5 The dimensionless criterion $\pi_1 = 6$ as a low contact angle approximation from the diffusive expression (eqn. 2.43) captures the LFP data from experiment to within 5% error. The dimensionless number π_1 encapsulates the stabilizing effects of evaporative phase change (vapor mass generation), surface tension and viscous transport, while the critical value at which the LFP occurs describes the destabilizing role of the van der Waals interaction for low contact angle fluids. Experimental LFP and fluid property data are available for acetone, ethanol, pentane,

- R134a, nitrogen, RC318, benzene, helium, R11, R113, liquid sodium and liquid potassium [65, 66, 67, 68, 69, 70, 43, 124, 56, 57, 71] 82
- 2.6 The LFP from experimental data of R113, R12, hexane and nitrogen at different pressures (o's) normalized by the critical pressure p_c of the fluid [72, 73, 74] vs the predictive ability of the small contact angle angle approximation (eqn. 2.49) to the diffusive expression (eqn. 2.43). 83
- 2.7 The equilibrium contact surface separation for the fluid (alkanes), surface (gold) and the heterogeneous value corresponding to the Leidenfrost point. Note that the equilibrium separation H_{LVL} is reported at the respective Leidenfrost temperatures of each alkane species, whereas Drummond et. al. listed H_{LVL} at the same temperature. The temperature dependence of H_{SVS} is assumed to be small over the range of temperatures corresponding to the LFP of the alkane series [85, 86], which is much lower than the melting point of gold. 91
- 2.8 Residence time and frequency of liquid-solid contact in X-ray imaging [103]. 96
- 2.9 The Leidenfrost temperature vs the contact angle for water, from experiments [58, 42, 59, 41, 60], the diffusive prediction of the LFP (eqn. 2.43), molecular dynamics simulations from this work, and the corresponding states correlation (eqn. 2.67) 99
- 3.1 Finite, one-dimensional system with two fluid components A and B . The interface between the two phases is located at $x = d[t]$. A

motionless wall bounds the domain at $x = 0$, and a moveable piston at $x = L[t] + d[t]$ controls the pressure in the system. The wall is held at constant temperature T_W and the piston at temperature T_P . The radius of curvature of the interface R can be nonzero.

106

3.2

The components of the entropy production rate at the two phase interface are plotted as a function of the liquid and vapor side interface temperatures. The width of the vapor and liquid domains are both 1 mm. The piston cooling the liquid reservoir is held at a constant temperature 350 K and pressure 7.3×10^3 Pa, while the wall temperature heating the vapor is 389.4 K. **A)** The entropy production rate Δ_{LV} (eqn. 3.24) at the liquid-vapor interface reaches a maximum for finite values of the interface temperatures T_{SV} and T_{SL} . **B)** The first component of the entropy production rate Δ_1 arises from the difference in phase entropies between the liquid and vapor. This term decreases for larger values of T_{SV} and T_{SL} . **C)** The second component of the entropy production rate Δ_2 reflects the kinetic energy contribution. Due to the small mass flux \dot{m} relative to the other quantities, this term is negligible. **D)** The third component of the entropy production rate Δ_3 is due to heat transfer from the interface. This term increases for larger values of T_{SV} and T_{SL} . The opposite dependencies of Δ_1 and Δ_3 on T_{SV} and T_{SL} allow the interfacial entropy production rate to reach a maximum value at finite temperatures. The vapor and liquid properties of water (thermal conductivities, latent heat of phase change, etc.) as a function of

temperature and pressure were referenced from the IAPWS formulation [136, 137, 124].

117

3.3

The components of the entropy production rate at the two phase interface are plotted as a function of the liquid and vapor side interface temperatures. The width of the vapor and liquid domains are both 1 mm. The piston cooling the liquid reservoir is held at a constant temperature 350 K and pressure 7.3×10^3 Pa, while the wall temperature heating the vapor is 389.4 K. **A)** The entropy production rate Δ_{LV} (eqn. 3.24) at the liquid-vapor interface is negative for interface temperatures T_{SV} and T_{SL} away from the maximum. These states are not thermodynamically accessible, but can be reached transiently under local violation of the second law of thermodynamics. **B)** The first component of the entropy production rate Δ_1 arises from the difference in phase entropies between the liquid and vapor. This term drives Δ_{LV} for larger values of T_{SV} and T_{SL} . **C)** The second component of the entropy production rate Δ_2 reflects the kinetic energy contribution. Due to the small mass flux \dot{m} relative to the other quantities, this term is negligible. **D)** The third component of the entropy production rate Δ_3 is due to heat transfer from the interface. This term drives Δ_{LV} for smaller values of T_{SV} and T_{SL} . The vapor and liquid properties of water (thermal conductivities, latent heat of phase change, etc.) as a function of temperature were referenced from the IAPWS formulation [136, 137, 124].

120

3.4 The entropy evolution at the interface (eqn. 3.26) normalized by the maximum value ($\Delta_{LV}^{\prime s} = \frac{\Delta_{LV}^s}{\max(\Delta_{LV}^s)}$) as a function of the normalized interface temperature T'_S . The entropy production rate Δ'_C reaches a maximum between $T'_S = 1$ (the wall temperature) and $T'_S = 0$ (the saturation temperature) due to opposing dependencies between the mass flux and the difference in phase free entropies on the interface temperature. The temperature corresponding to the maximum $\Delta_{LS}^{\prime s}$ drops towards the saturation value as the distance d between the wall and interface increases to macroscale lengths. The vapor and liquid properties of water (thermal conductivities, latent heat of phase change, etc.) as a function of temperature were referenced from NIST[124]. The boundary conditions and location were set to $L = 0.1$ m, $T_{\text{wall}} = 550$ K, $T_{\text{sat}} = 373.15$ K, $p_P = 1$ atm. Linear temperature profiles are assumed in the liquid and vapor domains. 121

3.5 The evolution of liquid and vapor side interface temperatures as a function of the interface distance d from the superheated wall, predicted by the maximum entropy rate principle proposed in this work and measured via MD. The temperatures as averaged over 6 molecular dynamics simulations from independent initial conditions are well captured by maximizing the interfacial entropy production rate at each time step. The vapor and liquid properties of water (thermal conductivities, latent heat of phase change, etc.) as a function of temperature were referenced from literature [136, 137, 124]. The

boundary conditions were $T_W = 575$ K, $T_P = 350$ K, $p_P = 1$ bar. Linear temperature profiles were assumed in the liquid and vapor domains. 124

3.6 The temperature profiles in the vapor and liquid phases were measured using molecular dynamics (MD) for a system being superheated on the vapor side wall to $T = 575$ K and cooled on the liquid side piston to $T = 350$ K. The piston applies a pressure of 1 bar. The assumption of linear temperature profiles incurs error in calculating the heat fluxes for both phases. However, it is the lowest order model that does not require additional knowledge of the system outside of the applied boundary conditions. Additionally, the interface temperatures calculated by maximizing the entropy production rate at the interface while assuming linear profiles are adequate in capturing the values measured by MD. The vapor and liquid properties of water (thermal conductivities, latent heat of phase change, etc.) as a function of temperature were referenced from the IAPWS formulation [136, 137, 124]. 126

3.7 The evolutionary time scale of the interface $\tau_{E,c}$ as well as the diffusive time scale $\tau_{D,c}$, $c \in L, V$ of each phases were measured using molecular dynamics (MD) for a system being superheated on the vapor side wall to $T = 575$ K and cooled on the liquid side piston to $T = 350$ K. The piston applies a pressure of 1 bar. The diffusive time scales in both phases are orders of magnitude smaller than evolution time of the interface, such that the system can be considered as quasi-steady relative to the interfacial temperatures. The time scales associated with

the speed of sound were also reported to show that both phases were not caught in the ballistic regime. The vapor and liquid properties of water (thermal conductivities, latent heat of phase change, etc.) as a function of temperature were referenced from the IAPWS formulation [136, 137, 124].

127

3.8 **A)** The temperature profile of an ice-liquid system as measured via molecular dynamics by Wang et al[131] using the mW water model and as calculated by the maximum entropy production interface condition proposed in this work. The boundary condition in the liquid water has been chosen at a location closer to the interface in order to better estimate the interfacial heat flux. Note that molecular dynamics places the interface temperature $T_{SL,MD} \approx T_{SI,MD} \approx 267$ K to be 15 K greater than the boundary temperatures $T_{BC} \approx 250$ K but around 7 K less than the freezing point of mW water $T_F = 274.6$ K. The temperature distribution is non-monotonic and yet cannot be approximated accurately by the saturation temperature assumption.**B)**

The interfacial entropy production rate exhibits a maximum value at $T_{SL}^* = 265.2$ K, $T_{SI}^* = 263.1$ K. The ice and liquid properties of water (thermal conductivities, latent heat of phase change, etc.) were drawn from the mW water properties reported by Wang et al. [131]. Linear temperature profiles were assumed in the liquid and ice domains.

129

3.9 **A)** The temperature profile of an ice-liquid system as measured via molecular dynamics by Wang et al[131] using the mW water model and

as calculated by the maximum entropy production interface condition proposed in this work. Note that molecular dynamics places the interface temperature $T_{SL,MD} \approx T_{SI,MD} \approx 267$ K to be 15 K greater than the boundary temperatures $T_{BC} \approx 250$ K but around 7 K less than the freezing point of mW water $T_F = 274.6$ K. The temperature distribution is non-monotonic and yet cannot be approximated accurately by the saturation temperature assumption.**B)** The interfacial entropy production rate exhibits a maximum value at $T_{SL}^* = T_{SI}^* = 263.2$ K. The ice and liquid properties of water (thermal conductivities, latent heat of phase change, etc.) were drawn from the mW water properties reported by Wang et al. [131]. Linear temperature profiles were assumed in the liquid and ice domains. 130

3.10 **A)** The experimental temperature profile [114] of a two phase water system is well described by the predicted interface temperatures for the liquid (T_{SLM}) and vapor (T_{SVM}) side using the maximum entropy principle. The interface is located at $x = 0$ micron, where a pronounced temperature jump creates a non-monotonic temperature distribution such that T_{SL} is not bounded by the liquid or vapor temperatures in the far field.**B)** The interfacial temperature jump is well described by the maximum entropy principle. Only data sets that provided all necessary information such as boundary conditions, distances to the interface, etc. were included in the plot to avoid using any unknown properties to 'fit' the data. Linear temperature profiles were assumed in the liquid

and vapor domains. The vapor and liquid properties of water and octane (thermal conductivities, latent heat of phase change, etc.) as a function of temperature were referenced from the IAPWS formulation [136, 137, 124].

132

- 3.11 **A)** The experimental temperature profile [114] of a two phase water system is well described by the predicted interface temperatures for the liquid (T_{SLM}) and vapor (T_{SVM}) side using the maximum entropy principle. The interface is located at $x = 0$ micron, where a pronounced temperature jump creates a non-monotonic temperature distribution such that T_{SL} is not bounded by the liquid or vapor temperatures in the far field.**B)** The interfacial temperature jump is well described by the maximum entropy principle. Only data sets that provided all necessary information such as boundary conditions, distances to the interface, etc. were included in the plot to avoid using any unknown properties to 'fit' the data. Linear temperature profiles were assumed in the liquid and vapor domains. The vapor and liquid properties of water and octane (thermal conductivities, latent heat of phase change, etc.) as a function of temperature were referenced from the IAPWS formulation [136, 137, 124].

133

- 3.12 **A)** The experimentally measured temperature jump as well as the distinct liquid and vapor side temperatures at the two-phase interface are captured by the maximum entropy principle. This general agreement between experiment and theory holds for evaporation (Exp # 1, 3, 7,

8, 9)[**132, 116, 133**] and condensation (Exp # 4, 5)[**116**] of water; evaporation of octane (Exp # 2) [**134**]; evaporation of water under turbulent conditions (Exp # 6) [**135**]; and evaporation of water heated on the vapor side (Exp # 10, 11, 12) [**113**].**B**) The average phase change rate at the interface in units of mass per area, per unit time drawn from the same experiments are also captured by the maximum entropy principle. Only data sets that provided all necessary information such as boundary conditions, distances to the interface, etc. were included in the plot to avoid using any unknown properties to 'fit' the data; data points that overlapped significantly in the plot were also excluded for clear visualization. The vapor and liquid properties of water and octane (thermal conductivities, latent heat of phase change, etc.) as a function of temperature were referenced from the IAPWS formulation [**136, 137, 124**].

134

3.13 The components of the maximum entropy production rate at the two phase interface are mapped onto the average interfacial pressure and temperature. The width of the vapor and liquid domains are both 1 mm. The piston cooling the liquid reservoir is held at a constant temperature of 350 K, while the wall temperature and piston pressure are varied.**A**) The maximum entropy production rate Δ_{LV} (eqn. 3.24) at the average interface temperature $(T_{SV}^* + T_{SL}^*)/2$ exhibits a global minimum at the intersection of the binodal, continuous interface temperature and zero mass flux curves.**B**) The term Δ_1 , which encapsulates the difference

in phase entropies, increases for larger average interface temperature and lower interface pressure. **C)** The second component of the entropy production rate Δ_2 reflects the kinetic energy contribution. Due to the small mass flux \dot{m} relative to the other quantities, this term is negligible. **D)** The third component of the entropy production rate Δ_3 is due to heat transfer from the interface. This term increases for lower interface temperature and higher pressure. The vapor and liquid properties of water (thermal conductivities, latent heat of phase change, etc.) as a function of temperature were referenced from the IAPWS formulation [136, 137, 124].

137

3.14 For octane, the components of the maximum entropy production rate at the two phase interface are mapped onto the average interfacial pressure and temperature. The width of the vapor and liquid domains are both 1 mm. The piston cooling the liquid reservoir is held at a constant temperature of 350 K, while the wall temperature and piston pressure are varied. **A)** The maximum entropy production rate $\Delta_{LV,\max}$ (eqn. 3.24) at the average interface temperature $(T_{SV}^* + T_{SL}^*)/2$ exhibits a global minimum at the intersection of the binodal, continuous interface temperature and zero mass flux curves. **B)** The term $\Delta_{1,\max}$, which encapsulates the difference in phase entropies, increases for larger average interface temperature and lower interface pressure. **C)** The second component of the entropy production rate $\Delta_{2,\max}$ reflects the kinetic energy contribution. Due to the small mass flux \dot{m} relative to the

other quantities, this term is negligible.**D)** The third component of the entropy production rate $\Delta_{3,\max}$ is due to heat transfer from the interface. This term increases for lower interface temperature and higher pressure. The vapor and liquid properties of water (thermal conductivities, latent heat of phase change, etc.) as a function of temperature were referenced from the literature [124, 142, 143].

138

3.15 The nonequilibrium properties at the two phase interface are mapped onto the average interfacial pressure and temperature. The distance of the interface from the wall d and the distance of the interface to the piston L are both 1 mm, corresponding to the widths of the vapor and liquid domains. The piston cooling the liquid reservoir is held at a constant temperature of 350 K, while the wall temperature and applied piston pressure are both varied.**A)** The temperature jump at the liquid vapor interface is generally nonzero. The interface temperature is only continuous along the black contour.**B)** The mass flux due to phase change across the interface is positive for evaporation and negative for condensation. No phase change occurs along the white contour.**C)** The logarithm of the maximum entropy production rate at each interface pressure and temperature shows that the global minimum is located at equilibrium on the binodal, where the continuous interface temperature and zero mass flux contours intersect. The point of intersection corresponds to a constant temperature profile equal to the far field piston temperature 350 K in the liquid domain.**D)** The wall

temperature T_W is varied from 274 K to 646 K at different pressures to obtain the phase diagrams of the interfacial temperature jump, mass flux and entropy production rate. The vapor and liquid properties of water (thermal conductivities, latent heat of phase change, etc.) as a function of temperature were referenced from the IAPWS formulation [136, 137, 124].

141

4.1 The distensible blood vessel is modeled as a one-dimensional system with internal pressure P and velocity u averaged across the radial direction r , which is normal to the centerline coordinate x . The interior area $A = \pi R^2$ varies as a function of both space x and time t .

150

4.2 The viscous factor β as a function of Womersley number w_0 . Here, β has been normalized by its value at $w_0=0$, corresponding to a parabolic velocity profile.

152

4.3 **A)** The marginal stability curve depicting the dispersion relationship between the dimensionless wave number k'' of the perturbation mode and the dimensionless parameter N_ω , which encapsulates the blood viscosity, vessel diameter, pressure driven acceleration, and viscous contribution under pulsatile waveform of the flow. For a give k'' , N_ω larger than the value on the marginal stability curve indicates that the system is unstable as the perturbation amplitude will grow, and vice versa. **B)** The imaginary component of the Floquet multiplier α on the marginal stability curve. For small wavenumbers k'' , $\alpha = 0$ indicates

that only harmonic cases are relevant. Near order one k'' , the system undergoes a Neimark-Sacker [163] or secondary Hopf bifurcation in which $0 < \alpha < 0.5$.

161

4.4 Cross-sectional areas and mean velocity field from 4D flow MRI of the aorta. (a) Time-averaged 3D geometry of the aorta. The red box marks the ascending aorta. The axes units are in cm; (b) Point cloud (in blue) showing the ascending aorta. The red curve shows the centerline, and the red boxes show the planes normal to the centerline. These planes are used to calculate the cross-sectional areas and mean velocities. The axes units are in cm; (c) An example of the aorta cross-section on a normal plane. Meshing is done using Delaunay triangulation to calculate the cross-sectional area at the normal plane. The axes units are in cm; (d) Variation of mean velocity as a function of time and length along the ascending aorta.

170

4.5 **A)** The maximum SOV diameter recorded during each clinical visit. The initial MRI was processed at year 0. **B)** The maximum MAA diameter recorded during each clinical visit. **C)** A phase diagram of patients with follow-up imaging data. The maximum growth rate of their MAA and SOV in (cm/year) are visualized with respect to theoretical prediction $N_{\omega,sp}$. If $N_{\omega,sp} > 0$, the patient's marker is labeled by "x". Otherwise, the data point is labeled by "∇". The circles indicate that the patient experienced a surgical outcome after their initial MRI at year 0. $N_{\omega,sp} > 0$ appears to correlate with larger growth rates for

the MAA and SOV. **D)** Each patient has been labeled according to whether $N_{\omega,sp} > 0$ accurately predicts a growth outcome, quantitatively categorized as exhibiting a growth rate in SOV or $MAA \geq 0.29$ cm/year. This threshold is considered an indication for more frequent surveillance as it lies outside the range of normal growth rates in the thoracic aorta. 172

4.6 **A)** The distribution of the stability parameter $N_{\omega,sp}$ in the patient and normal subject cohorts. The median physiomaerker value for the normal subject cohort is shown to be significantly ($p < 0.005$) smaller than that for the patient cohort, via a one-tailed Wilcoxon rank sum test. 178

CHAPTER 1

Anti-icing surfaces

Ice formation presents a persistent problem in processes where structures are subject to cold conditions. Ice buildup on aircraft wings can cause a 25% increase in drag and 90% reduction in lift [1], while ice accretion on wind turbines can decrease annual energy production by 17% [2]. Hence, there is a need for engineered surfaces that suppress ice formation and reduce ice adhesion.

Topologically textured superhydrophobic surfaces have been shown to reduce both ice nucleation and adhesion by enhancing liquid droplet roll-off and sustaining ambient ice on top of the texture [3]. However, surface defects and homogeneous nucleation can eventually trigger the formation of ice on the substrate [4]. Water can also condense and freeze or desublimates in between surface texture, leading to ice occupation of the roughness and significantly increasing ice adhesion to the material[5]. Lastly, de-icing cycles erode surface roughness and degrade the ice-repellency of the substrate [6]. A robust, icephobic design that minimizes ice adhesion to the surface must therefore ensure that ambient ice does not fill the space between surface texture by impalement or phase change, despite surface defects or damage.

De-icing a substrate has also been facilitated by introducing other species onto the surface. Liquid impregnated textured surfaces (LIS [7]) and slippery liquid-infused porous

surfaces (SLIPS [8]) can decrease ice adhesion by introducing a lubricant that more favorably wets a textured surface than water. In these methods, the lubricant must be constantly replenished.

Surface science approaches have largely focused on rough hydrophobic surfaces with the expectation that such surfaces would also be icephobic. However, hydrophobic surfaces are liquid-water-hating, which may not necessarily imply ice-hating. A fundamental understanding of icephobic characteristics is missing. We address this gap.

Our approach to designing anti-icing surfaces is founded on texturing a surface so that it is energetically favorable for ambient ice to melt in between roughness. This ensures one of two cases will occur: either the ambient ice remains unimpaled by resting on top of the surface roughness, or the ambient ice coexists in thermodynamic equilibrium with liquid water confined between texture. This surface design reduces ice adhesion permanently, remains robust against defects or damage, and does not require consistent application of an external species such as oils, lubricants or salts.

In this work, heterogeneous nucleation theory in the form of the Gibbs-Thomson equation gives the confinement length scale for which liquid water is stabilized between surface texture as a function of material properties and operating conditions [9, 10]. In this thermodynamic framework, a surface which can sustain liquid water as opposed to ice in confinement is characterized by having an ice-liquid contact angle greater than 90° . This provides a physical basis for defining the icephobicity of a material.

Molecular dynamics simulations are then used to examine the interface between the different water phases (ice, liquid, vapor) and a solid substrate to uncover the molecular origin of icephobicity. The relationship between the various intrinsic contact angles of

a substrate shows that both hydrophobic and hydrophilic substrates exhibit icephobic properties and can be textured appropriately to reduce ice adhesion.

Although pores enclosed entirely inside the substrate have been simulated with molecular dynamics,[11] this study examines periodic arrays of pores and pillars at the interface between ambient ice and the material substrate. The confinement length scales for two-phase equilibrium predicted from classical nucleation theory are shown to agree closely with simulation results for both types of texture at the interface, suggesting the underlying theoretical predictions may be generally applicable. We further elucidate how liquid water confined in equilibrium within surface roughness impact the physics of ice adhesion through an analysis of free energy and non-equilibrium steered molecular dynamics. These procedures inform the rational design of textured, icephobic surfaces that reduce ice adhesion to a minimum.

The mechanism for the reduction in ice adhesion is found to be due to the metastability of liquid water. We demonstrate that for icephobic surfaces sustaining confined liquid water, initiating cleavage of ice adhering to the textured surface activates a persistent force propelling the adhered ice away from the surface. This is due to the change in free energy associated with the phase transition of the liquid water to ice as it leaves confinement. As a result, the strength of ice adhesion to the textured surface is decreased by over a factor of twenty-seven from that to a perfectly smooth hydrophobic surface. A robust, de-icing surface exhibiting strong resistance to defects and damage can be achieved by texturing an icephobic substrate with deep pores or tall, periodic features with spacing below the prescribed critical confinement length scale.

1.0.1. Ice-Liquid Phase Equilibrium: Flat Surface

The critical confinement length scale below which liquid water is sustained in between surface texture can be determined from heterogeneous nucleation theory. The theory describes the change in free energy associated with the formation of an ice particle from ambient, liquid water near a solid surface.

The maximum change in free energy with respect to the change in radius of the ice particle ($\frac{d\Delta G}{dr} = 0$) gives the critical energy barrier that must be overcome for ice nucleation to occur (see the ‘‘Heterogeneous Nucleation’’ section of the Supporting Information):

$$(1.1) \quad \Delta G_{crit} = \frac{16\pi\sigma_{IL}^3}{3\rho_I^2\Delta h_F^2} \left(\frac{T_F}{T_F - T} \right)^2 g(\theta_{IL}),$$

where Δh_F is the enthalpy of fusion [12], T_F the bulk freezing temperature of water associated with the saturation pressure, and T the temperature of the liquid water in thermal equilibrium with the ice particle. The subscripts I, L, S denote the ice, liquid, and substrate, respectively, such that ρ_I is the density of ice [13] and σ_{IL} the ice-liquid surface energy. The term $g(\theta_{IL})$ (equation (S6)) is a function of the intrinsic ice-liquid contact angle θ_{IL} with the substrate surface. The critical radius of the ice particle corresponding to this energy barrier is:

$$(1.2) \quad r_{crit}^{IL} = \frac{2\sigma_{IL}}{\rho_I\Delta h_F} \left(\frac{1}{1 - T/T_F} \right).$$

Ice particles with radii smaller than the critical value ($r < r_{crit}^{IL}$) will disperse and remain in the liquid state, as the free energy decreases with a reduction of the particle radius. Ice

particles larger than the critical size ($r > r_{crit}^{IL}$) form nuclei that initiate crystal growth, as the free energy then decreases with increasing radius of the nuclei.

1.0.2. Ice-Liquid Phase Equilibrium: Cylindrical Pore

For simplicity, the surface texture considered will be a cylindrical pore on an otherwise flat, icephobic surface ($\theta_{IL} > 90^\circ$) adjacent to bulk ice. The subsequent analysis assumes that the height of the pore is much larger than its radius. Although the cylindrical pore is not a typical anti-icing surface roughness explored in current experiments, it will be shown later that the critical pore radius derived from considering a cylindrical geometry provides a good estimate of the critical confinement length scale for general surface texture. In addition, the cylindrical geometry of the pore is a meaningful approximation for porous substrates; the present study will show that porous surfaces can demonstrate robust de-icing performance, motivating their use in future anti-icing experiments.

For the cylindrical pore to sustain liquid water in thermodynamic equilibrium with the ambient ice phase, the pore radius R must be smaller than a critical value R_{crit}^{IL} to prevent the formation of solid nuclei in confinement that initiate growth of the ice phase. Geometric considerations for the largest possible ice particle existing in mechanical equilibrium in the cylindrical pore gives the Gibbs-Thomson equation [10]:

$$(1.3) \quad R_{crit}^{IL}(\theta_{IL}, T) = -r_{crit}^{IL} \cos(\theta_{IL}) = \cos(\theta_{IL}) \frac{2\sigma_{IL}}{\rho_I \Delta h_F} \left(\frac{1}{T/T_F - 1} \right)$$

where the contact angle θ_{IL} of the ice-liquid interface with the icephobic surface should be the equilibrium contact angle defined in equation (1.12). Therefore the confined phase

is liquid if R satisfies:

$$(1.4) \quad R < -r_{crit}^{IL} \cos(\theta_{IL}).$$

The confined phase is ice otherwise. This criterion for the pore radius enforces thermodynamic equilibrium between the confined liquid phase and the ambient ice. Ice particles do not nucleate in the confined liquid water inside the pore and ambient ice does not grow into the pore, instead forming a ice-liquid meniscus pinned at the top edge of the pore. This analysis is similar to that for liquid-vapor phase change presented earlier [14, 15].

R_{crit}^{IL} defines a critical confinement length scale informing the design of surface texture which passively sustains liquid water in between surface roughness as a function of the ambient temperature and pressure, as well as the intrinsic ice-liquid contact angle θ_{IL} of the substrate material. As will be demonstrated by molecular dynamics simulations, R_{crit}^{IL} not only applies to general pore geometries, but also to pillar-type texture.

1.0.3. Condensed Water-Vapor Phase Equilibrium: Cylindrical Pore

To explore other possible phase transition pathways that could result in ice filling the space between surface texture, we examine the coexistence condition between water vapor and condensed water (ice or liquid), which describes the condition for desublimation or condensation in confinement. The critical radius r_{crit}^{CV} of the ice or liquid nucleus in its surrounding vapor is [15, 16] :

$$(1.5) \quad r_{crit}^{CV} = \frac{2v_C \sigma_{CV}}{RT \log\left(\frac{p_V}{p_S}\right)}$$

where the subscript C denotes the condensed phase (ice or liquid) and the subscript V denotes the vapor. \bar{R} is the specific gas constant, v_C the specific volume, p_V the vapor pressure, and p_S the saturation vapor pressure at temperature T over the condensed phase. Mechanical equilibrium between the condensed phase and water vapor across a curved interface is described by the Young-Laplace equation:

$$(1.6) \quad r_{crit}^{CV} = \frac{2\sigma_{CV}}{p_V - p_C}.$$

Analogous to equation (1.3), the critical pore radius R_{crit}^{CV} to sustain confined vapor in a cylindrical pore is then given by:

$$(1.7) \quad R_{crit}^{CV} = -r_{crit}^{CV} \cos(\theta_{CV}).$$

Therefore, the equilibrium confined phase is vapor if the pore radius $R < R_{crit}^{CV}$. The confined phase is liquid or ice otherwise. Typically, p_V (vapor pressure) or p_C is known depending on whether the ambient phase outside of the pore is vapor or condensed water, respectively.

Figure 1.1 shows the dependence of R_{crit}^{CV} and R_{crit}^{IL} on temperature. For R_{crit}^{CV} , the ambient phase outside of the pore is assumed to be ice or liquid at $p_C = 1$ atm, and the confined phase is vapor; for R_{crit}^{IL} , the ambient phase is assumed to be ice, and the confined phase liquid. R_{crit}^{CV} then describes the confinement length scale below which condensed water will not fill the space between the surface roughness through impalement or phase change. Indeed, Supplementary Fig. S3 uses molecular dynamics to verify that ambient ice or liquid initially resting on top of the surface texture will not fill the pore if its radius $R < R_{crit}^{CV}$, since the confined vapor and ambient condensed water

outside the pore are in thermodynamic equilibrium. Note that a simplifying assumption is made to compare the order of magnitude values of the three critical confinement length scales: $\theta_{LV} = \theta_{IV} = \theta_{IL} = 120^\circ$. This does not hold true in general for a specific substrate; however, a relationship between these contact angles has not been established experimentally or computationally in the literature. The assumption is not made for subsequent analyses. Instead, this study will examine the relationship between the three intrinsic contact angles between using molecular dynamics.

The critical confinement length scale for the reverse case, in which ambient vapor outside the pore exists in equilibrium with the confined condensed phase, is shown in Supplementary Fig. S4; this length scale is highly sensitive to the supersaturation of the ambient vapor.

The critical confinement length scale for freezing R_{crit}^{IL} is the most restrictive of the possible pathways for confined ice to occupy the pore; any condensed phase that fills the pore from non-equilibrium events such as rain or cloud droplet impacts will freeze into confined ice if $R > R_{crit}^{IL}$. A robust design requires that the surface be icephobic and that the texture satisfy $R < R_{crit}^{IL}$ in order to prevent water from freezing in between surface roughness.

1.1. Results and Discussion

1.1.1. Icephobicity: Liquid Wettability and Molecular Origin

Due to the difficulty in measuring the ice-liquid contact angle experimentally, it is desirable to relate the intrinsic ice-liquid contact angle θ_{IL} (icephobic or icephilic) with the liquid-vapor contact angle θ_{LV} (hydrophobic or hydrophilic) of a substrate. Since both θ_{IL}

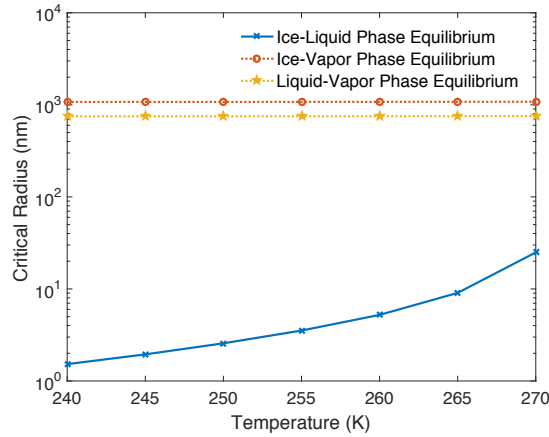


Figure 1.1. The critical pore radii (R_{crit}^{IL} , R_{crit}^{LV} and R_{crit}^{IV}) for phase equilibrium between liquid, ice or vapor at $p_C = 1$ atm as a function of temperature. The critical confinement length scale for freezing R_{IL} is the most restrictive of the three possible two-phase equilibria; a robust anti-icing surface must therefore satisfy $R < R_{IL}$. To compare the order of magnitude values of the three critical confinement length scales, the material contact angles are taken to be the same for simplicity ($\theta_{LV} = \theta_{IV} = \theta_{IL} = 120^\circ$). The actual relationship among the intrinsic contact angles is established subsequently using molecular dynamics.

and θ_{LV} are functions of temperature and pressure, the choice of ambient conditions may be somewhat arbitrary. We have chosen to compute θ_{IL} at $T = 255$ K and $p_C = 1$ atm, corresponding to the lower range of freezing depression induced by salts; and θ_{LV} at $T = 300$ K and $p_C = 1$ atm, corresponding to standard laboratory conditions. The contact angles were calculated from equation (1.12) by using molecular dynamics to determine the appropriate two-phase surface energies for a flat, planar interface [17]. This characterization of θ_{IL} offers insight into what makes a surface truly icephobic.

Figure 1.2 shows from our simulations that both hydrophilic and hydrophobic materials are icephobic. From a minimum $\theta_{IL} > 90^\circ$ at approximately neutral liquid wettability corresponding to $\theta_{LV} \approx 90^\circ$, the intrinsic θ_{IL} increases both as θ_{LV} increases towards

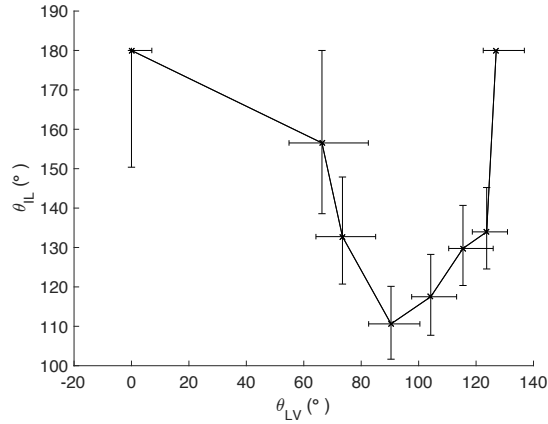


Figure 1.2. The intrinsic ice-liquid contact angle θ_{IL} of a material as a function of its intrinsic liquid-vapor contact angle θ_{LV} . θ_{IL} is computed at $T = 255$ K, $p_C = 1$ atm, while θ_{LV} is computed at $T = 300$ K, $p_C = 1$ atm, both using equations (1.11), (1.12). The error bars denote three standard errors.

180° and as θ_{LV} decreases to 0°. Supplementary Fig. S2 (a) shows that this icephobicity occurs due to the lower density of water in the contact layer (within 5 Å from the substrate surface) compared to bulk water density; water molecules favor positions in the bulk rather than at the interface with the solid substrate. This lower contact layer density penalizes the ice phase by deforming the lattice structure and introducing strain energy. On the other hand, the liquid phase exhibits significantly greater mobility in the contact layer compared to ice as indicated by the higher mean squared displacement $\langle u^2 \rangle$ of liquid water molecules (equation (S7)). This allows liquid water to achieve a lower, preferred interfacial density than the ice phase, even though the bulk density of liquid water is larger than that of ice. The favorability of liquid contact manifests in the ice-substrate surface energy exceeding the liquid-substrate surface energy for hydrophilic and hydrophobic materials, allowing both types of surfaces to sustain liquid water in between surface roughness. Similarly, Supplementary Fig. S1 shows that both hydrophobic and

hydrophilic surfaces can sustain vapor in confinement since the intrinsic ice vapor contact angle $\theta_{IV} \geq 90$.

The non-monotonic dependence of θ_{IL} on θ_{LV} may occur in part due to the higher viscosity of interfacial liquid water on hydrophilic surfaces compared to hydrophobic surfaces[18], which is corroborated by the drop in mobility of liquid water in the contact layer as θ_{LV} decreases (Supplementary Fig. S2). Li. et al. showed that this phenomenon increased the rate of ice nucleation on a hydrophobic surface by reducing the activation energy for diffusion of water molecules from the liquid to the ice phase. The change in both interfacial viscosity and density as θ_{LV} increases may result in a minimum difference in surface energy $\sigma_{IS} - \sigma_{LS}$ and a corresponding minimum in the ice-liquid contact angle θ_{IL} at neutral liquid wettability of the substrate.

1.1.2. Icephobicity: Freezing and Melting Point Hysteresis

The choice between hydrophilic and hydrophobic substrates in anti-icing applications is settled by the need for robustness. Although both hydrophilic and hydrophobic surfaces can sustain liquid water in confinement, it is known that hydrophilic materials like silica support hysteresis between the melting and freezing temperatures [19]; however, such hysteresis has not been observed experimentally for hydrophobic materials.

Supplementary Fig. S5 shows that for hydrophilic substrates, the confined melting temperature is higher than the freezing temperature, whereas the confined melting and freezing temperatures are equal for hydrophobic substrates. In the former case, the metastability of the confined ice may be attributed to the hydrophilic substrate providing

insufficient surface energy to overcome the volumetric energy barrier for melting; Supplementary Fig. S2 verifies that the surface energy of the substrate/ice interface is lower and the contact layer density higher for hydrophilic substrates compared to hydrophobic surfaces, such that the hydrophilic surface/ice interaction does not sufficiently perturb the local ice lattice to induce melting.

This phenomenon shows that the theoretically derived R_{crit}^{IL} from binodal coexistence accurately describes the confinement freezing and melting temperature for hydrophobic substrates. Although classical nucleation theory can also estimate the confinement freezing temperature of hydrophilic substrates, capturing the confinement melting temperature requires analysis of the spinodal metastability of the ice phase due to the demonstrated hysteresis effect. Thus, the use of hydrophilic substrates in anti-icing applications necessitates quantification of the confinement phase change hysteresis as a function of operating conditions and surface hydrophilicity, which is out of the scope of the current study.

1.1.3. Icephobicity: Critical Confinement Length Scale

For icephobic substrates, molecular dynamics demonstrates that if $R < R_{crit}^{IL}$ is satisfied, the liquid phase can exist between surface texture in equilibrium with the ambient ice. Figure 1.3 shows two molecular dynamics simulations identifying the equilibrium phase of water confined in a cylindrical pore on an icephobic substrate. Cross-sections are visualized to clarify the three-dimensionality of the system. Temperature and pressure are held constant at 255 K and 1 atm, respectively. The radius of the pore is chosen such that $R = 2.5 \text{ nm} < R_{crit}^{IL}$.

Initially for trajectory (1.3a), both the ambient and confined water are in the ice phase. Ambient ice on top of the surface remains frozen as time progresses, whereas ice inside the 5 nm diameter pore rapidly melts. Liquid water nucleates from the ice at the bottom of the pore and grows upward to the top of the cavity. The new state of the system persisted past 218 ns, the duration of the simulation.

Initially for trajectory (1.3b), both the ambient and confined water are in the liquid phase, although an ice nucleus is artificially introduced to accelerate the dynamics; this models ice accretion initiated by homogeneous nucleation [4]. Ambient liquid on top of the surface freezes as time progresses, whereas water inside the 5 nm diameter pore remains in the liquid phase. The new state of the system persisted past 10 ns, the duration of the simulation.

The equilibrium coexistence states were sampled in molecular dynamics by continuing the simulation well past the point where the count of molecules in the ice and liquid phases remains constant with time (chemical equilibrium), the temperature of both phases remain constant and equal (thermal equilibrium), and the ice-liquid contact angle with the vertical pore wall is constant (mechanical equilibrium).

These trajectories along with Supplementary Fig. S3 show that if the critical confinement length scale is satisfied by the surface texture, the space in between texture will be occupied by either liquid water or vapor. There is no equilibrium state where ice is confined in between roughness.

For two substrate materials with different θ_{LV} and θ_{IL} , Supplementary Table S1 and Fig. S7 show that the theoretical critical radii match well with simulation results. Molecular dynamics simulations also reveal that R_{crit}^{IL} can accurately predict liquid wetting in

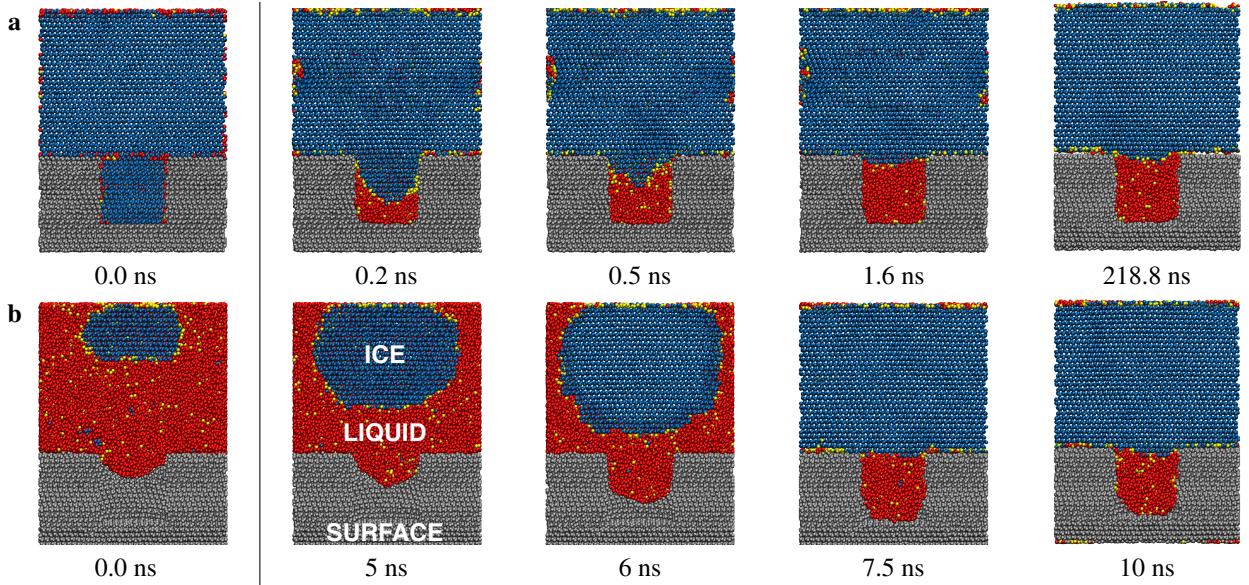


Figure 1.3. Molecular dynamics simulation of confined liquid water stabilized in a 5 nm diameter cylindrical pore on a substrate with $\theta_{LV} = 120.2^\circ$ (computed at $T = 300$ K) and $\theta_{IL} = 134.0^\circ$ (computed at $T = 255$ K). $T = 255$ K, and $p_C = 1$ atm. Cross-sections of the simulations are presented in **a** and **b**. In trajectory **a**, ambient ice (blue) is initially placed adjacent to a textured substrate (grey). In the cylindrical pore, the ice melts passively, producing amorphous glass (yellow) and liquid water (red) within the pore. In trajectory **b**, liquid water is initially placed adjacent to a textured substrate, where an ice nucleus is artificially introduced to initiate growth of the ice phase. The pore is initially empty with a liquid meniscus intruding from the bulk phase; the pore wall is curved compared to the adjacent substrate material. Inside the pore, the water does not freeze, instead remaining in the metastable liquid phase. Phases (lattice ice, amorphous glass, liquid) were colour coded using the CHILL algorithm [20].

surface texture as a function of the temperature (Supplementary Fig. S6). This agreement between theory and computation demonstrates the usefulness of R_{crit}^{IL} in specifying the critical confinement length scale for surface texture as a function of the material icephobicity θ_{IL} and the operating conditions.

Due to the latent heat of fusion released (positive enthalpy difference) with phase change from liquid water to ice, the presence of the liquid water in between the surface texture should make this equilibrium state metastable. We show subsequently that sustaining liquid water in between surface texture corresponds to a local energy minimum. It can be further shown that this metastability is useful in reducing the strength of ice adhesion to the surface.

1.1.4. Ice Adhesion: Metastability of the Liquid Water

We now wish to sample the energy landscape of the system in search of a possible global minimum away from the local minimum corresponding to confinement of liquid water in the pore. Metadynamics was used to reconstruct the free energy landscape in the space of a collective variable (CV) representing the vertical distance between the centers of mass of the ambient ice and the substrate [21]. The method uses a history dependent potential to bias the system away from local minima associated with particular values of the collective variable.

Note that the choice of the CV does not fully capture the complexity of de-icing pathways, which for instance can be expected to exhibit energy barriers in orthogonal shear directions or may involve some degree of interfacial premelting. Establishing a free energy landscape in the directions orthogonal to the ice/substrate interface necessitates the use of orthogonal CVs. Interfacial premelting occurs at low undercoolings and must be examined near the freezing point. Both analyses are outside the scope of this study.

Although the collective variable selected does not provide the most general description of possible ice/substrate dynamics, it does effectively describe the change in free energy

associated with the removal of the ambient ice from the substrate. The free energy landscape in the vertical direction is used to probe the existence of local vs global energy minima for porous surfaces, in contrast to the single global energy minimum expected for a flat substrate. Thus, the vertical distance between the centers of mass of the ambient ice and the underlying material is an appropriate choice for the collective variable in this context. The kinetics of ice detachment arising through shearing between the ambient ice and the substrate will be explored subsequently in this study using nonequilibrium simulations.

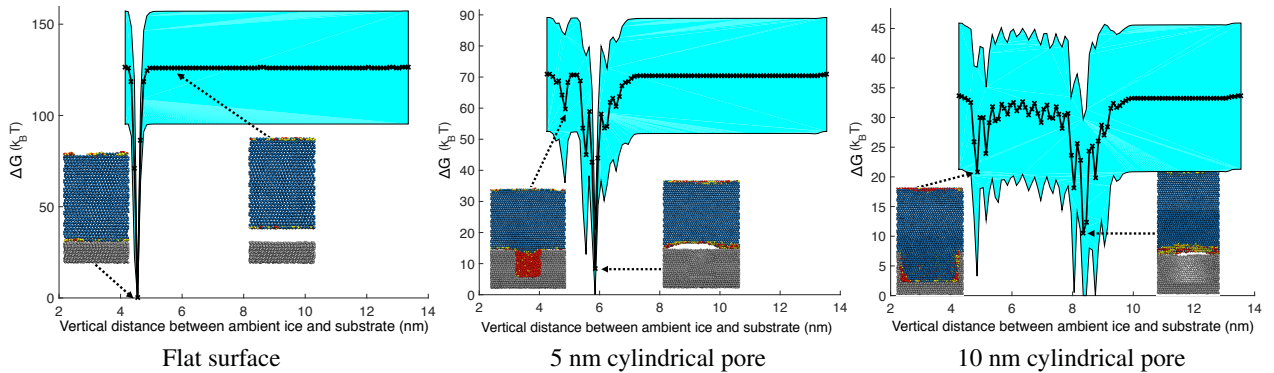


Figure 1.4. Change in free energy ΔG as a function of the vertical distance between the centers of mass of the ambient ice and the substrate. Cross-sections of the corresponding states in the molecular dynamics simulations are included for clarity. For a flat surface, there is a single global energy minimum for which ambient ice is attached to the surface. For porous surfaces, there are multiple local energy minima and a global energy minimum corresponding to ambient ice detached from the substrate and the initially confined phase evacuated from the pore. The wall of the empty pore associated with the global energy minimum is curved compared to the adjacent substrate material. $T = 255$ K, $p_C = 1$ atm, $\theta_{LV} = 120.2^\circ$ (computed at $T = 300$ K), $\theta_{IL} = 134.0^\circ$ (computed at $T = 255$ K). The heights of the pores are 7 nm. Metadynamics is carried out from 20 statistically independent initial conditions to reconstruct ΔG . The mean is the black curve and three standard errors is given by the cyan region.

Figure 1.4 shows the change in free energy as a function of the vertical distance between the centers of mass of the ambient ice and the substrate. The icephobic flat surface has a single, global energy minimum where the ambient ice is attached to the surface. To detach ambient ice from the substrate, a large external force must be applied to overcome the significant energy barrier in moving the system out of the global potential well into an unfavorable high energy state.

The 5 nm cylindrical pore satisfies $R < R_{crit}^{IL}$ and has a single, global energy minimum where the ambient ice phase has mostly detached from the icephobic substrate and the metastable liquid has frozen into ice after escaping the pore. The ambient ice adhering to the textured surface with the liquid water confined in the pore corresponds to a local energy minimum. To detach ambient ice from the substrate, a sufficient external force must be applied to overcome the small energy barrier separating the local energy minimum from the global potential well. As the ambient ice begins to cleave from the substrate, the liquid water adhering to the ambient ice escapes confinement and freezes. This initiated phase transition generates a force which drives the system down towards the global energy minimum, corresponding to the detached ice state.

Thus, the change in free energy elucidates the mechanism by which liquid water confined between surface texture reduces ice adhesion. Along with passively lubricating the interface, the liquid water confined in between surface texture actively does work in pushing ambient ice off the substrate as the metastable phase undergoes a freezing transition during the detachment process.

As the pore radius increases past the critical confinement length scale ($R \geq R_{crit}^{IL}$), the fraction of confined liquid water in the liquid phase decreases dramatically. For the 10 nm

cylindrical pore where confined water is dominated by the ice phase, the activation energy to move the system out of the local energy minimum corresponding to attached ambient ice is much larger than for the case in which the confined water is liquid. Additionally, the numerous local minima in the path between the attached and detached states means a consistent shear force must be applied to overcome a series of energy barriers; the mechanical interlocking of the confined ice and surface texture hinders removal of the ambient ice.

For a hydrophobic substrate, the vapor phase is preferred inside the pore compared to the liquid phase ($\sigma_{SV} < \sigma_{SL}$) from a surface energy perspective. One may thus be tempted to attribute the decrease in free energy associated with the detachment of the ambient ice from a porous substrate sustaining confined liquid water to this decrease in surface energy ($\sigma_{SV} - \sigma_{SL} < 0$). However, note that for an icephobic substrate, the liquid phase is preferred inside the pore compared to the ice phase ($\sigma_{SL} < \sigma_{SI}$). Based on this surface energy analysis, the detachment of the ambient ice from the substrate with the 10 nm cylindrical pore should therefore demonstrate the largest decrease in free energy, since the initial confined phase inside the pore is ice ($\sigma_{SV} - \sigma_{SI} < \sigma_{SV} - \sigma_{SL}$). However, this is not the case; the largest decrease in free energy occurs for porous substrates in which the confined phase is liquid. Thus, it is the phase transition of confined liquid water to ice that is responsible for producing the smallest energy barrier between the local (attached) and global (detached) energy minima for porous surfaces.

1.1.5. Ice Adhesion: Strength of Ice Adhesion

The strength of ice adhesion measures the stability of the ice/substrate interface under shear, and is a practical engineering metric to quantify the de-icing capabilities of engineered surfaces. It can be measured in experiments [22], which show that hydrophobic substrates with $\theta_{LV} \approx 120^\circ$ exhibit strength of ice adhesion around 160 kPa at -15°C . Using molecular dynamics, ambient ice in each system was sheared from the substrate at a constant velocity using a harmonic spring. One end of the spring was attached to the center of mass of the ambient ice while the other end was attached to a reference point at an equilibrium distance from the ice. The reference point is then displaced at a constant velocity, so that the force applied to the bulk ice in the shear direction is proportional to the spring deflection from the equilibrium distance (equation (S8)). The shear force was processed through a Gaussian filter to remove the high frequencies attributed to thermal fluctuations and the resonance frequency of the spring [23]. The strength of ice adhesion was taken to be the maximum shear force at which ambient ice detaches from the surface divided by the projected interface area.

Figure 1.5 shows that for the 5 nm diameter cylindrical pore in which the confined phase is completely dominated by liquid water, the strength of ice adhesion can be reduced by over a factor of four compared to that for the flat hydrophobic surface, which has roughness on the order of 2.8 Å. As the radius of the pore increases past R_{crit}^{IL} , the ice phase fills the pore. The mechanical interlocking between ice and the substrate for the 10 nm diameter pore leads to an increase in the strength of ice adhesion. Thus, textured surface can reduce or increase the strength of ice adhesion compared to a flat hydrophobic surface depending on whether the confined phase is liquid or ice, respectively.

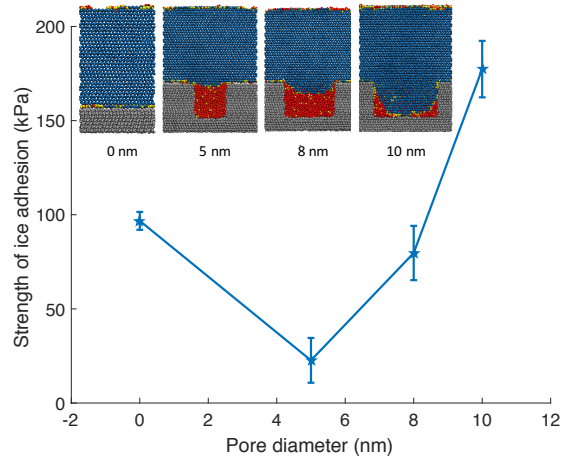


Figure 1.5. Strength of ice adhesion for cylindrical pores embedded in an icephobic substrate, compared with that for a flat surface (radius = 0 nm). $T = 255$ K, $p_C = 1$ atm, $\theta_{LV} = 120.2^\circ$ (computed at $T = 300$ K), $\theta_{IL} = 134.0^\circ$ (computed at $T = 255$ K). The error bars denote three standard errors. Cross-sections of molecular dynamics simulations with the corresponding pore diameters are included for clarity; the visualized snapshots correspond to equilibrium conditions before shear is applied.

The effect of pore geometry and hierarchical surface texture on the confinement length scale and the strength of ice adhesion is explored in Supplementary Fig. S8, S9, and S10. It is shown that although selecting triangular prisms for the pore geometry can reduce the strength of ice adhesion compared to cylindrical pores, manipulating pore geometry or hierarchical structure does not significantly change the critical confinement length scale.

Supplementary Fig. S12 depicts the ice detachment pathways as a function of liquid wettability. For hydrophobic substrates ($\theta_{IL} > 90^\circ$) with roughness satisfying $R \leq R_{crit}^{IL}$, the reduction in the strength of ice adhesion (Fig. 1.5) occurs when ice detachment is accompanied by dewetting of the texture. Since the ambient ice is effectively hydrophilic, the confined liquid will adhere to the ice rather than the hydrophobic texture during detachment. This de-icing pathway is therefore robust, and the reduction of ice adhesion

will occur reproducibly and generically for hydrophobic texture satisfying the critical confinement length scale.

For hydrophilic substrates ($\theta_{IL} < 90^\circ$), the texture may not necessarily dewet during ice detachment. Supplementary Fig. S11 shows that lubrication from liquid water confined in hydrophilic roughness satisfying $R \leq R_{crit}^{IL}$ can also reduce the strength of ice adhesion compared to that of a flat surface. For the roughness regime satisfying $R \gtrsim R_{crit}^{IL}$, Supplementary Fig. S12 shows that the shearing of the ambient ice induces melting of the confined ice near the walls of the pore; this local phase change causes a change in surface free energy which decreases ice adhesion to a greater extent than can be achieved with lubrication effects. For both the phase change pathway and the lubrication pathway, the confined water does not escape during de-icing. Thus, there is a fundamental difference between the ice detachment pathways for hydrophobic and hydrophilic substrates sustaining a confined phase.

1.1.6. Ice Adhesion: Periodic Surface Texture

The critical confinement length scale derived theoretically for cylindrical pores also applies reasonably for periodic arrays of icephobic, cylindrical pillars arranged on a substrate (Fig. 1.6). These periodic arrays can sustain a continuous film of liquid water, for which confinement is dictated by the spacing between roughness features.

Figure 1.7 shows the strength of ice adhesion as a function of the spacing and radius of the pillars in the periodic lattice. The spacing is defined as the radius of the inscribed circle in the projected area between four adjacent pillars. The strength of ice adhesion on a flat substrate with $\theta_{LV} = 120.2^\circ$ (computed at $T = 300$ K) and $\theta_{IL} = 134.0^\circ$ (computed

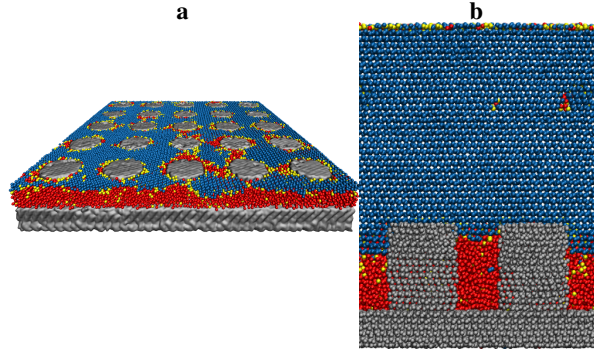


Figure 1.6. (a) Periodic array of cylindrical nanopillars arranged in a 5 by 5 grid. The radius of each pillar in this particular array is 2 nm, the spacing is 2.5 nm (defined as the radius of the inscribed circle in the projected area between four adjacent pillars). (b) A cross-sectional view of two adjacent nanopillars and the confined liquid water in the space between texture. $T = 255$ K, $p_C = 1$ atm, $\theta_{LV} = 120.2^\circ$ (computed at $T = 300$ K), $\theta_{IL} = 134.0^\circ$ (computed at $T = 255$ K).

at $T = 255$ K) at $T = 255$ K and $p_C = 1$ atm is 96.75 kPa, which is on the same order of magnitude as experimental values [22]. The strength of ice adhesion for the pillared surface is less than for the flat surface when the pillar spacing $\lesssim 4.5$ nm, which matches well with theory ($R_{crit}^{IL} = 3.8 \pm 0.7$ nm). Note from the isocontours that the strength of ice adhesion depends mainly on the spacing between pillars (confinement length scale) and is less sensitive to the pillar radius. Thus, R_{crit}^{IL} yields a general confinement length scale for the design of textured surfaces which can sustain liquid water in order to reduce ice adhesion.

The anti-icing performance of these surface textures is also robust to local defects. Figure 1.8 (a) shows a periodic array of pillars where one pillar is removed from the center of the lattice, introducing a defect that allows ambient ice to intrude into the

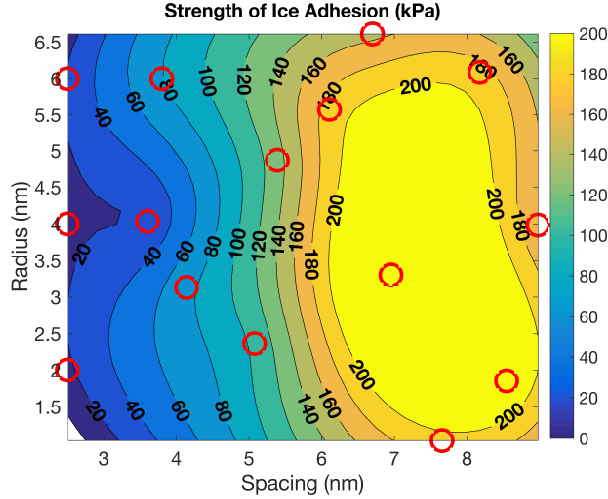


Figure 1.7. Strength of ice adhesion vs. radius and spacing (defined as the radius of the inscribed circle in the projected area between four adjacent pillars) of pillars in a periodic array. The height of each pillar is 2 nm. $T = 255$ K, $p_C = 1$ atm, $\theta_{LV} = 120.2^\circ$ (computed at $T = 300$ K), $\theta_{IL} = 134.0^\circ$ (computed at $T = 255$ K). The strength of ice adhesion for a flat surface is 96.75 kPa. The red circles correspond to simulation results; design of experiments was carried out using latin hypercubes. The exact strength of adhesion values are shown in Supplementary Fig. S13.

liquid film. However, due to the abundance of liquid water in adjacent period cells, the increase in the strength of ice adhesion is negligible.

As the height of the pillars increases, the strength of ice adhesion decreases due to the increase in the amount of liquid water confined in between surface texture, as demonstrated in Fig. 1.8 (b). Thus, periodic surface texture with the proper confinement length scale and sufficient depth can reduce the strength of adhesion by over a factor of twenty-seven compared to that for the flat hydrophobic surface. Since the strength of ice adhesion increases gradually as the height of the pillars decreases until the flat interface case is reached, the surface texture will continue to lower ice adhesion until it is completely destroyed. It is therefore desirable to engineer surfaces with tall texture or deep pores.

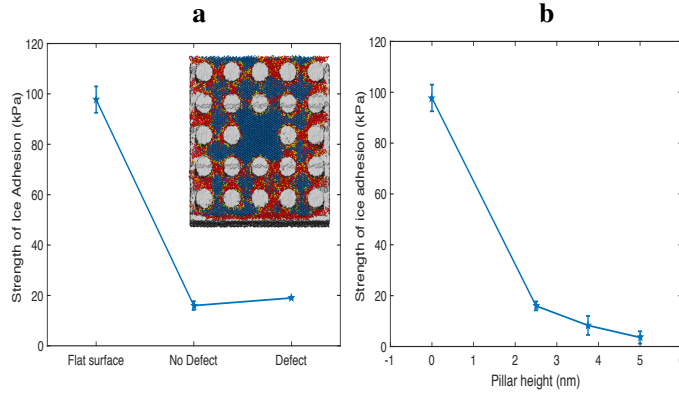


Figure 1.8. Strength of ice adhesion for pillars with and without defect (a) and as a function of pillar height (b). $T = 255$ K, $p_C = 1$ atm, $\theta_{LV} = 120.2^\circ$ (computed at $T = 300$ K), $\theta_{IL} = 134.0^\circ$ (computed at $T = 255$ K). The error bars denote three standard errors. A top down cross-section of the molecular dynamics simulation with a defect is included for clarity; the visualized snapshot corresponds to equilibrium conditions before shear is applied.

1.2. Conclusions

In this work, material icephobicity is physically characterized by the ice-liquid contact angle satisfying $\theta_{IL} > 90^\circ$. The molecular origin of icephobicity arises from the rigid structure and reduced mobility of ice compared to liquid water at the interface with a material substrate, which results in a higher ice-substrate surface energy relative to the liquid-substrate interface. With this physical understanding and quantification of icephobicity, substrates may be appropriately engineered to reduce ice-adhesion to an icephobic surface.

The critical confinement radius below which liquid water exists in thermodynamic equilibrium with the adjacent bulk ice phase can be derived theoretically as a function of the ambient conditions (temperature, pressure) and surface wettability. The confinement of metastable liquid in between surface texture corresponds to a local energy minimum;

as the ambient ice is sheared from the substrate, the liquid water escapes confinement and freezes, generating a detachment force driving the system to a global energy minimum where the ambient ice is mostly detached from the substrate. Icephobic surfaces textured according to the critical confinement length scale therefore undergo a permanent decrease in ice adhesion, either by the above mechanism or by ambient ice remaining suspended atop the surface roughness in the unimpaled state.

Surfaces that sustain liquid water in confinement are robust against local defects, which negligibly affects the global de-icing performance. As long as the confinement length scale is satisfied on average by the surface texture, the surface will continue to reduce ice adhesion until the texture is completely depleted. Porous or periodically textured surfaces are prime candidates for de-icing applications.

Materials with such properties include mesoporous zeolites and MOFs. A zeolite such as MCM-41 has pore diameters between 1 and 10 nm [24]; silylated MCM-41 has a liquid vapor contact angle of 133° [25]. Similarly, metallic organic frameworks such as MOF 5 have been polymerized to achieve liquid vapor contact angles of 135° [26], and carbonized to achieve pore diameters around 6 nm [27]. MOF pores are interconnected, but as the periodic surface textures show, a continuous film of liquid water can be sustained between surface texture such that the ice/water interface area exceeds the ice/substrate interface area. Such appropriately textured, icephobic materials may be applied as robust surface coatings in a wide range of anti-icing and de-icing applications.

1.3. Computational Methods

In this work, molecular dynamics is used to provide a quantitative characterization of material icephobicity and to probe the utility of liquid water sustained between surface roughness in reducing ice adhesion.

1.3.1. Force Fields

The course-grained mW [17] water model was used for computational efficiency and for precision capture of the hexagonal, cubic, and amorphous phases of ice. mW, proposed by Moore and Molerino, is a single particle model that accurately reproduces the structure, energetics, and phase transitions of water. The model comprises a re-parameterization of the Stillinger Webber potential, which incorporates a three-body term that penalizes non-tetrahedral configurations [17]:

$$(1.8) \quad E = \sum_i \sum_{j>i} \phi_2(r_{ij}) + \sum_i \sum_{j>i} \phi_3(r_{ij}, r_{ik}, \theta_{ij})$$

$$(1.9) \quad \phi_2(r) = A\epsilon \left[B \left(\frac{\sigma}{r} \right)^p - \left(\frac{\sigma}{r} \right)^q \right] \exp \left(\frac{\sigma}{r - a\sigma} \right)$$

$$(1.10) \quad \phi_3(r, s, \theta) = \lambda\epsilon [\cos\theta - \cos\theta_o]^2 \exp \left(\frac{\gamma\sigma}{r - a\sigma} + \frac{\gamma\sigma}{s - a\sigma} \right)$$

Ice nucleation and liquid diffusion are several times faster in mW than in water due to the absence of hydrogen atoms and long-range electrostatic calculations allows crystallization studies using mW to access longer time and length scales [20].

1.3.2. Molecular Dynamics

Molecular dynamics simulations were implemented using LAMMPS [139] software. A periodic domain of water was initially crystallized at $T < 273.15$ K and $p_C = 1$ atm. A solid substrate material was constructed from mW molecules in the ice phase, similar to previous studies [20]. Molecules defining the substrate were tethered to their equilibrium positions. The interaction between the substrate and water was governed by a 6-12 Lennard Jones pair potential [11]; water-water as well as surface-surface interactions were governed by the three-body mW potential.

1.3.3. CHILL Algorithm

The CHILL algorithm developed by Moore et al. differentiates cubic, hexagonal, and interfacial ice as well as liquid water and low density glass (amorphous ice). The local structures of the four closest neighbors of a mW molecule are projected onto a basis of spherical harmonics. The alignment of the local structure centered on each neighbor characterizes the central mW molecule as belonging to a specific ice or liquid phase [20].

1.3.4. Surface Energy

The surface energies σ between the various phase interfaces were calculated using the stress tensor method [17] in molecular dynamics simulations:

$$(1.11) \quad \sigma = L_z(P_N - \bar{P}_T)$$

where L_z is the length of the simulation domain normal to the interface, $P_N = P_{zz}$ is the normal component of the stress tensor with respect to the interface, and $\bar{P}_T = \frac{1}{2}(P_{xx} + P_{yy})$

is the average of the tangential components of the stress tensor. From equation (1.12), the ratio of surface energies can be used to find the intrinsic, equilibrium contact angle for liquid-vapor, ice-liquid, and ice-vapor (θ_{LV} , θ_{IL} , θ_{IV}) interaction with the substrate:

$$(1.12) \quad \cos(\theta_{IL}) = \frac{\sigma_{LS} - \sigma_{IS}}{\sigma_{IL}}.$$

The surface energy between water and the substrate is changed to modulate surface hydrophobicity/icephobicity by altering the Lennard Jones energy parameter [11]. It would be of interest, but not in the scope of the current study, to examine how surface energy changes with surface polarity.

1.3.5. Data Availability

Data generated or analysed during this study are included in this published article (and its supplementary information files).

1.4. Acknowledgements

The authors thank S. Keten of Northwestern University for suggestions regarding the use of metadynamics as well as the mean squared displacement metric to quantify water mobility. This research was supported by the McCormick Catalyst Award at Northwestern University and by funding from the Illinois Space Grant Consortium. Computational resources and staff were provided by the high performance computing facility, QUEST, at Northwestern University which is jointly supported by the Office of the Provost, the Office for Research, and Northwestern University Information Technology.

1.5. Author contributions statement

N.A.P. , P.R.J. and T.Y.Z. conceived and planned the research. T.Y.Z. and P.R.J. performed simulations. T.Y.Z., P.R.J. and N.A.P. wrote the manuscript.

CHAPTER 2

Leidenfrost point

As a surface is superheated above the boiling point of an adjacent fluid, vapor bubbles nucleate and grow. The boiling behavior of the liquid phase undergoes a fundamental change at a critical temperature known as the Leidenfrost point. Beyond this point, a film of insulating vapor forms between the liquid and the surface that suppresses heat transfer from the solid material. This heat flux reduction can be highly detrimental in the quenching of metal alloys by extending cooling rates and precluding the desired increase in strength and hardness [29]. Alternatively, film boiling may be used to promote drag reduction as well as enable power generation through self-propulsion [30, 31, 32]. Thus, modulation of the LFP through fluid choice, surface texture and chemistry for the specific application is crucial [33].

On a fundamental level, the physical mechanism responsible for the LFP is still uncertain. Many theoretical frameworks have been used to characterize the Leidenfrost effect and estimate the LFP, including hydrodynamic instability [34, 35], superheat spinodal limits [119, 37], and the change of liquid wettability on the heated surface with temperature [38, 39]. A thermocapillary model has also been proposed that attributes the film instability to fluctuations at micron length scales; however the analysis posits that the thermocapillary effect is the dominant destabilizing term, which does not explain the significant change in LFP on surfaces with different wettabilities [40]. For example, the LFP

of water can vary from 300°C for hydrophilic surfaces to 145°C on hydrophobic surfaces [41, 42].

In this work, we introduce a stability analysis of the vapor film at the nanoscale regime. The dominant destabilizing term arises from the van der Waals interaction between the bulk liquid and the substrate across a thin vapor layer. On the other hand, liquid-vapor surface tension driven transport of vapor and evaporation at the two phase interface stabilize the film. The competition between these mechanisms gives rise to a comprehensive description of the LFP as a function of both fluid and solid properties. For fluids that wet the surface, such that the intrinsic contact angle is small, a single dimensionless number (eqn. 2.48) can be derived that encapsulates the instability determining the Leidenfrost point.

It is noted that the literature has proposed different names for the critical temperature associated with a droplet levitating on a heated plate (Leidenfrost point) versus the critical temperature for vapor film formation in pool boiling (minimum film temperature). The Leidenfrost point has been shown to be equivalent to the minimum film boiling temperature for saturated liquids on isothermal surfaces [43]. In this work, the term LFP will be used for both cases as a matter of convenience, with the understanding that no undercooling is applied to the liquid phase for pool boiling scenarios unless explicitly stated.

2.1. Film Instability

There are many approaches to examine the stability of a vapor film adjacent to a superheated wall in two dimensions. Models have been developed with a base solution

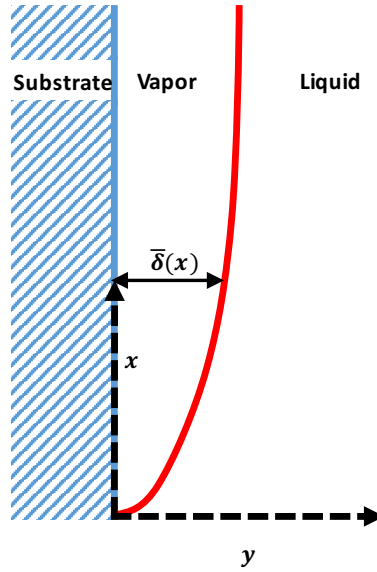


Figure 2.1. Film boiling on a vertical plate, with the coordinate system delineated. The film thickness is denoted by $\bar{\delta}(x)$

imposing static equilibrium, where the interface is at the saturation temperature corresponding to the imposed, far field liquid pressure [40, 44]. Here, we consider the thickness of the vapor film to be in dynamic equilibrium, as in a vertical plate configuration [45] or vapor under a droplet [46]. This appears to be a more general analysis since under experimental settings, droplet levitation occurs over a film that is continuously replenished by evaporation and depleted through escape of the buoyant vapor phase. Similarly in a horizontal setup for pool boiling, bubbles pinch off the film, necessitating a nonzero rate of evaporation to sustain a constant mean film thickness [45].

Fig. 2.1 shows a chosen “model” problem of film boiling on a vertical plate [45, 119]. The vapor forms a laminar layer at the wall, with evaporation at the liquid interface sustaining the buoyant transport of vapor mass away from the base of the plate. The surrounding liquid is saturated and motionless with its properties fixed at the saturation

temperature. The properties of vapor are assumed to be constant at the superheated wall temperature, an assumption discussed in the Supplementary.

2.1.1. Governing Equations

The mass, momentum and energy conservation equations in the vapor domain are given by the following boundary-layer equations:

$$(2.1) \quad \frac{\partial \bar{u}_V}{\partial x} + \frac{\partial \bar{v}_V}{\partial y} = 0$$

$$(2.2) \quad \bar{u}_V \frac{\partial \bar{u}_V}{\partial x} + \bar{v}_V \frac{\partial \bar{u}_V}{\partial y} = -\frac{1}{\rho_V} \frac{\partial \bar{\Phi}}{\partial x} + \frac{\Delta \rho g}{\rho_V} + \frac{\mu_V}{\rho_V} \frac{\partial^2 \bar{u}_V}{\partial y^2}$$

$$(2.3) \quad \frac{\partial \bar{\Theta}}{\partial t} + \bar{u}_V \frac{\partial \bar{\Theta}_V}{\partial x} + \bar{v}_V \frac{\partial \bar{\Theta}_V}{\partial y} = \frac{k_V}{\rho_V c_{p,V}} \frac{\partial^2 \bar{\Theta}_V}{\partial y^2}$$

where the parameters μ , ρ , k , g and c_p represent the the dynamic viscosity, density, thermal conductivity, gravitational acceleration and specific heat of the fluid, respectively. The term $\Delta \rho = \rho_L - \rho_V$ represents the density difference, the subscripts L and V denote the liquid and vapor field, and the temperature has been normalized as $\bar{\Theta} = \frac{\bar{T} - T_s}{T_w - T_s}$, the difference between the temperature field and the saturation temperature T_s at the interface over the difference between the wall temperature T_w and T_s . Note that we take the liquid phase to be motionless due to its much greater viscosity relative to the vapor ($u_L(x, t) = 0$), as well as isothermal at saturation temperature in the long-time limit (equilibrium) due to its larger thermal conductivity ($\Theta_L = 0$) [47]. Due to high thermal conductivity of the liquid relative to the vapor, the temperature variations in the liquid

are much less than those in the vapor. Consequently, most of the temperature gradient would be observed within the vapor. These simplifications allow for an analytical solution for the base state per Burmeister [45].

Note that if no external temperature boundary conditions are imposed on the liquid reservoir, the saturation condition for the liquid is well established in experiment [43]. The adjacent liquid is also generally assumed to be at the saturation temperature in physical models of film boiling [119, 45, 57].

The generalized pressure term $\bar{\Phi}$ takes into account both the fluid pressure arising due to surface tension as well as due to van der Waals interactions. To first order in the base solution, these terms are negligible since the liquid-vapor interface is assumed to be locally parallel to the wall [48, 49]; this implies $\bar{\Phi} \approx 0 + \Phi'$, where the overbar variables represent the general solution, the unbarred variables denote the base solution, and the primed variables give the perturbed solution. Additionally, the momentum and temperature equations are modeled as steady in the base solution and only exhibit a time varying term in the linearized equations for the perturbations.

The boundary conditions at the superheated wall and the liquid-vapor interface at $\bar{\delta}(x)$ are given by:

$$(2.4) \quad \text{at } y = 0, \quad \bar{u}_v = \bar{v}_v = 0, \quad \bar{\Theta}_v = 1$$

$$(2.5) \quad \text{at } y = \bar{\delta}, \quad \bar{u}_v + \bar{v}_v \frac{d\bar{\delta}}{dx} = 0, \quad \bar{\Theta}_v = 0$$

Eqn. 2.4 enforces the temperature and no interfacial slip at the impermeable wall, while eqn. 2.5 ensures that the tangential component of velocity is continuous and that

the temperature is at saturation along the liquid-vapor interface. As with Burmeister, we neglect the “blowing” of vapor toward the plate by assuming $v(x, t) \approx 0$, such that the preceding set of boundary conditions are sufficient to fully specify the problem. Otherwise, the normal component of velocity would also need to be fixed at the interface; this leads to a cubic rather than a parabolic estimate to the velocity field.

The vapor generated due to phase change at this interface is balanced by the stream-wise rate of change of the vapor flow in the film and the growth of the film thickness in time:

$$(2.6) \quad \rho_v \frac{\partial \bar{\delta}}{\partial t} + \frac{\partial}{\partial x} \int_0^{\bar{\delta}} (\rho_v \bar{u}_v dy) = -\frac{k_v}{h_{LV}} \frac{\partial \bar{\Theta}_v}{\partial y} \Big|_{y=\bar{\delta}}$$

where h_{LV} is the latent heat of vaporization. In the base state, the time variation of the film thickness is taken to be negligible, $\frac{d\bar{\delta}}{dt} \approx 0 + \frac{d\delta'}{dt}$. An in-depth description of this setup is covered in the Supplementary.

2.1.2. Base Flow

Along with the boundary conditions (eqn. 2.4 and 2.5), the base flow equations are:

$$(2.7) \quad \frac{\partial u_v}{\partial x} + \frac{\partial v_v}{\partial y} = 0$$

$$(2.8) \quad u_v \frac{\partial u_v}{\partial x} + v_v \frac{\partial u_v}{\partial y} = \frac{\Delta \rho g}{\rho_v} + \frac{\mu_v}{\rho_v} \frac{\partial^2 u_v}{\partial y^2}$$

$$(2.9) \quad u_v \frac{\partial \Theta_v}{\partial x} + v_v \frac{\partial \Theta_v}{\partial y} = \frac{k_v}{\rho_v c_{p,v}} \frac{\partial^2 \Theta_v}{\partial y^2}$$

The steady, developed solution can be found approximately by using an integral expansion method, which is described in full detail by Burmeister [45]. After introducing the normalized variable $\eta = y/\delta$, we can determine the velocity (u_v) and temperature field (Θ_v) in the base solution:

$$(2.10) \quad u_v = \frac{\Delta\rho g \delta^2}{2\mu_v} (\eta - \eta^2)$$

$$(2.11) \quad \Theta_v = \frac{T_v - T_s}{T_w - T_s} = 1 + \left(-1 - \frac{1-c}{2}\right)\eta + \frac{1-c}{2}\eta^3$$

Note that the velocity profile is locally parabolic due to the buoyancy force, while the velocity variation in the streamwise direction under mass conservation is encapsulated in the $\delta(x)^2$ dependence and occurs on a much larger length scale. The value of c can be found by solving the quadratic expression [45]:

$$(2.12) \quad \frac{1}{3} \frac{c_{p,v} \Delta T}{h_{LV}} c \left(1 - \frac{3}{10}(1-c)\right) = 1 - c$$

and $\Delta T = T_w - T_s$. For typical Jakob numbers around $Ja = \frac{c_{p,v} \Delta T}{h_{LV}} = \frac{1}{10}$, c can be found from a simplified linear equation $c = 1 - \frac{1}{3} \frac{c_{p,v} \Delta T}{h_{LV}}$. Using this approximation, the film thickness δ is described by:

$$(2.13) \quad \delta = 2 \left(1 - \frac{1}{3} \frac{c_{p,v} \Delta T}{h_{LV}}\right)^{1/4} \left(\frac{x \Delta T \mu_v k_v}{\rho_v h_{LV} g \Delta \rho}\right)^{1/4}$$

Note that to first order, the velocity and temperature fields as well as the film thickness are steady.

2.1.3. Linearized Equations

The base solutions for the velocity, temperature and film thickness are perturbed, yielding the following linearized equations:

$$(2.14) \quad \frac{\partial u'}{\partial x} + \frac{\partial v'}{\partial y} = 0$$

$$(2.15) \quad u' \frac{\partial u}{\partial x} + u \frac{\partial u'}{\partial x} + v' \frac{\partial u}{\partial y} + v \frac{\partial u'}{\partial y} = -\frac{1}{\rho_V} \frac{\partial \Phi'}{\partial x} + \frac{\mu_V}{\rho_V} \frac{\partial^2 u'}{\partial y^2}$$

$$(2.16) \quad \frac{\partial \Theta'}{\partial t} + u' \frac{\partial \Theta}{\partial x} + u \frac{\partial \Theta'}{\partial x} + v' \frac{\partial \Theta}{\partial y} + v \frac{\partial \Theta'}{\partial y} = \frac{k_V}{\rho_V c_{p,V}} \frac{\partial^2 \Theta'}{\partial y^2}$$

The boundary conditions at the wall are:

$$(2.17) \quad \text{at } y = 0 \quad u'_V = v'_V = 0, \quad \Theta'_V = 0$$

At the perturbed interface location $\delta + \delta'$, the tangential velocity and temperature conditions (eqn. 2.5) after applying the locally parallel approximation $\frac{d\delta}{dx} \approx 0$ give:

$$(2.18) \quad u'_V|_{\eta=1} + \frac{\delta'}{\delta} \frac{\partial u}{\partial \eta}|_{\eta=1} = 0, \quad \Theta'_V|_{\eta=1} + \frac{\delta'}{\delta} \frac{\partial \Theta_V}{\partial \eta}|_{\eta=1} = 0$$

The phase change equation at the interface (eqn. 2.6) is linearized as:

$$(2.19) \quad \rho_V \frac{\partial \delta'}{\partial t} + \frac{\partial}{\partial x} \int_0^\delta \rho_V u'_V dy + \frac{\partial}{\partial x} \int_0^{\delta+\delta'} \rho_V u_V dy = -\frac{k\Delta T}{h_{LV}} \left(\delta' \frac{\partial^2 \Theta}{\partial y^2} \Big|_\delta + \frac{\partial \Theta'}{\partial y} \Big|_\delta \right)$$

Analogous to the base solution, the perturbed velocity is expanded in powers of η .

$$(2.20) \quad u'_v = a'_0 + a'_1\eta + a'_2\eta^2$$

$$(2.21) \quad \text{at } \eta = 0 \quad u'_v = 0 \rightarrow a'_0 = 0$$

The terms a'_1 and a'_2 can be found as functions of the fluid properties and the generalized pressure gradient $\frac{\partial\Phi'}{\partial x} = \frac{\partial p'}{\partial x} + \frac{\partial\phi'}{\partial x}$ from the momentum equation eqn. 2.15 evaluated at the wall ($\eta = 0$) and the tangential velocity condition (eqn. 2.18).

$$(2.22) \quad a'_1 = \left(\frac{\Delta\rho g\delta\delta'}{2\mu_v} - \frac{\frac{\partial\Phi'}{\partial x}\delta^2}{2\mu_v} \right)$$

$$(2.23) \quad a'_2 = \frac{\frac{\partial\Phi'}{\partial x}\delta^2}{2\mu_v}$$

The pressure gradient arises from the liquid-vapor surface tension σ_{LV} at the two phase interface due to capillary pressure induced by local nonzero curvature:

$$(2.24) \quad \frac{\partial p'}{\partial x} = -\sigma_{LV} \frac{d^3\delta'}{dx^3}$$

This implies that positive curvature corresponds to the center of curvature lying in the vapor domain, such that the vapor bulges into the liquid. Here, we also introduce the disjoining pressure term $\bar{\phi}$, which describes the van der Waals interaction between the fluid and the substrate:

$$(2.25) \quad \bar{\phi} = \frac{A}{6\pi\bar{\delta}^3}$$

The streamwise derivative of this term is negligible in the base state under the locally parallel interface approximation. The Hamaker constant A is typically positive, denoting attractive interactions between dipoles [50]. The perturbed component is:

$$(2.26) \quad \frac{\partial \phi'}{\partial x} = -\frac{A}{2\pi\delta^4} \frac{d\delta'}{dx}$$

This gives an expression for the perturbed, generalized pressure term evaluated at the liquid-vapor interface.

$$(2.27) \quad \frac{\partial \Phi'}{\partial x} = \frac{\partial p'}{\partial x} + \frac{\partial \phi'}{\partial x} = -\sigma_{LV} \frac{d^3 \delta'}{dx^3} - \frac{A}{2\pi\delta^4} \frac{d\delta'}{dx}$$

Next, the expanded perturbed temperature is:

$$(2.28) \quad \Theta'_v = b'_0 + b'_1 \eta + b'_2 \eta^2 + b'_3 \eta^3$$

From the wall boundary condition (eqn. 2.17) and energy conservation equation (eqn. 2.16) at $\eta = 0$, we find that $b'_0 = b'_2 = 0$. Similarly, the temperature condition (eqn. 2.18) and energy conservation (eqn. 2.16) at the interface $\eta = 1$ leads to an expression for b'_1 in terms of δ' :

$$(2.29) \quad \frac{\delta}{4} \frac{\partial b'_1}{\partial t} + \frac{1}{4} (1 - 2b_3) \frac{\partial \delta'}{\partial t} + \left(\frac{1}{6} - \frac{2b_3}{15} \right) \frac{\Delta \rho g \delta^2}{2\mu_v} \frac{d\delta'}{dx} \\ + \left(\frac{1}{12} - \frac{b_3}{20} \right) \left(\frac{\delta^3}{2\mu_v} \right) \left(\sigma_{LV} \frac{d^4 \delta'}{dx^4} + \frac{A}{2\pi\delta^4} \frac{d^2 \delta'}{dx^2} \right) \\ + \frac{a_1}{30} (1 - 2b_3) \frac{d\delta'}{dx} + \frac{a_1 \delta}{20} \frac{db'_1}{dx} = \frac{3k_v}{\rho_v c_{p,v} \delta^2} \delta' - \frac{3k_v}{\rho_v c_{p,v} \delta} b'_1$$

The time evolution for the perturbed δ' as a function of b'_1 follows from the linearized phase change expression (eqn. 2.19) and the expressions for u'_v and Θ'_v (eqn. 2.20 and 2.28):

$$(2.30) \quad \rho_v \frac{\partial \delta'}{\partial t} + \frac{\rho_v \Delta \rho g \delta^2}{4\mu_v} \frac{d\delta'}{dx} + \frac{\rho_v \delta^3 \sigma_{LV}}{12\mu_v} \frac{d^4 \delta'}{dx^4} + \frac{\rho_v A}{24\pi \mu_v \delta} \frac{d^2 \delta'}{dx^2} + \frac{3k_v \Delta T}{h_{LV} \delta^2} \delta' - \frac{2k_v \Delta T}{h_{LV} \delta} b'_1 = 0$$

The perturbation equations 2.29 and 2.30 give two homogeneous conditions for δ' and b'_1 . The perturbations can now be expressed in terms of normal modes:

$$(2.31) \quad \delta' = \delta'_a \exp(i(kx + \omega t))$$

$$(2.32) \quad b'_1 = b'_{1a} \exp(i(kx + \omega t))$$

To avoid introducing new notation, we will represent the amplitudes without subscripts $\delta'_a \rightarrow \delta'$ and $b'_{1a} \rightarrow b'_1$. Here, k is the wave number and ω the time rate of growth of the perturbation. We combine eqn. 2.29 and 2.30 to obtain a single equation with the coefficient δ' . To simplify the representation, we introduce the following dimensionless parameters:

$$(2.33) \quad \pi_{LP} = \frac{3A^2 h_{LV} \rho_v}{(24\pi)^2 \delta^3 k_v \mu_v \Delta T \sigma_{LV}}$$

$$(2.34) \quad \pi_{LB\sigma_{LV}} = \sqrt{\frac{A}{\pi \sigma_{LV}}} \left(\frac{\Delta \rho g \delta^2 h_{LV} \rho_v}{2k_v \mu_v \Delta T} \right)$$

$$(2.35) \quad k'' = k\delta^2 \sqrt{\frac{4\pi\sigma_{LV}}{A}}$$

$$(2.36) \quad \omega' = \omega \left(\frac{h_{LV}\rho_V\delta^2}{k_V\Delta T} \right)$$

This leads to the general, characteristic equation for the temporal growth rate $i\omega$ of the perturbation after eliminating b'_1 using eqn. 2.29 and 2.30:

$$(2.37) \quad \left(\frac{i\omega'}{8} + \frac{ik''\pi_{LB\sigma_{LV}}}{80} + \frac{3}{2Ja} \right) \\ \left(i\omega' + ik''\frac{\pi_{LB\sigma_{LV}}}{4} + k''^4\pi_{LP} - 2\pi_{LP}k''^2 + 3 \right) \\ + i\omega'\frac{c}{4} + ik''\frac{(1+c)\pi_{LB\sigma_{LV}}}{20} + k''^4\frac{3\pi_{LP}}{20}\left(\frac{7}{3} + c\right) \\ - k''^2\left(\frac{7}{3} + c\right)\frac{3\pi_{LP}}{10} - \frac{3}{Ja} = 0$$

The marginal state occurs when the real part $\text{Re}(i\omega) = 0$, separating zones of stability ($\text{Re}(i\omega) < 0$), where the perturbation amplitude decays in time, from regions of instability ($\text{Re}(i\omega) > 0$), where the base state becomes unstable (Fig. 2.2 **a**). Note that only three dimensionless numbers Ja , π_{LP} and $\pi_{LB\sigma_{LV}}$ govern the stability of the perturbed solution. With the inclusion of van der Waals interactions, the buoyancy terms described by $\pi_{LB\sigma_{LV}}$ become negligible at nanoscale, as will be discussed shortly.

This analysis incorporated time variation and convective transport in the energy equation. We can obtain a simpler expression for the stability problem by neglecting these two terms:

$$(2.38) \quad i\omega' = - \left(k''^4 \pi_{LP} - 2k''^2 \pi_{LP} + 1 \right) - ik'' \frac{\pi_{LB\sigma_{LV}}}{4}$$

where the buoyancy term $\pi_{LB\sigma_{LV}}$ is explicitly shown to give the dimensionless traveling wave velocity, signifying that the base flow acts only to convect the perturbation and does not affect its growth. The full derivation of eqn. 2.38 is provided in the Supporting Information.

The diffusive expression (eqn. 2.38) is a good estimate to the full stability equation (eqn. 2.37) for small Jakob numbers, as demonstrated in Fig. 2.2 c. Since the dimensionless parameters are calculated from the vapor properties at the superheated wall temperature, the Jakob number is small ($Ja \lesssim \frac{1}{10}$) for the vapor phase of most fluids, implying that the thermal energy imparted by the heated solid is predominantly consumed through the latent heat of phase change rather than as sensible heat in raising the temperature of the vapor. Physically, dropping the time varying term in the energy equation implies that the heat conduction time scale is much longer (quasi-steady) than that for the perturbation growth in the phase change equation.

The Leidenfrost point corresponds to the lowest, critical $\pi_{LP, \text{crit}}$ on the marginal stability curve, below which the flow becomes unconditionally stable for all values of k'' . For eqn. 2.37, a good approximation for the critical π_{LP} can be derived by noting that due to how we scaled the dimensionless parameters, $\pi_{LP, \text{crit}}$ occurs at $k'' = 1$. This leads to

an algebraic equation for $\pi_{LP, \text{crit}}$:

$$(2.39) \quad \left(\frac{Ja}{10}\left(\frac{7}{3} + c\right) + 1\right)\pi_{LP, \text{crit}} - 1 \left(1 + \frac{Ja}{4} + \frac{Ja}{6}c - \frac{Ja}{12}\pi_{LP, \text{crit}}\right)^2 \\ = \left(\frac{3\pi_{LB}\sigma_{LV}}{20}\right)^2 \left(\frac{Ja}{12}\right)^2 \left(1 + \frac{Ja}{9}(2 + c)\right) \left(\frac{1}{3} + \frac{2c}{3} - \pi_{LP, \text{crit}}\right)$$

Eqn. 2.39 was verified against a numerical solution to the full stability equation (eqn. 2.37) with $\text{Re}(i\omega) = 0$, and was found to give the same solution for $\pi_{LP, \text{crit}}$ up to machine precision for all parameter sets tested (Fig. 2.2 **b**). For small Jakob numbers, Fig. 2.2 **c** shows that the critical π_{LP} can also be estimated from the diffusive expression (eqn. 2.38).

$$(2.40) \quad \pi_{LP, \text{crit}} = 1$$

The implication of eqn. 2.40 as a good estimate is threefold. First, it means that the boundary layer approximation is not required if film boiling is assumed to be diffusion dominated in both energy and momentum via lubrication theory. Secondly, the use of the locally-parallel assumption [48, 49] is self-consistent since the film thickness δ in the base solution changes over a much longer length scale compared to the critical perturbation wavelength. Note that the wave number k for the critical stability criterion $k'' = 1$ is on the order of 100 (1/micron), corresponding to a wavelength of around 10 nm. Over this wavelength, the relative change in film thickness $\frac{\Delta\delta}{\delta}$ is around $10^{-9} \ll 1$, showing that the slow growth of the film thickness is negligible in the perturbation analysis.

Lastly, perturbation growth is independent of the base flow, which carries vapor generated at the liquid-vapor interface out of the local control volume. This explains why

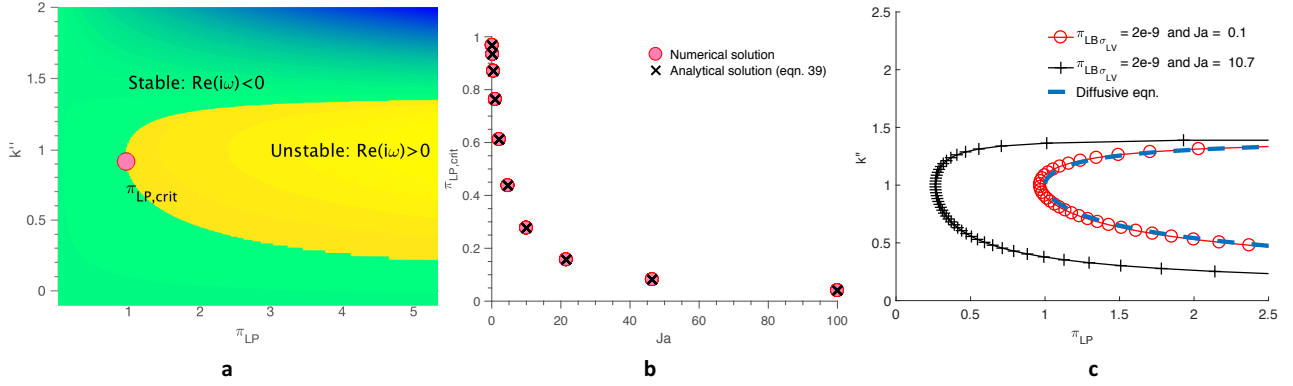


Figure 2.2. **The stability of the perturbed solution.** **a.** The variation of $\text{Re}(i\omega)$ with π_{LP} and the dimensionless wavenumber k'' for $\Pi_{LB\sigma_{LV}} = 2 \times 10^{-9}$ and $Ja = 0.1$. A critical $\pi_{LP,crit}$ can be defined, for which lower values lead to unconditional stability, and greater values allow the coexistence of stable and unstable zones. **b.** The Jakob number vs the critical $\pi_{LP,crit}$, as predicted by the numerical solution to the full stability solution (eqn. 2.37) and by taking $\pi_{LP,crit}$ to occur at $k'' = 1$ (eqn: 2.39). The agreement is excellent. **c** The marginal stability curves are calculated by taking the locus of points where the real value of $i\omega$ changes sign. The diffusive expression (eqn. 2.38) is a good approximation for small Jakob numbers.

the LFP is not found to be strongly dependent on the configuration of the experimental set up. Any configuration eventually takes the vapor out of the film by some buoyancy driven force (even if it is horizontal or upside down - vapor eventually finds its way up). The strength of that driving force would indeed depend on configuration, but it does not matter for the perturbation solution.

2.1.4. Stabilizing Terms

The diffusive approximation to the critical π_{LP} (eqn. 2.40) reveals that the main stabilizing terms are the liquid-vapor surface tension σ_{LV} , the evaporative phase change that replenishes local vapor mass $\frac{k_V \Delta T}{h_{LV} \rho_V}$, and the viscous shear μ that reduces mass transport away from any given point in the vapor field.

The liquid-vapor surface tension acts as a restoring force against oscillatory modes imposed on the basic, locally-parallel solution. Positive curvature of the liquid-vapor interface with its center in the vapor region (curving into the liquid), induces high pressure locally with an adjacent low pressure zone due to the negative curvature of the continuous two phase interface. This creates a pressure gradient that attempts to restore the basic state by dampening all possible oscillatory frequencies.

Similarly, a perturbed interface that bulges into the vapor steepens the thermal gradient in the vapor film, triggering an increase in the rate of evaporation locally that restores the base state and vice versa. Viscous shear is larger for smaller film thicknesses, therefore reducing mass transport away from a local bulge into the vapor domain and enhancing transport away from a bulge into the liquid field; this also acts to dampen perturbed modes.

2.1.5. van der Waals Interaction

The heterogeneous Hamaker constant A_{SVL} is used to characterize the van der Waals dispersion forces between an uncharged surface and an adjacent liquid separated by vacuum. It is incorporated into this analysis via the generalized pressure gradient (eqn: 2.27). From the diffusive expression of the perturbation stability (eqn. 2.38), it is shown that these dispersion forces between the liquid and solid substrate across the vapor film is the only destabilizing term for attractive interactions $A > 0$. The film is unconditionally stable if the interaction is purely repulsive $A < 0$. The former case holds in general for a liquid separated from a solid by a vacuum or an intermediate gas phase [51, 52].

The relationship between the heterogeneous Hamaker constant and the contact angle θ of the substrate has been derived using Lifshitz theory [53, 54] :

$$(2.41) \quad 1 + \cos(\theta) = \frac{A_{SVL}}{12\pi\sigma_{LV}H_{SVL}^2}$$

where H_{SVL} is the equilibrium contact separation between the solid substrate (S) and the liquid (L) across vacuum (V) and takes on values in the order of magnitude of 1 nm for most materials. Eqn. 2.41 can thus be used to account for the effect of surface wettability on the stability of the perturbed solution. As the van der Waals interaction only plays a significant role for film thicknesses that have reached the same order of magnitude as H_{SVL} , we approximate the ratio $\frac{H_{SVL}}{\delta} \approx 1$.

In this nanoscale regime, the neutral curve described by the full perturbation solution (eqn: 2.37) is insensitive to $\pi_{LB\sigma_{LV}}$, which encapsulates the buoyancy force on the vapor film and is on the order of 10^{-14} . The diffusive expression of the perturbation equation (eqn. 2.38) has an explicit dependence on $\pi_{LB\sigma_{LV}}$ only in the imaginary part of the temporal growth rate, such that the marginal state predicted is completely agnostic to changes in $\pi_{LB\sigma_{LV}}$. This implies that the stability criterion (eqn. 2.39 or 2.40) can be applied to capture the Leidenfrost point on plates of arbitrary orientation, as the direction and magnitude of the gravitational field does not play a significant role in the instability mechanism examined. The further implications of the nanoscale regime on this analysis is presented in the Supporting Information.

2.2. Verification by experiment and simulation

To compare against experimental data, eqn. 2.40 for the critical π_{LP} can be rewritten in terms of material properties:

$$(2.42) \quad \frac{3}{(24\pi)^2} \left(\frac{1}{\delta}\right)^4 \frac{h_{LV}\rho_V\delta}{\sigma_{LV}} A^2 \frac{1}{k_V\Delta T\mu_V} = 1$$

Substituting in eqn. 2.41, we obtain the corresponding expression for the LFP in terms of the intrinsic contact angle on the substrate.

$$(2.43) \quad \underbrace{\frac{3}{4} \left(\frac{H_{SVL}}{\delta}\right)^4}_{\approx 1} \underbrace{\left(\frac{h_{LV}\rho_V\delta}{\sigma_{LV}}\right)}_{\pi_2} (1 + \cos(\theta))^2 \underbrace{\frac{\sigma_{LV}^2}{k_V\Delta T\mu_V}}_{\pi_1} = 1$$

where we have defined two new dimensionless parameters that we will show to be significant:

$$(2.44) \quad \pi_1 = \frac{\sigma_{LV}^2}{k_V\mu_V\Delta T}$$

$$(2.45) \quad \pi_2 = \frac{h_{LV}\rho_V\delta}{\sigma_{LV}}$$

Eqn. 2.43 provides an explicit relationship between the intrinsic contact angle of a fluid on a substrate and the Leidenfrost point for the system. Since each fluid property ($k_V(T)$, $\mu_V(T)$, $\sigma_{LV}(T)$, etc.) is calculated at the superheated wall temperature, the left hand side of eqn. 2.43 is in general a nonlinear function of temperature. The temperature at which eqn. 2.43 is satisfied corresponds to the predicted LFP; this can be found numerically with the temperature and pressure dependent fluid properties available from databases like NIST and tabulations from literature [124, 56, 57].

For ease of use, eqn. 2.43 can also be written using corresponding states correlations (eqn. 2.67), which express fluid properties in terms of the critical temperature T_c and pressure p_c , the applied saturation pressure p , and the molar mass of the fluid.

2.2.1. Surface dependence of the LFP

The LFP for water has been demonstrated to vary dramatically with changes in the liquid wettability of the solid surface [41, 42]. Fig. 2.3 shows that the diffusive prediction of the LFP (eqn. 2.43) accurately captures the relationship between the LFP and the contact angle as delineated by experiments [58, 42, 59, 41, 60]. Physically, larger contact angles indicate a hydrophobic substrate, which exhibits less attractive van der Waals interaction with the bulk liquid and presents a smaller destabilizing effect to the vapor film; the LFP thus decreases to near the boiling point. Without considering van der Waals interaction between the liquid and substrate surfaces, such a relationship cannot be explained or predicted from first principles.

Further evidence of the significant role played by van der Waals forces in governing the LFP arises from X-ray imaging of the vapor film collapse [62]. Images spanning the film lifespan between formation and collapse showed that film collapse on the macroscopic level is preceded by submicron length scale vapor film thicknesses where the bulk liquid appears to wet the substrate. Although instabilities on the micron scale and above perturb the liquid-vapor interface and induce frequent local contact between the liquid and solid, only when the vapor film becomes unstable on the smallest length scales where van der Waals interactions dominate will the film completely collapse. Further discussion on the time

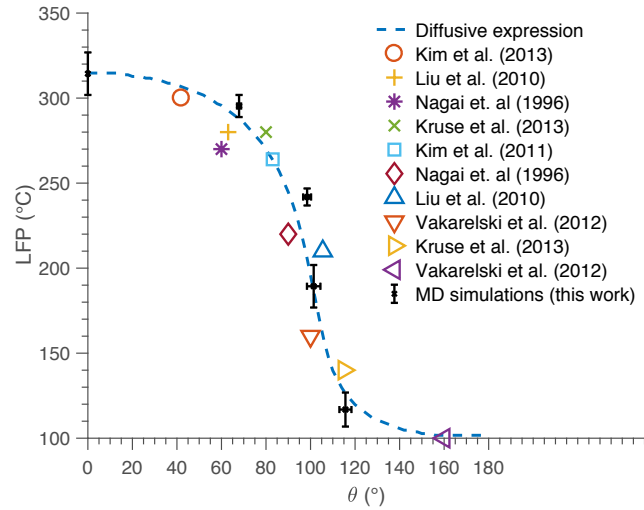


Figure 2.3. The Leidenfrost temperature vs the contact angle for water, from experiments [58, 42, 59, 41, 60], the diffusive prediction of the LFP (eqn. 2.43) and molecular dynamics simulations from this work. The equilibrium separation H_{SVL} and its variation associated with changes in the contact angle $\frac{dH_{SVL}}{d\theta}$ can be estimated from experimental data [61, 53]. Typical errors in the LFP and the contact angle measured from experiment are around 5°C and 2° respectively, though many sources do not explicitly report an error value for either quantity. The data point corresponding to a contact angle of 160° from Vakarelski et al. corresponds to the only surface which was textured with nanoparticles to achieve superhydrophobicity; the other data points correspond to flat surfaces with random roughness.

scales associated with the instability theory as well as the residence time and frequency of liquid-solid contact observed in experiment is presented in the Supporting Information.

Lastly, we note that our theoretical analysis predicts that the main effects governing the LFP operate in the nanoscale regime, which is accessible by molecular dynamics (MD). Figure 2.4 shows one of the boiling heat transfer simulations performed using LAMMPS [139] software to numerically determine the LFP and the corresponding intrinsic contact angle of the substrate. Details of the MD implementations are provided in the Supporting Information. Note that a vapor film forms when the liquid water adjacent to the bottom

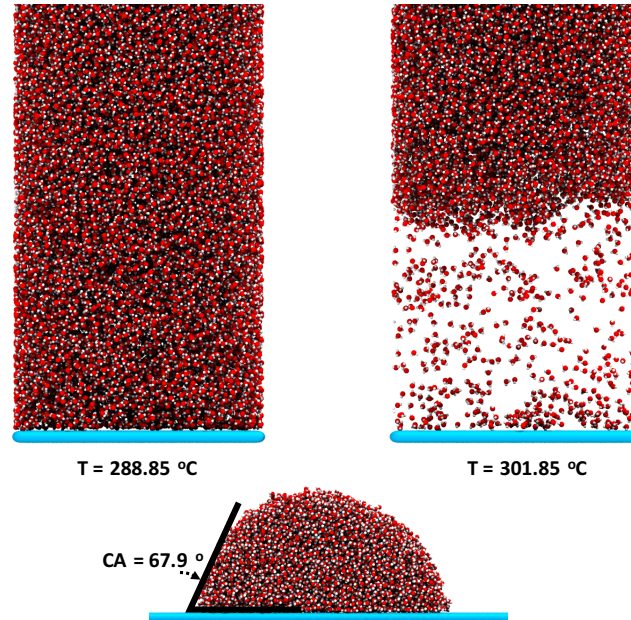


Figure 2.4. Molecular dynamics simulation of vapor film formation adjacent to a heated surface. The system is pressurized at 1 atm.

plate is heated above the LFP, whereas liquid contact with the solid surface is preserved below the LFP due to the attractive heterogeneous van der Waals interactions. The relationship between the contact angle and the Leidenfrost point of the SPC/E (extended simple point charge) water model is in good agreement with the diffusive prediction of the LFP (eqn. 2.43). These simulations show that vapor film stability is ultimately determined at the proposed nanometric length scale where fluid-surface van der Waals interactions cannot be discounted and where the effect of gravity driven instabilities is nonexistent.

2.2.2. Fluid dependence of the LFP

For most experimentally available data on the Leidenfrost point, the contact angle of the fluid on the substrate material is low, around $\theta \approx 20^\circ$. Nonetheless, the Hamaker

constant must be found to determine the equilibrium separation H_{SVL} . Although the assumption $\frac{H_{SVL}}{\delta} \approx 1$ is made, the base film thickness δ still needs to be incorporated into our instability expression via π_2 (eqn: 2.45). We can find the homogeneous Hamaker constant of the fluid (acetone, ethanol, benzene, etc.) and the substrate (gold, aluminum, copper), and take the geometric mean to obtain the heterogeneous value [52, 64]. From the relationship between the surface energy and homogeneous Hamaker constant, we can obtain the homogeneous contact separations via:

$$(2.46) \quad \sigma_{LV} = \frac{A_{LVL}}{24\pi H_{LVL}^2}$$

$$(2.47) \quad \sigma_{SV} = \frac{A_{SVS}}{24\pi H_{SVS}^2}$$

Figure 2.7 shows that it is possible to determine either the heterogeneous Hamaker constant given the Leidenfrost point for a fluid on a solid substrate, or vice versa with knowledge of the homogeneous Hamaker constants of both species.

In general, experimental data on the homogeneous Hamaker constants may not be available for a fluid or substrate of interest. Here, we note an avenue for simplification: it is observed that the dimensionless quantity $\pi_2 = \frac{h_{LV}\rho_V\delta}{\sigma_{LV}}$ in the diffusive expression is around 0.06 for most fluids at their respective Leidenfrost temperatures. This suggests that there exists a functional dependence $H_{SVL} = F\left(\frac{h_{LV}\rho_V}{\sigma_{LV}}\right)$. Additionally, most experimental setups in the film boiling regime feature fluids that wet the surface in contact, such that their intrinsic contact angle are small ($\theta \approx 20^\circ$) [57]. From the diffusive expression (eqn. 2.43) valid for low Jakob numbers, the above approximations leads to a simplified, dimensionless

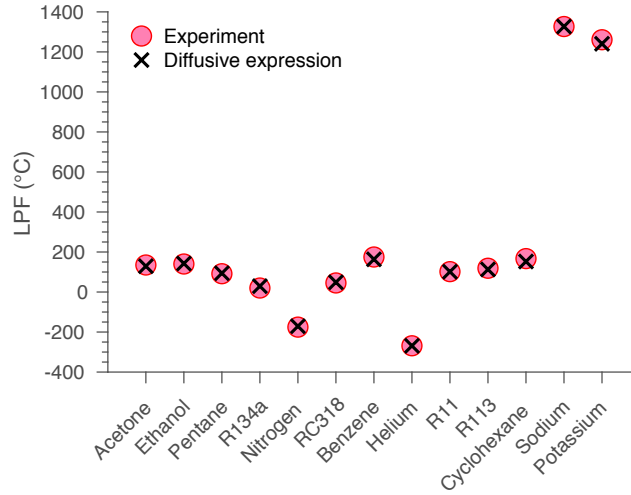


Figure 2.5. The dimensionless criterion $\pi_1 = 6$ as a low contact angle approximation from the diffusive expression (eqn. 2.43) captures the LFP data from experiment to within 5% error. The dimensionless number π_1 encapsulates the stabilizing effects of evaporative phase change (vapor mass generation), surface tension and viscous transport, while the critical value at which the LFP occurs describes the destabilizing role of the van der Waals interaction for low contact angle fluids. Experimental LFP and fluid property data are available for acetone, ethanol, pentane, R134a, nitrogen, RC318, benzene, helium, R11, R113, liquid sodium and liquid potassium [65, 66, 67, 68, 69, 70, 43, 124, 56, 57, 71]

prediction to the Leidenfrost point for fluids/substrate systems with low, intrinsic contact angles:

$$(2.48) \quad \pi_1 = \frac{\sigma_{LV}^2}{k_v \Delta T \mu_v} \approx 6$$

This dimensionless quantity also arises by application of the Buckingham's Pi Theorem to the system, as discussed in the Supporting Information. Fig. 2.5 shows that the temperature at which this equality is satisfied captures the experimental data on the LFP for a variety of different fluids, including cryogenics and liquid metals. The single dimensionless number describes the terms that stabilize the vapor film, including surface

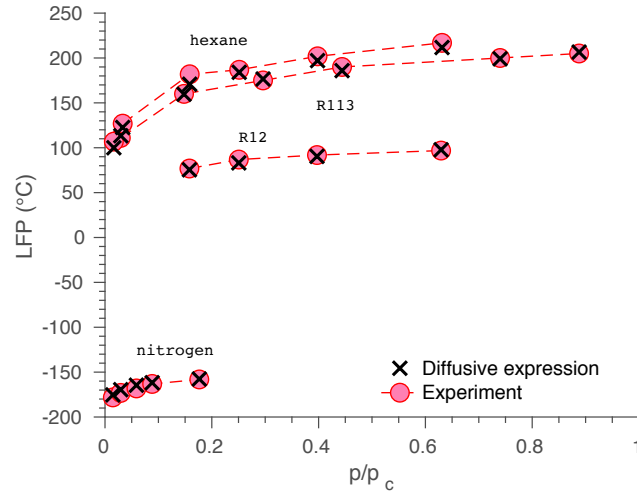


Figure 2.6. The LFP from experimental data of R113, R12, hexane and nitrogen at different pressures (o's) normalized by the critical pressure p_c of the fluid [72, 73, 74] vs the predictive ability of the small contact angle approximation (eqn. 2.49) to the diffusive expression (eqn. 2.43).

tension, phase change and viscous transport, while the critical value corresponding to the LFP denotes the destabilizing effect of attractive van der Waals interaction between the bulk liquid and solid substrate. Larger values of π_1 above the critical imply the system is the film boiling regime, since the stabilizing terms dominate.

2.2.3. Pressure dependence of the LFP

Experimental work has shown that the LFP depends on the ambient pressure applied, such that the Leidenfrost temperature gradually increases from near the boiling point towards the critical point of the fluid [73]. For low contact angle fluid/substrate systems, we find that $\pi_2(1 + \cos(\theta))^2$ scales linearly with pressure such that the LFP corresponds to:

$$(2.49) \quad \pi_1 = 6 \frac{p_{\text{ref}}}{p_{\text{applied}}}$$

where p_{ref} and p_{applied} are 1 atm and the applied, operating pressure, respectively. Essentially, eqn. 2.49 is a small contact angle estimate to the full diffusive expression (eqn. 2.43) obtained by empirical observation of the data and reported for ease of use, since less terms are computed in this approximation. Excel sheets that apply the full diffusive expression and the small contact angle approximations (eqn. 2.48 and 2.49) are provided as supplementary material. Figure 2.6 demonstrates that eqn. 2.49, a simplified estimate to the diffusive expression (eqn. 2.43), captures the LFP of various fluids for both subatmospheric and superatmospheric pressures up to the critical point.

2.3. Conclusion

The dynamic stability of a vapor film on a heated vertical wall under the effects of gravity were considered. The only possible instability at nanoscale was driven by attractive van der Waals interaction between the bulk liquid and the substrate, which could be stabilized by the liquid-vapor surface tension, evaporative phase change and viscous transport. The marginal or neutral state can be found analytically (eqn. 2.39) for the most general case, or simplified for small Jakob number flows to a diffusive approximation (eqn. 2.40). The resulting theoretical solution for the LFP captures the variation of experimental data with surface wettability, fluid properties and pressure.

A single, dimensionless number π_1 is found to encapsulate the physical instability mechanism of the Leidenfrost phenomenon for wetting fluids. The value of π_1 with respect to the critical denotes regimes in which the vapor film is stable or unstable, providing a useful characterization of both the thermodynamic state and the physical means by which transition to the pool boiling regime occurs.

This insight into the nanoscale mechanisms inducing the transition from film to nucleate boiling enables control of the phase adjacent to the surface [75]. It would be of interest to extend the instability mechanism towards surface roughness, which experiment has shown to effect dramatic changes in the LFP beyond what can be explained by variation in surface wettability [33, 42, 76]. In addition, a theoretical treatment of the Nukiyama temperature corresponding to the critical heat flux may reveal the mechanism underlying transition boiling and provide a comprehensive understanding of the entire boiling curve under a unified, physical framework.

2.4. Additional information regarding film boiling on a vertical plate

In the base state, vaporization occurs. This vapor is being moved up within the boundary layer due to buoyancy force (not by external pressure gradient). As one goes to higher elevation within the boundary layer, there has to be more vapor flowing upward because it is a collection of all vapor formed at locations below it. As a result, in the steady base state the boundary layer thickness has to increase with vertical location (x – direction).

In the base solution, the change in boundary layer thickness δ vs. x is resolved. In the base state when δ varies with x , it implies that the liquid-vapor interface is slightly curved. In the presence of surface tension and van der Waals interactions this could give rise to a pressure gradient within the boundary layer in the base state itself. This pressure gradient has been neglected while deriving the base state solution. The reason being that this pressure gradient is smaller compared to the driving buoyancy force when

	σ_{LV}	μ_V	$k_V(T_w - T_s)$	h_{LV}	ρ_L	g	P_V
M	1	1	1	0	1	0	1
L	0	-1	1	2	-3	1	-1
τ	-2	-1	-3	-2	0	-2	-2

delta changes with x on a large length scale. This approximation is similar to prior work in literature [79, 105].

2.5. Supporting Information (SI)

2.5.1. Buckingham's Pi Theorem

In general, the thermodynamic variables that affect the physical onset of film boiling include the thermal conductivity of the vapor (k_V), temperature (T), viscosity of the vapor (μ_V), liquid-vapor surface tension (σ_{LV}), the specific latent heat of vaporization (h_{LV}), the liquid density ρ_L , the vapor pressure P_V , and the gravitational constant g [77, 78, 79]. This leads to four dimensions, namely mass M , length L , time τ and temperature ϕ . Taking the product $k_V(\Delta T) = k_V(T_w - T_s)$ as a single variable, the number of dimensions can be reduced to three, forming the dimensional matrix [80]:

The repeating variables are chosen to be σ_{LV} , $k_V(T_w - T_s)$ and ρ_L , which span the space of M , L , and τ . Given seven variables and a rank three matrix, four dimensionless numbers are expected: $\Pi_1 = \frac{\sigma^2}{k_V(T_w - T_s)\mu_V}$, $\Pi_2 = \frac{\sigma_{LV}^2 h_{LV}}{k_V^2(T_w - T_s)^2}$, $\Pi_3 = \frac{\sigma_{LV}^5 g}{k_V^4(T_w - T_s)^4 \rho_L}$, $\Pi_4 = \frac{\sigma^2 P_V}{k_V^2(T_w - T_s)^2 \rho_L}$. We note immediately that for the dimensionless numbers Π_1 and Π_2 , the repeating variable ρ_L is absent. This suggests that density or mass is not relevant to the subset of variables $k_V(T_w - T_s)$, σ_{LV} , h_{LV} and μ_V ; the dimensionless combination of these variables may be responsible for the static equilibrium behavior of a fluid in the different boiling regimes.

	σ_{LV}	μ_V	$k_V(T_w - T_s)$	h_{LV}
M	1	1	1	0
L	0	-1	1	2
τ	-2	-1	-3	-2

Thus, to reduce the number of independent variables describing the LFP, the gravity, pressure and density of either phase are postponed for consideration in the present analysis. Prior work has shown that accounting for gravity and the density ratio between liquid and vapor accurately captures the length scales of the droplet and vapor film as well as their evolution in time specific to the Leidenfrost regime [81]. The present work focuses instead on the characteristics of a fluid that determines its LFP and distinguishes film boiling from nucleate or transition boiling.

By reducing the variable space, we obtain the dimensional matrix:

The rank of the matrix is two as the rows are linearly dependent; since density, pressure and gravity are neglected, mass is not relevant to the problem. With four variables and a rank two matrix, two dimensionless numbers are expected from the analysis. The repeating variables are chosen to be σ_{LV} and $k_V(T_w - T_s)$, which yield the dimensionless numbers:

$$(2.50) \quad \Pi_1 = \frac{\sigma^2}{k_V(T_w - T_s)\mu_V} = \pi_1$$

$$(2.51) \quad \Pi_2 = \frac{\sigma^2 \Delta H}{k_V^2 (T_w - T_s)^2}$$

The dimensionless number π_1 represents the ratio of the liquid-vapor surface tension to the viscosity, thermal conductivity and temperature of the vapor phase. The LFP is posited to increase for fluids with larger liquid-vapor surface tension based on the model

for the maximum superheat limit [79] and the Taylor type instability [77]. The same correlation between surface tension and the LFP has been demonstrated experimentally across a broad range of fluids [78]. From the superheat limit viewpoint, the relationship arises since a lower liquid-vapor surface tension decreases the energy barrier and increases the rate of vapor nucleation, which reduces the critical temperature necessary to form a vapor film.

From the Taylor instability perspective, the role of surface tension appears contradictory. Larger surface tension is theorized to stabilize the liquid-vapor interface by suppressing low wavelength perturbations and reducing the growth of high wavelength disturbances [77]. It is therefore expected that higher surface tension would lead to a lower LFP by promoting the formation of a stable vapor film. However, the predicted expression for the Leidenfrost temperature originating from Taylor instability theory proposes that the LFP should increase with the surface tension, based on a fitted expression for bubble radii [77]. While accurate for n-pentanes and carbon tetrachloride, it has been shown experimentally that the LFP predicted from the instability analysis is less accurate for water, cryogenic fluids and liquid metals [78].

The experimentally corroborated relationship between liquid-vapor surface tension and the LFP of a fluid means that the Leidenfrost regime should occur for small values of the dimensionless number π_1 , corresponding to low surface tension, high vapor viscosity, high vapor thermal conductivity and high temperature; nucleate or transition boiling occurs for large values of π_1 . For consistency, this suggests that higher vapor thermal conductivity should trigger the Leidenfrost phenomenon by conveying more heat to the liquid-vapor interface and boosting the rate of vaporization. A higher vapor viscosity should also

induce film boiling by stabilizing the vapor layer from perturbations and penalizing the escape of the vapor phase from the film.

Physically, π_1 compares two velocities $\frac{k_V(T_w - T_s)}{\sigma}$ and $\frac{\sigma}{\mu_V}$; the units of these quantities are $\frac{L}{\tau}$. The former $\frac{k_V(T_w - T_s)}{\sigma_{LV}}$ gives a velocity scale of the vapor phase in the direction normal to the liquid vapor interface, which is approximately parallel to the heated surface. The latter $\frac{\sigma_{LV}}{\mu_V}$ gives a velocity scale of the vapor phase in the direction parallel to the liquid vapor interface. If the normal component of the velocity $\frac{k_V(T_w - T_s)}{\sigma_{LV}}$ exceeds the tangential component $\frac{\sigma_{LV}}{\mu_V}$, a film of vapor can be sustained beneath the droplet. The transition to the Leidenfrost regime therefore occurs at π_1 around order one.

The second dimensionless number Π_2 represents the ratio of the liquid-vapor surface tension and the latent heat of vaporization to the thermal conductivity and temperature of the vapor phase. The Leidenfrost regime should occur for small values of Π_2 , corresponding to low surface tension, high vapor thermal conductivity, high temperature and low latent heat of vaporization. With all else constant, a lower latent heat can trigger the Leidenfrost effect by increasing the rate of vaporization to sustain a stable film [79].

Physically, Π_2 compares the specific energies h_{LV} and $\frac{k_V^2(T_w - T_s)^2}{\sigma_{LV}^2}$. The energy scale h_{LV} gives the specific latent heat needed to sustain vaporization at steady state. The latter $\frac{k_V^2(T_w - T_s)^2}{\sigma_{LV}^2}$ represents the energy scale for heat conducted to the liquid-vapor interface. If the conducted heat $\frac{k_V^2(T_w - T_s)^2}{\sigma_{LV}^2}$ that reaches the interface exceeds the specific latent heat h_{LV} , a vapor film can be sustained beneath the liquid. The transition to the Leidenfrost regime may thus occur for Π_2 around order one.

2.5.2. Molecular dynamics

Molecular dynamics simulations were implemented using LAMMPS [104] software. 33573 molecules of liquid water were initially equilibrated at saturation temperature in the canonical ensemble with constant pressure (1 atm) imposed by a piston constrained to move only in the direction orthogonal to the bottom surface [82]. The solid plate was constructed using a graphene sheet with armchair lattice orientation, and the interaction between the solid substrate and the SPC/E water molecules was governed by the 6-12 Lennard Jones pair potential with the depth of the potential well ranging from 0.01 to 0.15 kcal/mole. After equilibration, the liquid adjacent to the bottom surface was heated to a target temperature around the LFP, whereas the liquid adjacent to the piston was maintained at constant, saturation temperature to simulate nonequilibrium heat transfer conditions [83]. Vapor film thicknesses above the Leidenfrost point ranged from 10 to 25 nm over simulation times spanning 7 to 12 ns. The lateral simulation box size in the plane of the surface and piston was 8 nm by 8 nm. The vertical direction was allowed to grow as the vapor film evolved in time.

2.5.3. Relationship between the Hamaker constant and the equilibrium separation

The heterogeneous contact separation have been estimated as the arithmetic or geometric mean of the homogeneous values [102], although these means may not provide a good approximation for the actual H_{SVL} in general. Nonetheless, for our theory to be physically consistent, the heterogeneous contact separation corresponding to the experimental

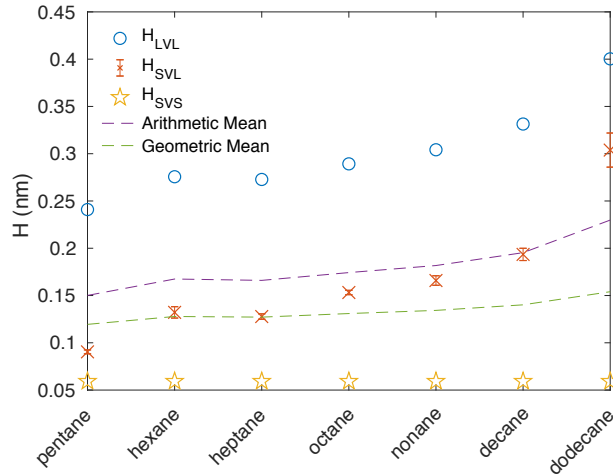


Figure 2.7. The equilibrium contact surface separation for the fluid (alkanes), surface (gold) and the heterogeneous value corresponding to the Leidenfrost point. Note that the equilibrium separation H_{LVL} is reported at the respective Leidenfrost temperatures of each alkane species, whereas Drummond et. al. listed H_{LVL} at the same temperature. The temperature dependence of H_{SVS} is assumed to be small over the range of temperatures corresponding to the LFP of the alkane series [85, 86], which is much lower than the melting point of gold.

Leidenfrost temperatures must be between the two bounding homogeneous values. Figure 2.7 shows that for the alkane family, this condition $H_{SVS} < \delta \approx H_{SVL} < H_{LVL}$ is satisfied, and the arithmetic and geometric means provide a reasonable estimate to the actual heterogeneous value.

Drummond has shown that as the chain length of the alkane species increases, the contact angle increases correspondingly. This suggests that longer chain alkanes in the liquid phase have unfavorable energetic interactions with a given substrate (greater liquid-solid surface energy σ_{SL}) compared to small chain alkanes on the same solid material. The heterogeneous, equilibrium distance H_{SVL} therefore tends to increase with the straight

chain length of the alkane species, moving from near the solid separation H_{SVS} toward the liquid value H_{LVL} .

2.5.4. Derivation of the diffusive equation

We begin with the general formulation of the vertical film boiling setup, taking into account only the diffusive terms in the steady momentum and energy conservation equations:

$$(2.52) \quad \frac{\partial \bar{u}_V}{\partial x} + \frac{\partial \bar{v}_V}{\partial y} = 0$$

$$(2.53) \quad 0 = -\frac{1}{\rho_V} \frac{\partial \bar{\Phi}}{\partial x} + \frac{f_d}{\rho_V} + \frac{\mu_V}{\rho_V} \frac{\partial^2 \bar{u}_V}{\partial y^2}$$

$$(2.54) \quad 0 = \frac{k_V}{\rho_V c_{p,V}} \frac{\partial^2 \bar{\Theta}_V}{\partial y^2}$$

where f_d is a buoyancy driven force dependent on the system configuration. As before, the boundary conditions at the superheated wall and the liquid-vapor interface at $\bar{\delta}(x)$ are given by:

$$(2.55) \quad \text{at } y = 0, \quad \bar{u}_V = \bar{v}_V = 0, \quad \bar{\Theta}_V = 1$$

$$(2.56) \quad \text{at } y = \bar{\delta}, \quad \bar{u}_V + \bar{v}_V \frac{d\bar{\delta}}{dx} = 0, \quad \bar{\Theta}_V = 0$$

while the phase change equation at the interface is written as:

$$(2.57) \quad \rho_V \frac{\partial \bar{\delta}}{\partial t} + \frac{\partial}{\partial x} \int_0^{\bar{\delta}} (\rho_V \bar{u}_V dy) = -\frac{k_V}{h_{LV}} \frac{\partial \bar{\Theta}_V}{\partial y} \Big|_{y=\bar{\delta}}$$

The base solution for the velocity field as found using an integral expansion is identical to our prior solution to the boundary layer equations:

$$(2.58) \quad u = a_0 + a_1\eta + a_2\eta^2 = \frac{f_d\delta^2}{2\mu_v}(\eta - \eta^2)$$

The temperature field in the base solution is linear, as expected from a diffusive approximation:

$$(2.59) \quad \Theta = b_0 + b_1\eta + b_2\eta^2 = 1 - \eta$$

The corresponding perturbed solutions are:

$$(2.60) \quad u' = a'_0 + a'_1\eta + a'_2\eta^2 = \left(\frac{f_d\delta\delta'}{2\mu_v} - \frac{\partial\Phi'}{\partial x}\frac{\delta^2}{2\mu_v}\right)\eta + \frac{\partial\Phi'}{\partial x}\frac{\delta^2}{2\mu_v}\eta^2$$

$$(2.61) \quad \Theta' = b'_0 + b'_1\eta + b'_2\eta^2 = \frac{\delta'}{\delta}\eta^2$$

The variation of the film thickness in the streamwise direction is found from eqn. 2.57 after assuming time invariance in the base state:

$$(2.62) \quad \delta = \left(\frac{16k_v\Delta T\mu_v}{\rho_v h_{LV} f_d} x\right)^{\frac{1}{4}}$$

Note that compared with the solution for the film thickness obtained from the boundary layer equations, eqn. 2.64 is missing the term $-\frac{1}{3}\frac{c_{PV}\Delta T}{h_{LV}}$. This is expected given only conduction is consumed in the thin film limit.

Linearizing the phase change conservation condition (eqn: 2.57) at the interface we obtain:

$$(2.63) \quad \rho_v \frac{\partial \delta'}{\partial t} + \frac{\partial}{\partial x} \int_0^\delta \rho_v u'_v dy + \frac{\partial}{\partial x} \int_0^{\delta+\delta'} \rho_v u_v dy = - \frac{k\Delta T}{h_{LV}} \left(\delta' \frac{\partial^2 \Theta}{\partial y^2} \Big|_\delta + \frac{\partial \Theta'}{\partial y} \Big|_\delta \right)$$

The change in δ' is obtained after substituting in the expressions for u' and Θ' (eqn: 2.60 and 2.61 respectively):

$$(2.64) \quad \rho_v \frac{\partial \delta'}{\partial t} + \frac{\rho_v f_d \delta^2}{4\mu_v} \frac{\partial \delta'}{\partial x} + \frac{\rho_v \delta^3 \sigma}{12\mu_v} \frac{\partial^4 \delta'}{\partial x^4} + \frac{\rho_v A}{24\pi\mu} V \delta \frac{\partial^2 \delta'}{\partial x^2} + \frac{k_v \Delta T}{h_{LV} \delta^2} \delta' = 0$$

Expressing in terms of normal modes:

$$(2.65) \quad \delta' = \delta'_a \exp(i(kx + \omega t))$$

where for brevity we take $\delta'_a \rightarrow \delta'$. This gives us:

$$(2.66) \quad i\omega = - \frac{k_v \Delta T}{h_{LV} \delta^2 \rho_v} - \frac{\delta^3 \sigma}{12\mu_v} k^4 + \frac{A}{24\pi\mu_v \delta} k^2 - i \frac{f_d \delta^2}{4\mu_v} k$$

After substituting in the set of dimensionless numbers introduced previous, we recover the diffusive expression (eqn. 2.38). The validity of this diffusive formulation is justified by observing that the maximum Peclet number Pe and Reynolds number Re for both liquid and vapor phases are on the order of $\max(Re_{vap}, Re_{liq})=10^{-6} \ll 1$ and $\max(Pe_{vap}, Pe_{liq})=10^{-8} \ll 1$. At the film thickness length scale where van der Waals interactions

are significant, the velocity and temperature fields are viscous and conduction dominated, respectively.

2.5.5. Nanoscale implications

Given that the phenomenon is localized in the nanoscale regime, it is important to discuss the applicability of the Navier-Stokes equations in the context of $O(1)$ in the Knudsen number (Kn). Hadjiconstantinou showed that the second order Knudsen layer correction is qualitatively robust well beyond $Kn \approx 0.4$, such that the underlying Navier-Stokes constitutive laws captures the behavior of arbitrary flows in spite of superimposed kinetic corrections in the flow field [84].

Here, the base solutions for velocity (eqn. 2.58) and temperature (eqn. 2.59) for the diffusive equation above are represented by the lowest order polynomials possible, given the buoyancy force in the momentum equation and no heat source in the energy equation. An examination of the system from a time and spatially averaged statistical standpoint would give us similar profiles with an effective slip and temperature jump at the interfaces, giving rise to effective viscosities and thermal conductivities that converge to the continuum values as the film thickness is increased.

It would be of great interest and rigor to frame the film stability problem in the context of a linearized Boltzmann analysis to accommodate larger Kn flows; however, the excellent agreement between the present, simplified model with experiment suggests the dominant effects governing the Leidenfrost film stability is captured despite the absence of statistical analyses describing intermolecular collisions. Additionally, the granularity

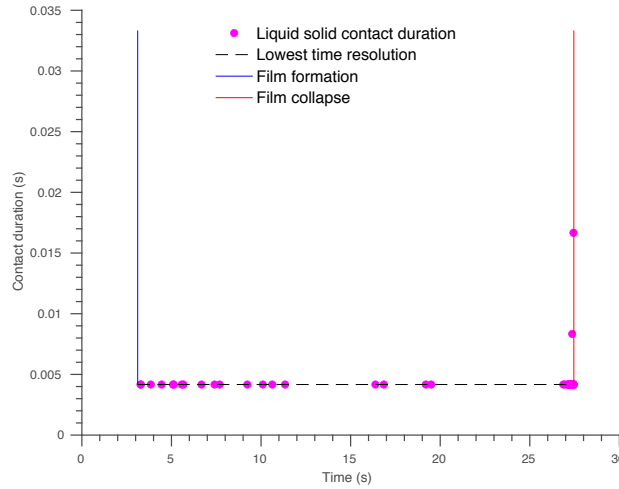


Figure 2.8. Residence time and frequency of liquid-solid contact in X-ray imaging [103].

of linear Boltzmann equation may obscure the effect of surface tension and van der Waals interactions, which have been shown to be important factors in pinpointing the LFP.

2.5.6. Time scale comparisons

Around the critical stability point $\pi_{LP}=1$ (eqn. 2.40), the real part of the temporal growth rate $\text{Re}(i\omega)$ is on the order of ± 10 (1/ns), depending on whether the film is stable $\pi_{LP} < 1$ or unstable $\pi_{LP} > 1$. Figure 2.8 shows the liquid contact time scales of a typical film boiling scenario from X-ray imaging [103]. Liquid-solid contact occurs intermittently after the film forms, and contact usually lasts ≤ 0.00417 s, the minimum time resolution of the experimental procedure; this qualitatively agrees with the temporal growth rate predicted by theory, which can be converted to contact durations on the order of 10 picoseconds for stable films. Both contact frequency and contact duration rise sharply near the collapse point. Note that upon examining the sequential images, the longer contact duration reported right before collapse does not stem from extended contact at a single location,

but from multiple touching/vaporizing cycles at different locations occurring sequentially or near simultaneously.

2.5.7. Corresponding states

We can use the correlations based on the corresponding states principle to estimate fluid properties such as thermal conductivity and surface tension. The resulting corresponding states expression for the diffusive approximation (eqn. 2.38) is a function of the molar mass m in (g/mol), estimated film thickness δ (around 10^{-9} m), the critical temperature T_c and pressure p_c , the applied saturation pressure p , the molar gas constant R , the Avogadro's number N , the saturation temperature T_{sat} , the dipole moment d , and the liquid-vapor contact angle θ of the solid substrate [106, 98, 99]:

$$(2.67) \quad \pi_{LP} =$$

$$\frac{[Q]}{p(mT)^2(T - T_{sat})(T_c - 1.T_{sat}) \left(\frac{0.0000175456d^4}{(T_c V_c)^2} + 1 \right)^2}$$

where

$$\begin{aligned}
 (2.68) \quad [Q] &= 6.95963 \times 10^{11} \delta p_c^{2/3} T T_c^{4/3} V_c^{4/3} \\
 &\left(2.16178 e^{-\frac{5.74143T}{T_c}} + 0.52487 e^{-\frac{1.82096T}{T_c}} + \frac{1.02251}{\left(\frac{T}{T_c}\right)^{0.14874}} \right)^2 \\
 &\quad \left(1 - \frac{T}{T_c} \right)^{1.60222} (\cos(\text{thet}) + 1)^2 \\
 &\quad (0.1196 T_{sat} \log(p_c) - 0.1594 T_c - 1.22909 T_{sat}) \\
 &\quad \left([P] + \frac{m^2 p V_c^2 (p - 81 p_c) + 6000 m p R T V_c + 9000000 R^2 T^2}{[P]} \right. \\
 &\quad \left. + m p V_c + 3000 R T \right)
 \end{aligned}$$

where

$$\begin{aligned}
 (2.69) \quad [P] &= \left(m^3 p^3 V_c^3 + 243 m^3 p^2 p_c V_c^3 + 4500 m^2 p R T V_c^2 (2p - 81 p_c) \right. \\
 &\quad + 27 \left(m^3 p^2 p_c V_c^3 \left(m^3 p V_c^3 (p + 27 p_c)^2 + 9000 m^2 p R T V_c^2 (p - 45 p_c) \right. \right. \\
 &\quad \quad \left. \left. + 6750000 m R^2 T^2 V_c (4p - 9 p_c) \right. \right. \\
 &\quad \quad \left. \left. + 27000000000 R^3 T^3 \right) \right)^{\frac{1}{2}} + 27000000 m p R^2 T^2 V_c \\
 &\quad \left. + 27000000000 R^3 T^3 \right)^{\frac{1}{3}}
 \end{aligned}$$

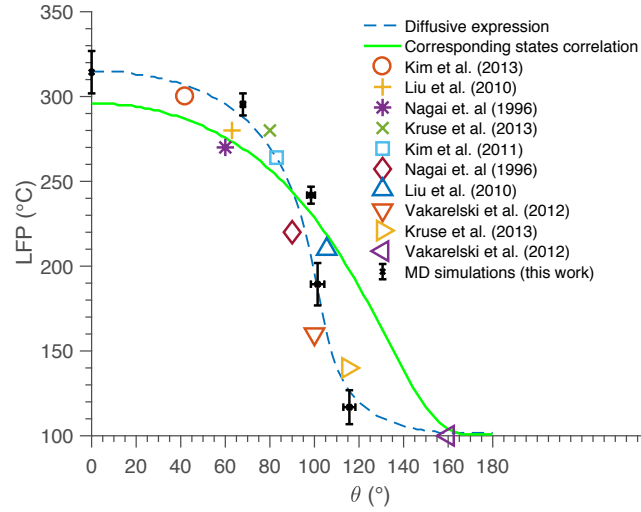


Figure 2.9. The Leidenfrost temperature vs the contact angle for water, from experiments [58, 42, 59, 41, 60], the diffusive prediction of the LFP (eqn. 2.43), molecular dynamics simulations from this work, and the corresponding states correlation (eqn. 2.67)

Eqn. 2.67 may provide a more convenient estimate for the LFP given that no tabulation of fluid properties as a function of temperature and pressure is necessary. Fig. 2.9 shows that the corresponding states correlation adequately represents the LFP over the range of liquid-vapor contact angles for water.

Fluid	Experimental LFP ($^{\circ}\text{C}$)	LFP ($^{\circ}\text{C}$) (eqn: 2.67)
Carbon tetrachloride	158.9 [[78]]	156..9
FC-72	90 [[101]]	78.9

We can approximate the liquid spinodal temperature T_{sp} via [100]:

$$(2.70) \quad T_{sp} = T_c \left(0.923 - \frac{287226}{\left(\log \left(\frac{p}{p_c} \right) - 5.3727 \right)^9} \right)$$

For all fluids tested, $T_{LFP} \lesssim T_{sp}$, such that the predicted, maximum Leidenfrost point at 0° contact angle generally falls below or near the superheat spinodal limit within the error introduced by the corresponding states correlations. There appears to be general consistency between the LFP estimate and the thermodynamic limit of liquid stability [87, 88, 89].

2.5.8. General assumptions

2.5.8.1. Vapor properties. First, it is important to consider whether density changes with temperature are significant. All flow conditions are such that the Mach number is small, and the Boussinesq approximation is valid. The Mach number for the current system is on the order of 10^{-6} . Hence, constant density incompressible flow assumption is reasonable.

We assume for simplicity that the vapor field properties can be represented as a constant value for a given wall/vapor film/liquid system with prescribed wall temperature T_W and interface saturation temperature T_S . Then we have the following choices for the temperature at which the vapor field properties are computed.

We can choose the temperature T_S , which means the only temperature dependent term in the LHS (left hand side) of equation 2.42 is $1/\Delta T$. We can also pick the temperature $(T_S + T_V)/2$ or use another type of averaging. Lastly, we can select the temperature T_W (as done prior). The wall temperature T_V such that $\text{LHS}(T_V) = 1$ corresponds to the LFP ($T_V = \text{LFP}$).

In short, the selection for the temperature corresponding to the constant vapor field properties was made after comparing the derived stability condition (eqn. 2.43) with

available fluid properties data and LFP experimental data. A priori, there is no clear ‘correct’ choice between the three options. It appears that the dominant contribution to film stability in the vapor domain stems from the near wall region where the vapor locally attains properties corresponding to the wall superheat.

2.5.8.2. Supercooling and roughness. Experimental observations show that ambient subcooling of the liquid reservoir can significantly affect the LFP for pool boiling, but not for drops on a surface [78, 92, 93]. A theoretical treatment of subcooling effects therefore not only requires additional complexity, but also separate models for the two boiling modes; this treatment is outside the scope of the current analysis. We refer to models in the literature for the effect of subcooled liquid reservoirs on rough surfaces [95], which capture the incipience of intensive heat transfer due to contact between liquid wave crests and surface roughness.

Periodically textured substrates which have been shown to have a strong effect on the LFP as well as the measured, effective temperature at the solid interface [97, 90, 91]. The general effect of surface roughness on the measured LFP is unavoidable; nevertheless, we can average out this effect by considering surfaces with random roughness instead of deliberate, repeated features or hierarchical structures.

This work focuses on understanding the baseline saturated pool boiling scenario for which data are abundant. The next goal should be to extend this work to include the effect of subcooling and optimized textures such as on superhydrophilic surfaces. Both these effects require an independent focused investigation. For example, note that the effect of optimized (as opposed to random) roughness and subcooling may lead to unexpected

supercritical Leidenfrost behavior as reported in prior literature [94, 96]. This remains an open question that is beyond the scope of this work.

2.5.8.3. Marangoni effect. Lastly, Bénard-Marangoni convection or phenomenon arising from gradients in surface tension may influence film stability. However, this would be a smaller effect in this work since the Marangoni number is on the order of 10^{-4} to 10^{-1} . This is further supported by good agreement between the theoretical predictions, that do not have Marangoni effects, and experimental data. Therefore, extending this analysis to include the Marangoni effect is out of the scope of the current work.

CHAPTER 3

Interface temperature

What is the interface temperature during phase transition (for instance, from liquid to vapor)? This question remains fundamentally unresolved. In the modeling of heat transfer problems with no phase change, the temperature and heat flux continuity conditions lead to the interface temperature. However, in problems with phase change, the heat flux condition is used to determine the amount of mass changing phase. This makes the interface temperature indeterminate unless an additional condition is imposed. A common approach in the modeling of boiling is to assume that the interface attains the saturation temperature according some measure of pressure at the interface. This assumption is usually applied even under highly non-equilibrium scenarios where significant temperature gradients and mass transport occur across the interface. In this work, an ab-initio thermodynamic principle is introduced based on the entropy production at the interface that fully specifies the associated temperature under non-equilibrium scenarios. Physically, the thermodynamic principle provides a theoretical limit on the space of possible phase change rates that can occur by associating the mass flux with a corresponding interfacial entropy production rate; a stronger statement is made that a system with sufficient degrees of freedom selects the maximum entropy production, giving the observed phase change rate and associated interface properties. This entropic principle captures experimental and computational values of the interface temperature that can deviate by over 50% from the assumed saturation values. It also accounts for temperature jumps

(discontinuities) at the interface whose difference can exceed 15°C . This thermodynamic principle is found to appropriately complete the phase change problem.

3.1. Introduction

In phase transition (e.g. liquid to vapor), the fundamental principle that dictates the temperature at the interface between the two phases has been debated and it remains an open question.

The interface temperature determines the rate of phase change in a heat transfer system. Thus, pinpointing the interface temperature from a reliable, ab-initio analysis is critical in designing and optimizing a variety of phase change applications, including water purification processes like membrane distillation, [107] energy storage systems using latent heat batteries,[108] additive manufacturing techniques involving molten metal jets, [109], and phase change memory technologies for nonvolatile solid state storage.[110]

Theoretical and computational models typically assume that the interface between the two phases attains the saturation temperature.[111, 112] Experimental work using thermocouples with thicknesses on the order of microns [113, 114] have resolved interface temperatures that are found to deviate significantly from the saturation assumption.[111] Theoretical attempts to find a different interface condition, to replace the saturation temperature condition, include the kinetic theory [115, 111] and the statistical rate theory.[116]

Kinetic theory expresses the entropy generation at the interface using a constitutive relationship with the parameter ϕ representing the kinetic mobility, or the relative strength of molecular attachment to a surface. However, the evaluation of ϕ requires an empirical

evaporation coefficient α , which is difficult to measure and can deviate by over three orders of magnitude from the theoretical value of unity.[111, 113] The kinetic theory also underestimates the temperature jump measured in experiment by 3 to 4 orders of magnitude.[114]

The statistical rate theory uses quantum mechanics to describe a relationship between the rate of phase change and the change in entropy associated with a molecule transferring from the liquid to the vapor phase.[116] After measuring the interface properties (including temperatures) of the liquid and vapor side from experiment, the mass flux from phase change can be calculated based upon the material properties of the fluid, the molecular vibrational frequencies and the partition function for the fluid molecule. From a computational standpoint or generally in scenarios where the interface temperatures and properties are not known a priori, the rate of phase change cannot be obtained via this method and vice versa.

In this work, we determine the thermodynamic relationship between the temperatures of both phases at the interface and the rate of interfacial entropy production Δ . This framework provides a theoretical limit on the space of possible interface temperatures and phase change rates; there exists a maximum rate of entropy production due to the competition between the entropy jump from phase change and the contribution to entropy change due to heat flux away from the interface. This space of possible Δ is bounded from below by the second law of thermodynamics $\Delta \geq 0$.

Finally, we propose a stronger thermodynamic principle that fully determines the interface temperatures during the time evolution of a phase change system. It is found that the interface temperatures which maximize the entropy production rate Δ capture

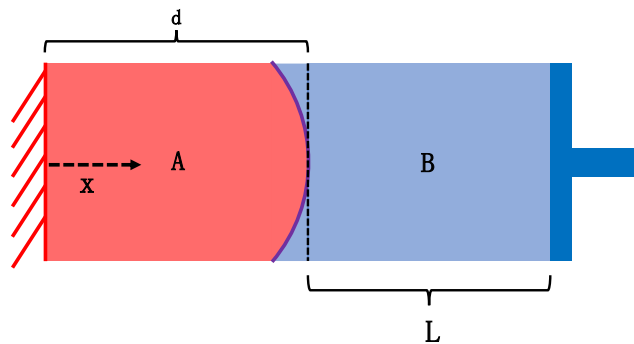


Figure 3.1. Finite, one-dimensional system with two fluid components A and B . The interface between the two phases is located at $x = d[t]$. A motionless wall bounds the domain at $x = 0$, and a moveable piston at $x = L[t] + d[t]$ controls the pressure in the system. The wall is held at constant temperature T_W and the piston at temperature T_P . The radius of curvature of the interface R can be nonzero.

the full range of both experimental and computational data of different fluids and solids under evaporation, condensation, and freezing processes. This thermodynamic principle prefaced on the maximum rate of entropy production [117, 118] also determines the rate of phase change as a function of material properties and temperature boundary conditions in the far field; properties and field variables at the interface are not known or fixed a priori.

The proposed entropy condition closes the formerly incomplete problem of phase change under nonequilibrium scenarios.

3.2. The missing interface condition

3.2.1. The complete problem without phase change

We first consider a well-posed problem comprising a two component system in which no phase change can occur (for instance, with water and oil). Fig. 4.1 shows a finite, one-dimensional system where the number of equations and boundary conditions can be easily

counted. The governing equations for the incompressible species A and B across the two phase interface are

$$(3.1) \quad \frac{\partial u_c}{\partial x} = 0,$$

$$(3.2) \quad \rho_c \frac{\partial u_c}{\partial t} = -\frac{\partial p_c}{\partial x},$$

$$(3.3) \quad \rho_c c_{p,c} \frac{\partial T_c}{\partial t} + \rho_c c_{p,c} u_c \frac{\partial T_c}{\partial x} = k_c \frac{\partial^2 T_c}{\partial x^2},$$

where the subscript $c \in \{A, B\}$. The velocities, pressures and temperatures in each phase are denoted u_c , p_c , and T_c respectively. Similarly, k_c , ρ_c and $c_{p,c}$ refer to the thermal conductivity, density and specific heat capacity at constant pressure. The boundary conditions at the motionless wall are

$$(3.4) \quad \text{at } x = 0, \quad u_A = 0,$$

$$(3.5) \quad T_A = T_W.$$

The boundary conditions at the piston are

$$(3.6) \quad \text{at } x = L[t], \quad p_B = p_P,$$

$$(3.7) \quad T_B = T_P.$$

The interface conditions are

$$(3.8) \quad \text{at } x = d[t], \quad \rho_A(u_A[d] - u_S) - \rho_B(u_B[d] - u_S) = \dot{m}_A + \dot{m}_B = 0,$$

$$(3.9) \quad \dot{m}_A = -\dot{m}_B = 0,$$

$$(3.10) \quad \llbracket Q \rrbracket = -k_B \frac{dT_B}{dx} \Big|_{d[t]} + k_A \frac{dT_A}{dx} \Big|_{d[t]} = 0,$$

$$(3.11) \quad T_A[d] = T_{SA} = T_{SB} = T_B[d],$$

$$(3.12) \quad p_A = p_B + \gamma\kappa,$$

where u_S is the interface velocity, T_W is the wall temperature, T_P is the piston temperature, p_P is the piston pressure, and $\llbracket Q \rrbracket$ is the jump in heat flux across the interface, γ is the surface tension between the two species and κ is the interface curvature ($\kappa = 1/R$ in one dimension). The temperatures T_{SA} , T_{SB} represent the respective values for each species A, B at the two-phase interface. Note that in this section only, we have assumed for simplicity that the interface is massless, surface tension is constant, and there is no temperature jump across the interface (eqn. 3.11) [111].

Here, eqn. 3.8 comprises the mass conservation condition at the interface by stating that mass flux of phase A entering the interface must equal the mass flux of phase B leaving it; there is no mass source or accumulation at the interface. Eqn. 3.9 describes the no phase change condition. The two phases are taken to be immiscible such that mass

from one side of the interface cannot move to the other by any process other than phase change. Eqn. 3.10 and eqn. 3.12 refers to energy and momentum conservation at the interface, respectively.

There are 6 unknown field variables ($u_A, T_A, p_A, u_B, T_B, p_B$) and six sets of conservation equations (eqn. 3.1, 3.2, 3.3) for components A and B. The four mass and momentum conservation equations (eqns. 3.1 and 3.2 for components A and B) are first order differential equations that each require a single boundary condition (eqn. 3.4, 3.6, 3.8, 3.12). The two energy equations (eqn. 3.5 for components A and B) are second order differential equations that each require two boundary conditions (eqn. 3.5, 3.7, 3.10, 3.11). Without phase change, the mass continuity condition at the interface (eqn. 3.9) specifies the interface velocity $u_S = u_A[d] = u_B[d]$ and completes the problem.

3.2.2. The ill-posed problem with phase change

Consider a scenario where phase change occurs between the two species (for instance, with liquid water and water vapor). The governing equations are the same, but the interface conditions change [119, 111, 120]. Conservation of mass at the interface states

$$(3.13) \quad \text{at } x = d[t], \quad \rho_A(u_A[d] - u_S) - \rho_B(u_B[d] - u_S) = \dot{m}_A + \dot{m}_B = 0.$$

From energy balance at the interface, the mass flux due to phase change is given as [119]

$$(3.14) \quad \dot{m}_A = \frac{[[Q]]}{H}.$$

The temperatures of the two phases at the interface are assumed to be continuous in this section, such that

$$(3.15) \quad T_A[d] = T_{SA} = T_{SB} = T_B[d].$$

Momentum conservation at the interface gives

$$(3.16) \quad p_A = p_B + \gamma\kappa + (1/\rho_A - 1/\rho_B) \left(\frac{[[Q]]}{H} \right)^2,$$

where viscous terms are zero in the momentum conservation eqn. 3.16 in the 1D limit [119]. Here, $H = h_A - h_B$ is the latent heat of phase change expressed as the difference between the enthalpy of phases A and B, h_A and h_B respectively.

As the mass flux across the interface is not identically equal to zero due to phase change between species A and B, eqn. 3.9 can no longer be applied. Thus, the interface velocity u_S becomes unspecified. The energy conservation condition eqn. 3.14 at the interface can be borrowed to determine the mass flux, which is fixed by the thermal energy diffused to the interface relative to the latent heat of phase change. Knowing m_A gives u_S via the continuity condition eqn. 3.13.

However, if the energy conservation condition is used to find the interfacial velocity u_S , the interface temperature T_S becomes unspecified; one of these two variables must be known a priori in order to determine the other with eqn. 3.14. A phase change problem is therefore ill-posed due to either the missing interface velocity or temperature.

3.3. The entropy condition at the two-phase interface

The entropy condition at the two phase interface has been explored in the literature [120], but the resulting statement on the interfacial entropy production rate Δ (in units of energy per unit temperature, per unit time, and per unit area) is weak when referencing the second law of thermodynamics in or near equilibrium: $\Delta \geq 0$. We refer to this inequality as weak in that it is not sufficient to specify a particular interface temperature or velocity. Additionally, the statement of the second law leaves the entropy production rate unbounded in a semi-infinite range.

In this section, we will first present a general evolution equation for the entropy production rate across a two phase interface in the absence of electromagnetic phenomena. Then for evolution of a two-phase system, it can be physically shown that the entropy production term is bounded from above by a finite maximum value. The range for Δ therefore also becomes finite, leading to a stronger statement on the possible macrostates accessible to the system.

The rate of entropy production Δ at the two phase interface is given by [120]

$$\begin{aligned}
 (3.17) \quad (T_S)\Delta = & \dot{m}_A \left((T_{SA} - T_S)s_A + g_A - g_S + 0.5(\mathbf{v}_A \cdot \mathbf{v}_A - 2\mathbf{v}_A \cdot \mathbf{v}_S + \mathbf{v}_S \cdot \mathbf{v}_S) \right) \\
 & + \dot{m}_B \left((T_{SB} - T_S)s_B + g_B - g_S + 0.5(\mathbf{v}_B \cdot \mathbf{v}_B - 2\mathbf{v}_B \cdot \mathbf{v}_S + \mathbf{v}_S \cdot \mathbf{v}_S) \right) \\
 & + \mathbf{q}_A \cdot \hat{\mathbf{n}}_A (1 - T_S/T_{SA}) + \mathbf{q}_B \cdot \hat{\mathbf{n}}_B (1 - T_S/T_{SB}) + T_S \mathbf{q}_S \cdot \nabla_S (1/T_S) \\
 & - \frac{\dot{m}_A}{\rho_A} (\boldsymbol{\tau}_A \cdot \hat{\mathbf{n}}_A) \cdot \hat{\mathbf{n}}_A - \frac{\dot{m}_B}{\rho_B} (\boldsymbol{\tau}_B \cdot \hat{\mathbf{n}}_B) \cdot \hat{\mathbf{n}}_B,
 \end{aligned}$$

where T_{SA} and T_{SB} are the absolute temperatures of the respective phases at the interface, and T_S is the absolute interface temperature. Similarly, the variables $g_{A,B,S}$ are the free

enthalpies, $s_{A,B}$ are the entropies per unit mass and $\mathbf{q}_{A,B,S}$ are the heat fluxes. The unit normal vectors $\hat{\mathbf{n}}_A$ and $\hat{\mathbf{n}}_B$ are directed towards the interface [120, 121]. The stress tensors in each species are given by $\boldsymbol{\tau}_{A,B}$, while the surface gradient is represented by ∇_S . Finally, the mass fluxes across the interface are denoted as $\dot{m}_A = \rho_A(\mathbf{v}_A - \mathbf{v}_S) \cdot \hat{\mathbf{n}}_A$ and $\dot{m}_B = \rho_B(\mathbf{v}_B - \mathbf{v}_S) \cdot \hat{\mathbf{n}}_B$. Eqn. 3.17 for the entropy source term comes from combining the conservation laws for mass, momentum, energy with the evolution equation for entropy at the interface [120].

Next, we can find a simplified expression for the entropy production rate Δ_1 in a 1D system across a massless, infinitesimally thin interface (Fig. 4.1). Let $c \in \{A, B\}$. By definition, the sum of the free enthalpy g_c and the product of temperature with the entropy density $T_{Sc} s_c$ of each phase is simply the saturation enthalpy, since the temperature and pressure dependencies of the two terms cancel to give

$$(3.18) \quad g_c + T_{Sc} s_c = \left(g_{c,\text{sat}} + \frac{1}{\rho_c} (p - p_{\text{sat}}) \right) + \left(T_{Sc} s_{c,\text{sat}} [T_{Sc}] - \frac{1}{\rho_c} (p - p_{\text{sat}}) \right) = g_{c,\text{sat}} + T_{Sc} s_{c,\text{sat}} [T_{Sc}] = h_{c,\text{sat}}.$$

The mass flux across the interface due to phase change \dot{m} is specified by the energy balance equation at the interface (eqn. 3.14) with

$$(3.19) \quad \dot{m} = \frac{1}{h_{A,\text{sat}} - h_{B,\text{sat}}} (\mathbf{q}_A \cdot \hat{\mathbf{n}}_A + \mathbf{q}_B \cdot \hat{\mathbf{n}}_B) = -\dot{m}_A = \dot{m}_B.$$

Using eqn. 3.18, we can then start simplifying the full expression for the entropy production rate at the two phase interface to

$$(3.20) \quad \begin{aligned} T_S \Delta_{1D} = & \dot{m} (h_{B,\text{sat}} - h_{A,\text{sat}}) + (q_A - q_B) \\ & + \dot{m}(T_S s_A - T_S s_B) + q_A(-T_S/T_{SA}) - q_B(-T_S/T_{SB}) - \frac{\dot{m}^3}{2} \left(\frac{1}{\rho_A^2} - \frac{1}{\rho_B^2} \right), \end{aligned}$$

where $q_c = -k_c \frac{dT_c}{dx}|_d$. The \dot{m}^3 term follows from converting the dot product of the interfacial velocities into mass fluxes (eqn. 3.19). By noting that the first two terms on the right hand side have equal magnitudes but opposite signs with respect to energy conservation (eqn. 3.19), we can reduce the entropy production rate to

$$(3.21) \quad \Delta_{1D} = \dot{m}(s_A - s_B) + q_A(-1/T_{SA}) - q_B(-1/T_{SB}) - \frac{\dot{m}^3}{2T_S} \left(\frac{1}{\rho_A^2} - \frac{1}{\rho_B^2} \right).$$

In this 1D expression for the entropy production rate Δ_{1D} , all variables, fluxes and material properties are evaluated at the interface, and are therefore functions of the interfacial temperatures T_S, T_{SA}, T_{SB} and pressures p_A, p_B . On the other hand, the variation of each species' entropy density s_c with interface temperatures can only be specified after more information is known about the identity of each phase.

For the particular case of phase change between vapor (species V) and liquid (species L), the entropy densities can be expressed in terms of the pressure and temperature in each phase as

$$(3.22) \quad (T_{SV})s_V = (T_{SV})s_{V,\text{sat}} - RT_{SV} \ln \left(\frac{p_V}{p_{\text{sat}}[T_{SV}]} \right),$$

$$(3.23) \quad (T_{SL})_{s_L} = (T_{SL})_{s_{L,\text{sat}}} - \frac{1}{\rho_L} (p_L - p_{\text{sat}}[T_{SL}]),$$

where ρ_L is the density of the liquid phase, R is the specific gas constant and p_{sat} is the saturation pressure associated with the interface temperature T_{SV} or T_{SL} of each phase.

Following the 1D formulation of Δ_{1D} (eqn. 3.21), the entropy production rate at the interface of a vapor-liquid system becomes

$$(3.24) \quad \Delta_{LV}[T_{SV}, T_{SL}, T_S] = \underbrace{\dot{m} \left(s_{V,\text{sat}} - s_{L,\text{sat}} - R \ln \left(\frac{p_V}{p_{\text{sat}}[T_{SV}]} \right) + \frac{1}{T_{SL} \rho_L} (p_L - p_{\text{sat}}[T_{SL}]) \right)}_{\Delta_1 = \dot{m}(s_V - s_L)} - \underbrace{\frac{\dot{m}^3}{2T_S} \left(\frac{1}{\rho_V^2} - \frac{1}{\rho_L^2} \right)}_{\Delta_2} + \underbrace{q_V(-1/T_{SV}) - q_L(-1/T_{SL})}_{\Delta_3}.$$

Three terms contribute to the interfacial entropy production rate. Here, Δ_1 encapsulates the difference in phase entropies between the liquid and vapor, Δ_2 accounts for the kinetic energy contribution, and Δ_3 resolves the entropy change due to heat flux leaving the interface.

Additionally, this framework poses the question: what is a reasonable choice for T_S ? For simplicity, we take $T_S \approx T_{SL}$ in this work on the basis that the Knudsen layer in the liquid phase is significantly smaller than that in the vapor [114].

3.3.1. Physical insight into the existence of a maximum entropy production rate

The entropy production rate Δ at the two phase interface is bounded below by the second law of thermodynamics. In an 1D system, we now show that Δ is bounded above by a maximum, finite value. We will first provide a physical proof in a simplified system where each term can be clearly resolved before revisiting the general case defined by eqn. 3.24.

Consider the setup introduced in Fig. 4.1, where component A is water vapor (V) and component B is liquid water (L). The wall at $x = 0$ is superheated to temperature T_W , while the piston at $x = L$ is maintained at the saturation temperature $T_P = T_{\text{sat}}$ corresponding to the applied piston pressure $p = p_P$.

We make further assumptions to simplify the analysis and provide physical intuition into the competing effects that drive the entropy production rate to achieve a finite maximum value. First, the temperature profiles are taken to be linear in the vapor and liquid phases to estimate the interfacial heat fluxes; more sophisticated profiles can be assumed in the presence of heat or mass sources in the bulk phases [122]. Next, we take $T_S = T_{SV} = T_{SL}$, acknowledging that this should only hold in special instances such as when the system is in equilibrium. With this, the mass flux at the interface (eqn. 3.19) becomes

$$(3.25) \quad \dot{m} = \rho_L(u_S - u_L) = \frac{1}{H} \left(k_L \frac{T_P - T_S}{L} - k_V \frac{T_S - T_W}{d} \right).$$

Meanwhile, the entropy production rate at the interface (eqn. 3.24) is simplified to

$$(3.26) \quad \Delta_{LV}^s(T_S) = \underbrace{\dot{m}(s_V - s_L)}_{\Delta_1^s} - \underbrace{\frac{\dot{m}H}{T_S}}_{\Delta_3^s},$$

where we have neglected the cubic term in mass flux, since dimensional analysis shows that \dot{m} is much smaller in magnitude compared to the other terms. We will demonstrate this explicitly for the general 1D case. If the lengths d , L , the temperatures T_P and T_W as well as the piston pressure p_P in the far field are fixed, then Δ_{LV}^s is only a function of T_S .

As T_S increases, the magnitude of \dot{m} decreases along with the net heat transfer to the interface. Meanwhile, the difference $s_V - s_L$ decreases as well (eqn. 3.22 and 3.23) with larger T_S as the system moves towards the critical point [136, 137, 124]. Thus the difference between phase entropies Δ_1^s in the simplified interfacial entropy evolution Δ_{LV}^s is inversely proportional to the interface temperature.

The remaining term $-\frac{\dot{m}H}{T_S}$ is directly proportional to T_S . As the interface temperature increases, \dot{m} , H and $\frac{1}{T_S}$ all decrease, such that the negative of their product increases. This affirms a positive proportionality between the entropy change due to heat flux leaving the interface Δ_3^s and the interface temperature T_S . Due to the competition between Δ_1^s and Δ_3^s as T_S varies, the interfacial entropy production rate reaches a finite maximum value $\Delta_{LV,\max}^s$ at the interface temperature T_S^* , analogous to how the change in Gibbs free energy goes through a minimum in the classical heterogeneous nucleation theory due to the competition between surface tension and volumetric free energy as the radius of the nucleus changes [119, 164].

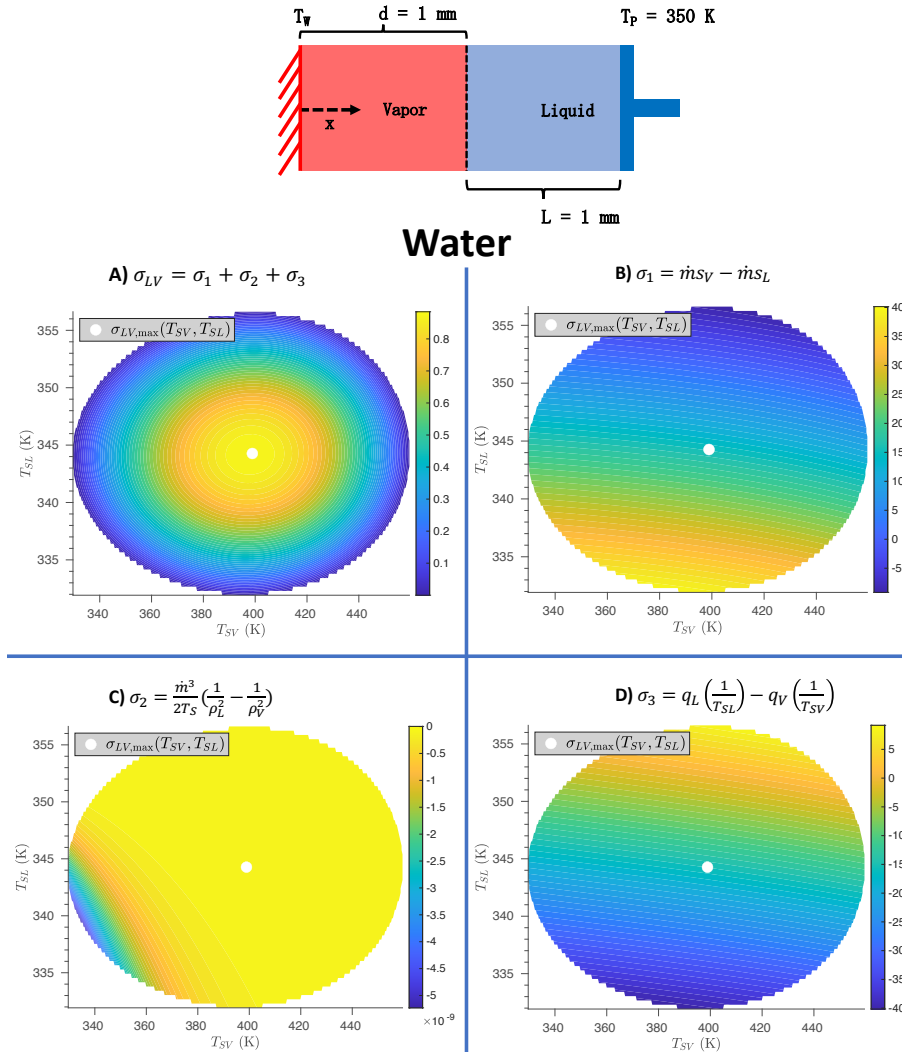


Figure 3.2. The components of the entropy production rate at the two phase interface are plotted as a function of the liquid and vapor side interface temperatures. The width of the vapor and liquid domains are both 1 mm. The piston cooling the liquid reservoir is held at a constant temperature 350 K and pressure 7.3×10^3 Pa, while the wall temperature heating the vapor is 389.4 K. **A)** The entropy production rate Δ_{LV} (eqn. 3.24) at the liquid-vapor interface reaches a maximum for finite values of the interface temperatures T_{SV} and T_{SL} . **B)** The first component of the entropy production rate Δ_1 arises from the difference in phase entropies between the liquid and vapor. This term decreases for larger values of T_{SV} and T_{SL} . **C)** The second component of the entropy production rate Δ_2 reflects the kinetic energy contribution. Due to the small mass flux \dot{m} relative to the other quantities, this term is negligible. **D)** The third component of the entropy production rate Δ_3 is due to heat transfer from the interface. This term increases for larger values of T_{SV} and T_{SL} . The opposite dependencies of Δ_1 and Δ_3 on T_{SV} and T_{SL} allow the interfacial entropy production rate to reach a maximum value at finite temperatures. The vapor and liquid properties of water (thermal conductivities, latent heat of phase change, etc.) as a function of temperature and pressure were referenced from the IAPWS formulation [136, 137, 124].

Fig. 3.4 shows that Δ_{LV}^s achieves a maximum value at a finite interface temperature T_S^* satisfying $T_{\text{sat}} < T_S^* < T_{\text{wall}}$, in agreement with our qualitative analysis of the simplified entropy production rate. As the distance between the superheated wall and the liquid-vapor interface increases from micro to macro length scales, the interface temperature T_S drops towards the saturation temperature corresponding to the applied piston pressure. This is accompanied by a shrinkage of the temperature range where $\Delta_{LV}^s \geq 0$, suggesting that the traditional assumption of saturation temperature at the interface is only valid at macroscale.

This analysis also holds true in general for $\Delta_{LV}[T_{SV}, T_{SL}, T_S = T_{SL}]$ (eqn. 3.24), which accounts for the discontinuous interface temperatures and the kinetic energy contribution, Δ_2 . Fig. 3.2C shows that Δ_2 remains negligible compared to the two remaining terms. Furthermore, Fig. 3.2B andD generalizes the competing relationship between the entropy difference of the two phases Δ_1 and the entropy change due to heat flux leaving the interface Δ_3 as the discontinuous interfacial temperatures vary. Their opposing dependencies on T_{SV} and T_{SL} allow the interfacial entropy production rate to reach a finite maximum value $\Delta_{LV,\text{max}}$ (Fig. 3.2A). The temperature regime where $\Delta_{LV} \geq 0$ is localized around this maximum. Thus, the one dimensional temperature range for $\Delta_{LV}^s \geq 0$ reflects a straightforward projection onto the diagonal of this two dimensional space comprising the discontinuous interface temperatures.

Outside the regime where the second law of thermodynamics is satisfied, Fig. 3.3 shows how the large magnitude of the negative phase entropy term Δ_1 drives $\Delta_{LV} < 0$ at greater interfacial temperatures, while Δ_3 induces $\Delta_{LV} < 0$ at lower interfacial

temperatures. For each set of boundary conditions, there are interfacial temperatures that are thermodynamically infeasible due to an imbalance between Δ_1 and Δ_3 .

3.3.2. The maximum entropy principle at the two-phase interface

Having demonstrated that the interfacial entropy production rate achieves a maximum, finite value for phase change systems, we now propose an entropic condition to determine the temperatures at the interface.

In nonequilibrium thermodynamics, it has been proposed that a process follows the path along which the entropy produced in the system at each step is maximized, subject to conservation laws as well as external constraints such as prescribed thermodynamic forces or fluxes [125].

The maximum entropy production principle (MEPP) therefore seeks to generalize the inequality formulation of the second law of thermodynamics, which only states that the entropy production is either positive for irreversible processes or zero for reversible ones [120]; alone, the second law gives a possible range of discontinuous interface temperatures T_{SA} and T_{SB} that satisfy $\Delta \geq 0$, but does not pinpoint an actual value for T_{SA} , T_{SB} .

MEPP has been explored with series of proofs in the literature ranging from variational analyses to statistical mechanics considerations [125, 118, 117, 126]. Functionally, MEPP can be used as a variational principle to solve the Boltzmann equation [125]; in climate models to predict surface temperatures and cloud coverage [127]; in solid state physics to predict dendritic structure and growth rates [128].

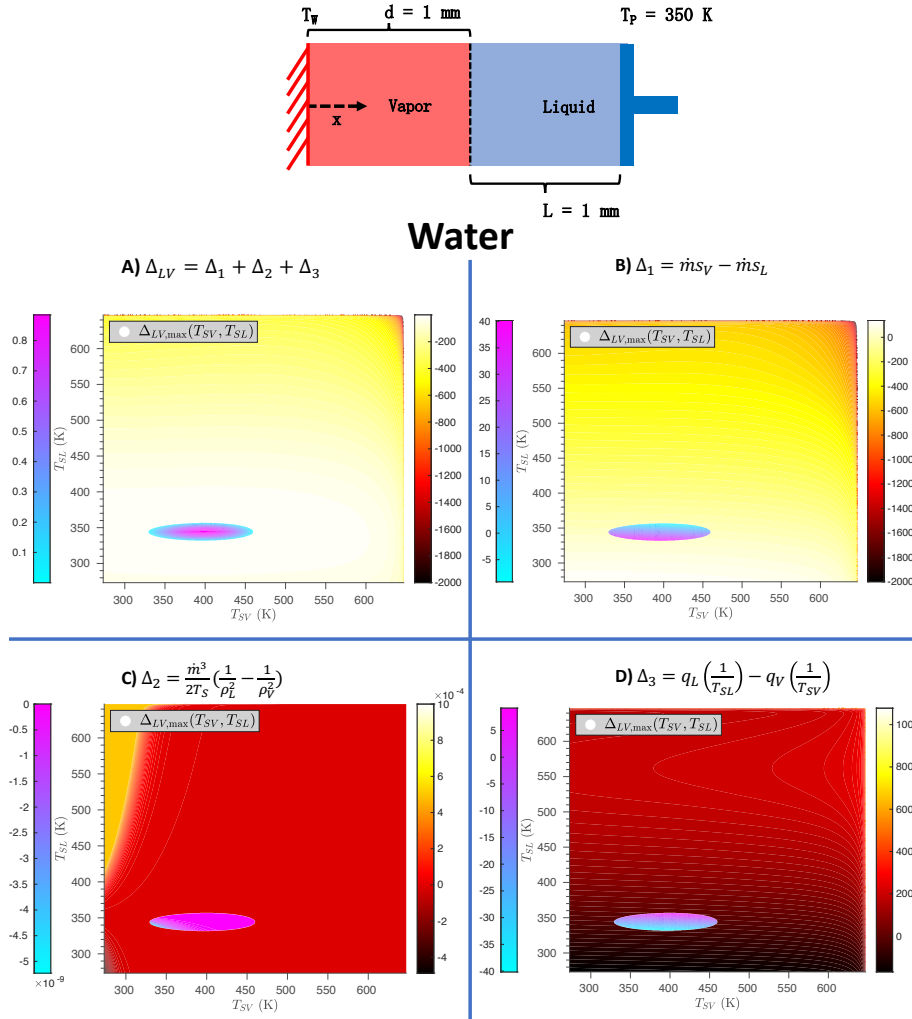


Figure 3.3. The components of the entropy production rate at the two phase interface are plotted as a function of the liquid and vapor side interface temperatures. The width of the vapor and liquid domains are both 1 mm. The piston cooling the liquid reservoir is held at a constant temperature 350 K and pressure 7.3×10^3 Pa, while the wall temperature heating the vapor is 389.4 K. **A)** The entropy production rate Δ_{LV} (eqn. 3.24) at the liquid-vapor interface is negative for interface temperatures T_{SV} and T_{SL} away from the maximum. These states are not thermodynamically accessible, but can be reached transiently under local violation of the second law of thermodynamics. **B)** The first component of the entropy production rate Δ_1 arises from the difference in phase entropies between the liquid and vapor. This term drives Δ_{LV} for larger values of T_{SV} and T_{SL} . **C)** The second component of the entropy production rate Δ_2 reflects the kinetic energy contribution. Due to the small mass flux \dot{m} relative to the other quantities, this term is negligible. **D)** The third component of the entropy production rate Δ_3 is due to heat transfer from the interface. This term drives Δ_{LV} for smaller values of T_{SV} and T_{SL} . The vapor and liquid properties of water (thermal conductivities, latent heat of phase change, etc.) as a function of temperature were referenced from the IAPWS formulation [136, 137, 124].

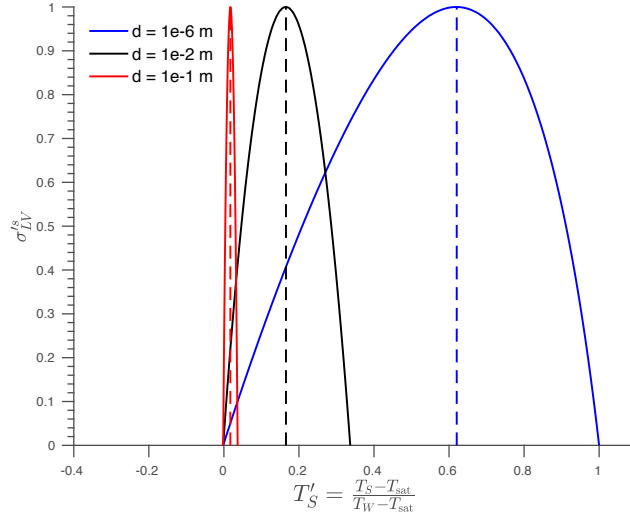


Figure 3.4. The entropy evolution at the interface (eqn. 3.26) normalized by the maximum value ($\Delta_{LV}^s = \frac{\Delta_{LV}^s}{\max(\Delta_{LV}^s)}$) as a function of the normalized interface temperature T'_S . The entropy production rate Δ'_C reaches a maximum between $T'_S = 1$ (the wall temperature) and $T'_S = 0$ (the saturation temperature) due to opposing dependencies between the mass flux and the difference in phase free entropies on the interface temperature. The temperature corresponding to the maximum Δ_{LV}^s drops towards the saturation value as the distance d between the wall and interface increases to macroscale lengths. The vapor and liquid properties of water (thermal conductivities, latent heat of phase change, etc.) as a function of temperature were referenced from NIST[124]. The boundary conditions and location were set to $L = 0.1$ m, $T_{\text{wall}} = 550$ K, $T_{\text{sat}} = 373.15$ K, $p_P = 1$ atm. Linear temperature profiles are assumed in the liquid and vapor domains.

Here, we propose that the MEPP closes the phase change problem at the two phase interface, in that the maximum entropy production rate can be used to specify the interface temperatures. In general, suppose that the discontinuous temperatures T_{SA}^* , T_{SB}^* , and T_S^* give an optimal solution to $\max(\Delta[T_{SA}, T_{SB}, T_S])$ while satisfying the imposed constraints on thermodynamic fluxes or forces and conservation laws, represented by the series of conditions $F_i[T_{SA}, T_{SB}, T_S]=0$ for $i \in \{1, 2, \dots, N\}$; in general, the dependence of

$\Delta[T_{SA}, T_{SB}, T_S]$ on the interface temperatures is given by eqn. 3.17. Then T_{SA}^* , T_{SB}^* and T_S^* are the temperatures observed at the two phase interface.

One caveat is that the diffusive time scale $\tau_{D,c}$ of each phase must be smaller than the evolutionary time scale $\tau_{E,c}$ of the interface in order for the thermodynamic state satisfying MEPP to be accessible in the nonequilibrium process. Essentially, the effective lifetime of the system $\tau_{E,c}$ over which steady thermodynamic properties can be measured must be greater than the thermal relaxation time $\tau_{D,c}$ for the interface temperatures to be sampled in each phase. This means that the system can be treated as quasi-stationary with respect to the attainment of the interface condition. Here, we take $\tau_{D,c} = d_c^2/\alpha_c$ to be the thermal diffusion time scale such that α_c is the thermal diffusivity of phase $c \in \{A, B\}$ at the associated interface temperature and d_c is the relevant length scale occupied by phase c . The evolutionary time scale $\tau_{E,c} = d_c/u_S$ is the length scale divided by the interface speed u_S , which likewise is a function of the interface temperature. We find that for systems that satisfy $\tau_{D,c} < \tau_{E,c}$, the interface temperatures and phase change rates predicted by MEPP capture the corresponding data obtained from experiments and molecular dynamics simulations.

The physical argument behind this closure condition is that the trajectory of states corresponding to the maximum entropy production rate at each step reflects the most probable path observed in the system under the constraints imposed by fixed thermodynamic fluxes or forces as well as conservation laws [125, 118]. Endres showed that for the Schlögl model of a first order phase transition with noise, the probability of observing a particular trajectory at nonequilibrium steady state increases exponentially with the entropy production rate[129]. Specifically, the most probable trajectory of states is the one

that maximizes the entropy production rate, while minimizing the classical and stochastic action along that path. The latter condition represents that the governing equations constraining the system are satisfied. A stepwise algorithm to apply this condition in calculating the interface temperatures is presented in Methods. It can be used to capture computational and experimental data on the evolution of interfacial properties during phase change processes.

3.4. Results

The interfacial temperatures that maximize the entropy production rate can be used to describe phase change features in both simulation and experiment. Only properties in the far field need to be known a priori in order to predict temperatures and mass fluxes at the interface. The efficacy of the proposed thermodynamic closure principle prompts its use in experiment and continuum simulation to capture the evolution of the interface under nonequilibrium behavior.

3.4.1. Nanoscale simulation of liquid-vapor water

In this work, we use molecular dynamics (MD) simulations to explore nonequilibrium phase change across the liquid-vapor interface of water within nanometers of the superheated wall. The simulation setup in Fig. 4.1 is established across a distance $L + d$ of 30 nm, with phase A adjacent to the superheated wall referring to water vapor and phase B adjacent to the piston denoting liquid water; further MD details are provided in the Methods section below.

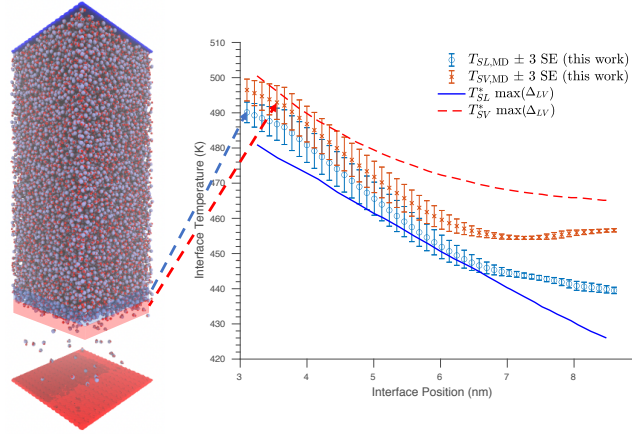


Figure 3.5. The evolution of liquid and vapor side interface temperatures as a function of the interface distance d from the superheated wall, predicted by the maximum entropy rate principle proposed in this work and measured via MD. The temperatures as averaged over 6 molecular dynamics simulations from independent initial conditions are well captured by maximizing the interfacial entropy production rate at each time step. The vapor and liquid properties of water (thermal conductivities, latent heat of phase change, etc.) as a function of temperature were referenced from literature [136, 137, 124]. The boundary conditions were $T_W = 575$ K, $T_P = 350$ K, $p_P = 1$ bar. Linear temperature profiles were assumed in the liquid and vapor domains.

Fig. 3.5 demonstrates that the liquid and vapor side temperatures (T_{SL}^* and T_{SV}^*) associated with the maximum entropy production rate $\Delta_{LV,\max}$ at the two phase interface (eqn. 3.24) well captures the interfacial temperatures $T_{SL,MD}$ and $T_{SV,MD}$ measured using molecular dynamics as the system evolves during the phase change process. The constant saturation temperature $T_{\text{sat}} = 373.15$ K corresponding to the pressure $p_P = 1$ bar applied at the piston completely fails to model the non-constant, discontinuous dynamics of the interface temperatures. This common assumption would appear as a constant line far below the contours show in Fig. 3.5 and be incapable of capturing the rate of phase change.

In the window of time presented in which the vapor film thickness d increases from 3.5 to 9 nm, the two phase interface shifts away from the superheated wall mainly due to expansion of the superheated vapor. In fact, the average mass flux calculated via MD when the interface position $3.5 < d < 9$ nm is $\overline{m} = -414.1 \frac{\text{kg}}{\text{m}^2\text{s}}$, which means that condensation occurs at the interface. The mass flux that maximizes the entropy production rate averaged over $3.5 < d < 9$ nm is $\overline{m}^* = -478.1 \frac{\text{kg}}{\text{m}^2\text{s}}$. Thus, this entropic interface principle accurately describes the physically unintuitive mode of condensation at the interface near a superheated vapor and estimates the correct order of magnitude of the phase change rate of a nonequilibrium, nanoscale process.

Possible sources of error in this analysis include the deviation of fluid properties the SPC/E water model compared to real water. There may also be differences in the definition of material properties in the nanoscale film relative to bulk phase values [164]. Additionally, it was assumed that the temperature profiles in both the liquid and vapor follow linear regimes, which can produce some deviation from the exact interfacial heat fluxes measured by MD (Fig. 3.6). However, this is the lowest order model that does not require additional knowledge of the system aside from the applied boundary conditions. The interface temperatures calculated by maximizing the entropy production rate at the interface while assuming linear profiles are adequate in capturing the values measured by MD.

In this system, as in all MD simulations and experimental outcomes included in this work, the respective thermal diffusion time scales $\tau_{D,c}$ are smaller than the evolutionary time scales of the interface $\tau_{E,c}$. Fig. 3.7 shows that $\tau_{E,L}$ exceeds $\tau_{D,L}$ by 1 order of magnitude in the liquid phase while $\tau_{E,V}$ surpasses $\tau_{D,V}$ by 2 orders of magnitude in

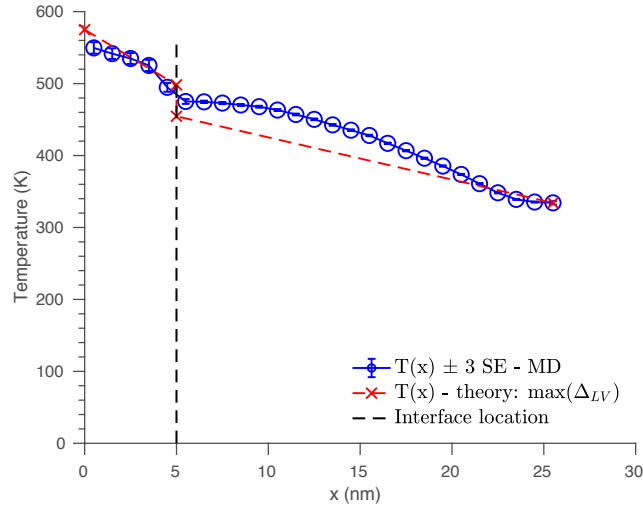


Figure 3.6. The temperature profiles in the vapor and liquid phases were measured using molecular dynamics (MD) for a system being superheated on the vapor side wall to $T = 575$ K and cooled on the liquid side piston to $T = 350$ K. The piston applies a pressure of 1 bar. The assumption of linear temperature profiles incurs error in calculating the heat fluxes for both phases. However, it is the lowest order model that does not require additional knowledge of the system outside of the applied boundary conditions. Additionally, the interface temperatures calculated by maximizing the entropy production rate at the interface while assuming linear profiles are adequate in capturing the values measured by MD. The vapor and liquid properties of water (thermal conductivities, latent heat of phase change, etc.) as a function of temperature were referenced from the IAPWS formulation [136, 137, 124].

the vapor phase. Intuitively, this means that the system has time to resolve interfacial temperatures that maximize the entropy production rate before the interface shifts to a new location, such that the interface can be considered stationary with respect to the entropy production rate. The method of calculation for these time scales is presented in Methods.

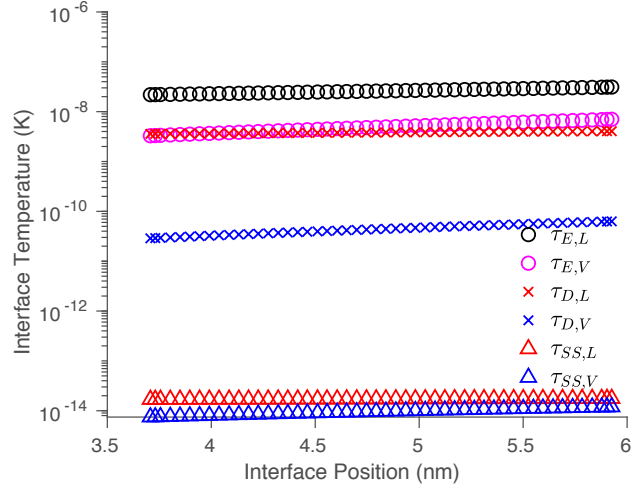


Figure 3.7. The evolutionary time scale of the interface $\tau_{E,c}$ as well as the diffusive time scale $\tau_{D,c}$, $c \in L, V$ of each phases were measured using molecular dynamics (MD) for a system being superheated on the vapor side wall to $T = 575$ K and cooled on the liquid side piston to $T = 350$ K. The piston applies a pressure of 1 bar. The diffusive time scales in both phases are orders of magnitude smaller than evolution time of the interface, such that the system can be considered as quasi-steady relative to the interfacial temperatures. The time scales associated with the speed of sound were also reported to show that both phases were not caught in the ballistic regime. The vapor and liquid properties of water (thermal conductivities, latent heat of phase change, etc.) as a function of temperature were referenced from the IAPWS formulation [136, 137, 124].

3.4.2. Nanoscale simulation of ice-liquid water

The agreement between the proposed entropy production interface principle and molecular dynamics simulation holds for phase change between solid and liquid water as well. Fig. 3.9 shows that the ice and liquid side interface temperatures T_{SI}^* and T_{SL}^* corresponding the maximum interfacial entropy production rate well describe the the highly non-equilibrium interface temperatures measured by MD during the freezing process [131].

Note that the entropy production rate Δ_{IL} at the interface between the ice and liquid phases can be derived from the general 1D expression (eqn. 3.21) by taking the pressure

dependence of the ice phase entropy to be

$$(3.27) \quad (T_S)s_I = (T_S)s_{I,\text{sat}} - \frac{1}{\rho_I} (p_I - p_{\text{sat}}[T_{SI}]).$$

The interfacial entropy production rate Δ_{IL} can then be expressed as

$$(3.28) \quad \Delta_{IL}[T_{SI}, T_{SL}, T_S] = \dot{m} \left(s_{L,\text{sat}} - s_{I,\text{sat}} - \frac{1}{T_{SL}\rho_L} (p_L - p_{\text{sat}}[T_{SL}]) + \frac{1}{T_{SI}\rho_I} (p_I - p_{\text{sat}}[T_{SI}]) \right) \\ + q_L(-1/T_{SL}) - q_I(-1/T_{SI}) - \frac{\dot{m}^3}{2T_S} \left(\frac{1}{\rho_L^2} - \frac{1}{\rho_I^2} \right),$$

where the difference in liquid and ice phase entropies $s_{L,\text{sat}} - s_{I,\text{sat}}$ for the mW water model was given by Holten et al[130].

The interface temperatures measured by MD are approximately continuous ($T_{SI,\text{MD}} \approx T_{SL,\text{MD}} \approx T_{S,\text{MD}} \approx 267$ K), but nonetheless form non-monotonic profiles with the boundary conditions in both the liquid and ice domains $T_{BC} \approx 250$ K. In the ice phase, the temperature rises from the boundary T_{BC} to a peak near the interface before falling in the liquid phase back to T_{BC} . Thus, the simplest assumption of a constant temperature distribution in both phases $T_{S,\text{MD}} \approx T_{BC}$ fails. The freezing point of the mW water model $T_F = 274.6$ K exceeds $T_{S,\text{MD}}$ by around 7 K and is thus also a poor predictor.

The best estimate for the interface temperatures $T_{SL}^* = T_{SI}^* = 263.2$ K is obtained by maximizing the entropy production rate at the ice-liquid interface $\Delta_{IL}[T_{SI}, T_{SL}, T_S = T_{SL}]$ in eqn. 3.28 while assuming linear temperature profiles in both the liquid and vapor domain. The interfacial velocity associated with this maximum entropy rate principle

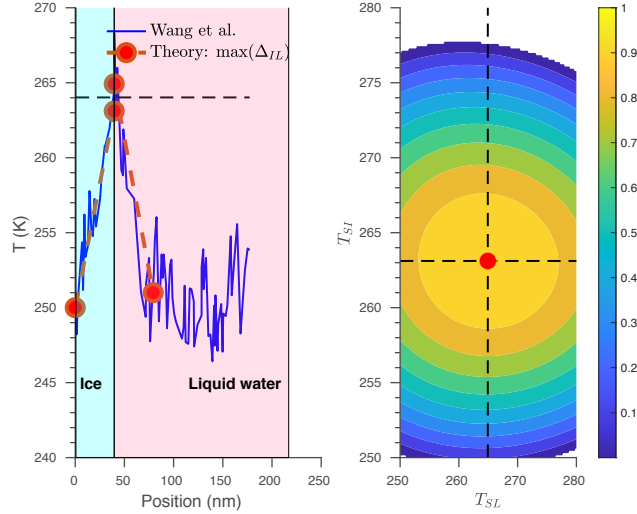


Figure 3.8. **A)** The temperature profile of an ice-liquid system as measured via molecular dynamics by Wang et al[**131**] using the mW water model and as calculated by the maximum entropy production interface condition proposed in this work. The boundary condition in the liquid water has been chosen at a location closer to the interface in order to better estimate the interfacial heat flux. Note that molecular dynamics places the interface temperature $T_{SL,MD} \approx T_{SI,MD} \approx 267$ K to be 15 K greater than the boundary temperatures $T_{BC} \approx 250$ K but around 7 K less than the freezing point of mW water $T_F = 274.6$ K. The temperature distribution is non-monotonic and yet cannot be approximated accurately by the saturation temperature assumption. **B)** The interfacial entropy production rate exhibits a maximum value at $T_{SL}^* = 265.2$ K, $T_{SI}^* = 263.1$ K. The ice and liquid properties of water (thermal conductivities, latent heat of phase change, etc.) were drawn from the mW water properties reported by Wang et al. [**131**]. Linear temperature profiles were assumed in the liquid and ice domains.

$u_S^* = 4.37$ m/s also agrees with the interface velocity measured via molecular dynamics $u_{S,MD} = 4.17$ m/s.

Fig. 3.8 demonstrates that the boundary condition can be selected closer to the interface in order to better estimate the interfacial heat flux. In general, if more information is known about the system, the interfacial entropy production rate as well as the associated temperatures and phase change rate can be determined with greater accuracy.

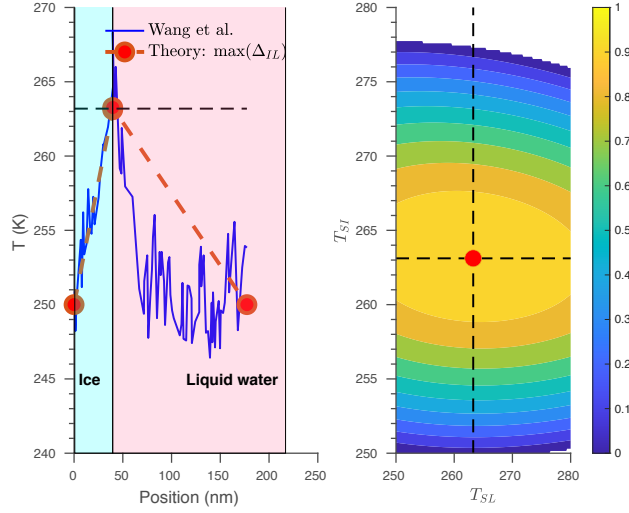


Figure 3.9. **A)** The temperature profile of an ice-liquid system as measured via molecular dynamics by Wang et al.[**131**] using the mW water model and as calculated by the maximum entropy production interface condition proposed in this work. Note that molecular dynamics places the interface temperature $T_{SL,MD} \approx T_{SI,MD} \approx 267$ K to be 15 K greater than the boundary temperatures $T_{BC} \approx 250$ K but around 7 K less than the freezing point of mW water $T_F = 274.6$ K. The temperature distribution is non-monotonic and yet cannot be approximated accurately by the saturation temperature assumption.**B)** The interfacial entropy production rate exhibits a maximum value at $T_{SL}^* = T_{SI}^* = 263.2$ K. The ice and liquid properties of water (thermal conductivities, latent heat of phase change, etc.) were drawn from the mW water properties reported by Wang et al. [**131**]. Linear temperature profiles were assumed in the liquid and ice domains.

In terms of the time scale restrictions, the difference between the evolution time $\tau_{E,I}$ and the diffusion time scale $\tau_{D,I}$ in the ice phase is just over 1 order of magnitude. Meanwhile, $\tau_{E,L} = 1 \times 10^{-8}$ and $\tau_{D,L} = 9 \times 10^{-9}$ are closer but also satisfy $\tau_{E,L} > \tau_{D,L}$. This implies that the system can be considered quasi-static with respect to the achieved interfacial temperatures.

3.4.3. Micron-scale experiments of liquid-vapor water and octane

The stochastic rate theory (SRT) suggested by Ward et al. advanced meticulous experiments to measure the interfacial temperature jump between two phases [132, 116, 133, 134, 135, 113]. As noted, the SRT gives reasonable estimates for the temperature jump if the interface temperature on either the liquid (T_{SL}) or vapor (T_{SV}) side as well as the mass flux across the interface is measured first.

Fig. 3.11 shows that the experimental interface temperatures measured via micro-thermocouples [114] are well captured by the vapor and liquid interface temperatures T_{SV}^* , T_{SL}^* that maximize $\Delta_{LV}[T_{SV}, T_{SL}, T_S = T_{SL}]$ (eqn. 3.24). Therefore in applications where interface properties are not available a priori, the maximum entropy production condition may be used to pinpoint the absolute temperatures of both phases at the interface and the mass flux due to phase change. Only far field boundary conditions for temperature and pressure must be input into this analysis.

As with prior analyses, taking the boundary condition in the vapor phase closer to the interface does not significantly impact the interfacial temperatures T_{SV}^* , T_{SL}^* that maximize Δ_{LV} , as shown in Fig. 3.10. This simply provides a better estimate of the interfacial heat fluxes used to calculate the entropy production rate.

The bulk temperature profiles in Fig. 3.11A are non-monotonic due to the interfacial temperature jump, and the liquid side interface temperature T_{SL} is not bounded by the temperature conditions in the far field. This escapes a straightforward description from existing theory and heretofore falls under the umbrella of 'nonlinear, transient evolution'. However, the nonequilibrium thermodynamic mechanism proposed in this work suggests that the interfacial liquid and vapor temperatures are selected by maximizing the rate

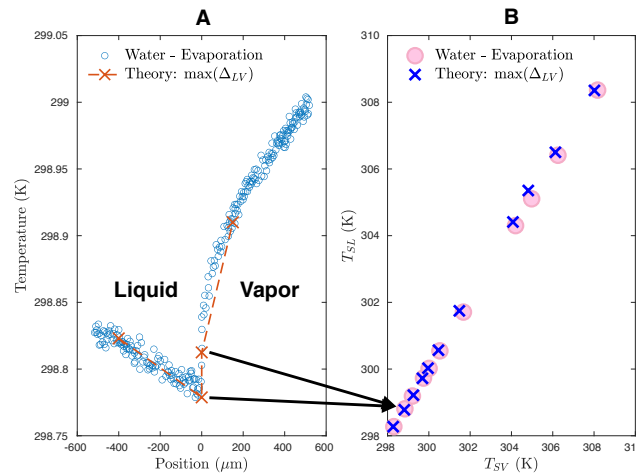


Figure 3.10. **A)** The experimental temperature profile [114] of a two phase water system is well described by the predicted interface temperatures for the liquid (T_{SLM}) and vapor (T_{SVM}) side using the maximum entropy principle. The interface is located at $x = 0$ micron, where a pronounced temperature jump creates a non-monotonic temperature distribution such that T_{SL} is not bounded by the liquid or vapor temperatures in the far field. **B)** The interfacial temperature jump is well described by the maximum entropy principle. Only data sets that provided all necessary information such as boundary conditions, distances to the interface, etc. were included in the plot to avoid using any unknown properties to 'fit' the data. Linear temperature profiles were assumed in the liquid and vapor domains. The vapor and liquid properties of water and octane (thermal conductivities, latent heat of phase change, etc.) as a function of temperature were referenced from the IAPWS formulation [136, 137, 124].

of entropy produced due to phase change; this non-monotonic behavior of the interface temperatures is therefore deterministic, rather than stochastic.

Another set of experimental results [132, 116, 133, 134, 113] are visualized in Fig. 3.12. The temperatures of each phase at the interface in Fig. 3.12A and mass fluxes due to phase change in Fig. 3.12B are well described by the thermodynamic principle proposed in this work. This agreement holds for evaporation and condensation of water under laminar and turbulent conditions, as well as for evaporation of octane. Although temperature

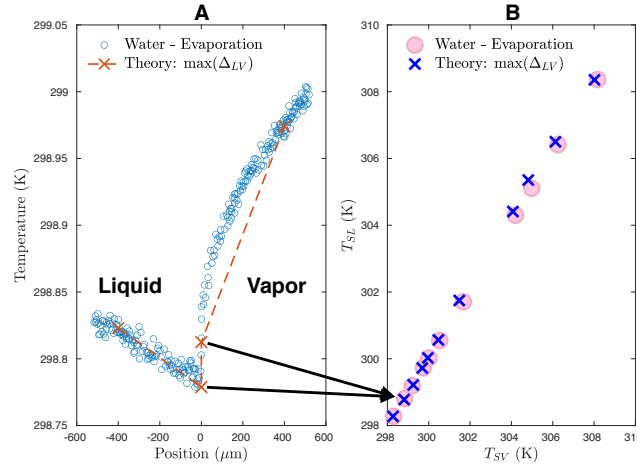


Figure 3.11. **A**) The experimental temperature profile [114] of a two phase water system is well described by the predicted interface temperatures for the liquid (T_{SLM}) and vapor (T_{SVM}) side using the maximum entropy principle. The interface is located at $x = 0$ micron, where a pronounced temperature jump creates a non-monotonic temperature distribution such that T_{SL} is not bounded by the liquid or vapor temperatures in the far field. **B**) The interfacial temperature jump is well described by the maximum entropy principle. Only data sets that provided all necessary information such as boundary conditions, distances to the interface, etc. were included in the plot to avoid using any unknown properties to 'fit' the data. Linear temperature profiles were assumed in the liquid and vapor domains. The vapor and liquid properties of water and octane (thermal conductivities, latent heat of phase change, etc.) as a function of temperature were referenced from the IAPWS formulation [136, 137, 124].

jumps in these sets of experiments are typically smaller, the nonequilibrium phase change processes examined nonetheless exhibit the distinct non-monotonic characteristic wherein the interface temperatures can lie outside the range of the far field temperature conditions. In all cases, only far field pressures, temperatures, and domain lengths were used as input into the maximum entropy rate principle; all properties on the interface were determined by maximizing the entropy production rate Δ_{LV} (eqn. 3.24).

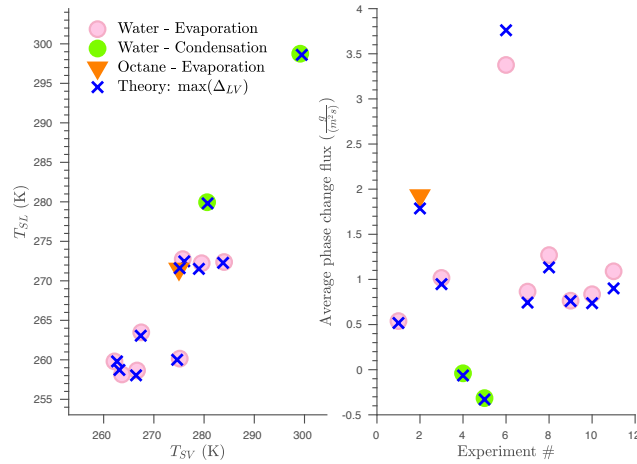


Figure 3.12. **A)** The experimentally measured temperature jump as well as the distinct liquid and vapor side temperatures at the two-phase interface are captured by the maximum entropy principle. This general agreement between experiment and theory holds for evaporation (Exp # 1, 3, 7, 8, 9)[**132**, **116**, **133**] and condensation (Exp # 4, 5)[**116**] of water; evaporation of octane (Exp # 2) [**134**]; evaporation of water under turbulent conditions (Exp # 6) [**135**]; and evaporation of water heated on the vapor side (Exp # 10, 11, 12) [**113**]. **B)** The average phase change rate at the interface in units of mass per area, per unit time drawn from the same experiments are also captured by the maximum entropy principle. Only data sets that provided all necessary information such as boundary conditions, distances to the interface, etc. were included in the plot to avoid using any unknown properties to 'fit' the data; data points that overlapped significantly in the plot were also excluded for clear visualization. The vapor and liquid properties of water and octane (thermal conductivities, latent heat of phase change, etc.) as a function of temperature were referenced from the IAPWS formulation [**136**, **137**, **124**].

3.5. Discussion

To gain a physical understanding of nonequilibrium phase change in a liquid-vapor system, we observe the interfacial temperature jump, mass flux and entropy production rate associated with the average pressure and temperature at the interface for water (Fig. 3.15). In this example, the widths of both the vapor and liquid domains are fixed at 1

mm. The piston cooling the liquid reservoir is held at a constant temperature of 350 K, while the wall temperature is varied from $274 \text{ K} \leq T_W \leq 646 \text{ K}$ for each value of pressure $10^{2.9} \text{ Pa} \leq p \leq 10^6 \text{ Pa}$ imposed on the system (Fig. 3.15D). Given each set of boundary conditions, the maximum value of the entropy production rate $\Delta_{LV,\max}$ in Fig. 3.2A is used to determine the interface temperatures T_{SL}^* and T_{SV}^* , whose average is plotted on the x axis. Similarly, the average pressure at the two phase interface is tabulated on the y axis.

Fig. 3.15A overlays the interfacial temperature jump $\Delta T_S = T_{SV}^* - T_{SL}^*$ on the average pressure-temperature diagram at the interface. It is notable that interfacial temperature continuity is a special condition confined to a single contour, whereas the majority of the phase space is dominated by the existence of a temperature discontinuity. The sign of this jump, whether $T_{SV}^* > T_{SL}^*$ or vice versa, cannot in general be predicted by the equilibrium binodal curve. The assumption of temperature continuity is not generally reliable when the local interface rests in equilibrium.

Another way to characterize the interface is to look at the mass flux due to phase change (Fig. 3.15B). The contour along which no phase change occurs is likewise ill predicted by the binodal in general. The two contours $\dot{m} = 0$ and $\Delta T_S = 0$ separate the interfacial phase space into four regions. In the top left and bottom right sectors, phase change conforms to our physical intuition around the binodal. That is, as temperature increases or pressure decreases past the coexistence curve, vapor becomes the bulk stable phase and vice versa. The top right and bottom left sectors characterize the metastable phases that are involved in processes like capillary condensation below and

capillary evaporation above the binodal. Thus this entropic interface condition gives a complete description of possible phase change processes in nonequilibrium scenarios.

All three curves (binodal, $\dot{m} = 0$, and $\Delta T_S = 0$) only intersect at the point $T_W = T_{SV}^* = T_{SL}^* = T_P$, which reflects constant temperature profiles in both phases. This corresponds to the bulk system being in equilibrium (Fig. 3.15C) such that $\Delta_{LV,\max}$ reaches a global minimum value. The maximum entropy production rate for each set of boundary conditions can be decomposed into the phase entropy $\Delta_{1,\max}$, kinetic energy $\Delta_{2,\max}$, and heat flux $\Delta_{3,\max}$ terms on the pressure-temperature phase diagram (Fig. 3.13). As the average interface temperature increases or the pressure decreases, $\Delta_{1,\max}$ grows monotonically while $\Delta_{3,\max}$ exhibits the opposite behavior. The kinetic term $\Delta_{2,\max}$ remains negligible due to the mass flux \dot{m} relative to the other quantities. Thus, the competition of the two terms $\Delta_{1,\max}$ and $\Delta_{3,\max}$ gives rise to a global minimum in the maximum entropy production rate when the system rests in equilibrium.

Fig. 3.14 shows that the maximum entropy production rate for octane displays characteristics analogous to that of water. The competing relationships between the interface temperatures and the individual terms $\Delta_{1,\max}$ and $\Delta_{3,\max}$ hold similarly for octane, while the kinetic contribution from $\Delta_{2,\max}$ can likewise be neglected. As a result, octane also achieves a global minimum value of $\Delta_{LV,\max}$ at the intersection of the binodal, zero mass flux, and temperature continuity contours.

Both of these interfacial phase diagrams agree with the minimum entropy production rate principle [138]. This principle says that over the relaxation time scale of a stationary nonequilibrium system with some thermodynamic forces fixed and others free, the thermodynamic fluxes in the system conjugate to those unfixed forces will disappear. This

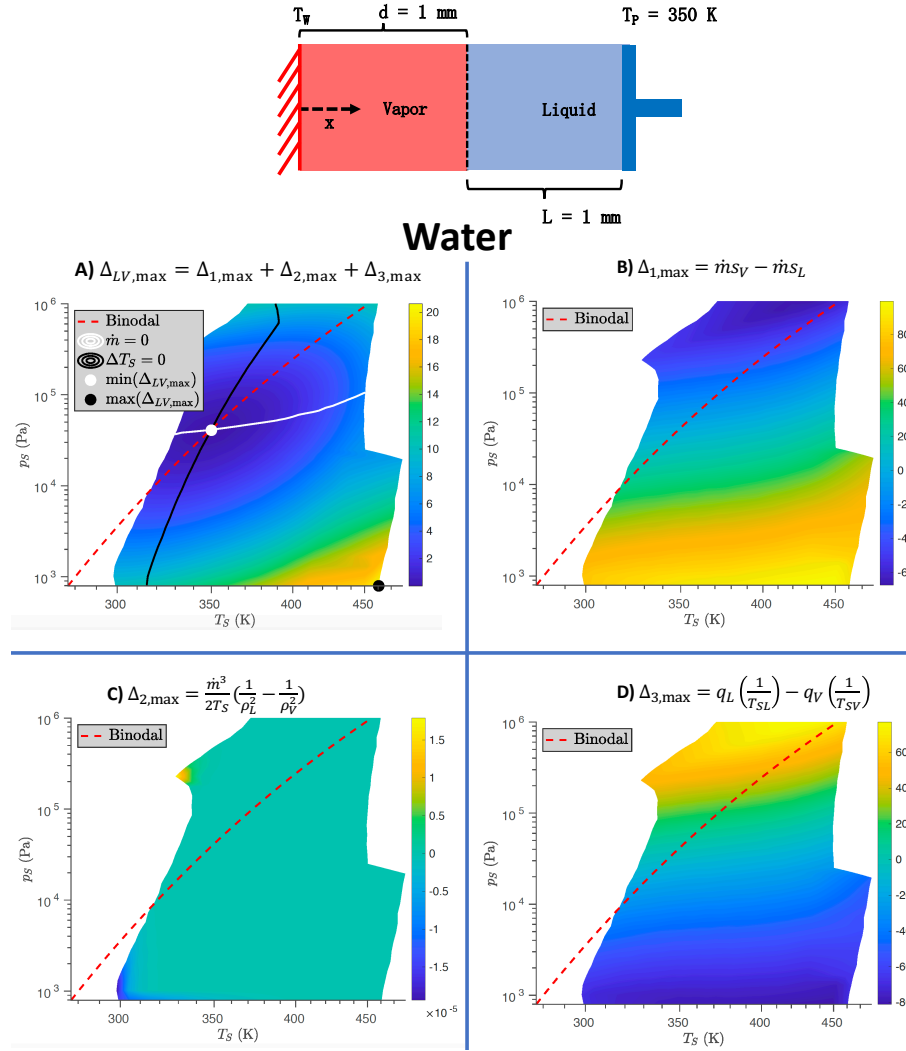


Figure 3.13. The components of the maximum entropy production rate at the two phase interface are mapped onto the average interfacial pressure and temperature. The width of the vapor and liquid domains are both 1 mm. The piston cooling the liquid reservoir is held at a constant temperature of 350 K, while the wall temperature and piston pressure are varied. **A)** The maximum entropy production rate Δ_{LV} (eqn. 3.24) at the average interface temperature $(T_{SV}^* + T_{SL}^*)/2$ exhibits a global minimum at the intersection of the binodal, continuous interface temperature and zero mass flux curves. **B)** The term Δ_1 , which encapsulates the difference in phase entropies, increases for larger average interface temperature and lower interface pressure. **C)** The second component of the entropy production rate Δ_2 reflects the kinetic energy contribution. Due to the small mass flux \dot{m} relative to the other quantities, this term is negligible. **D)** The third component of the entropy production rate Δ_3 is due to heat transfer from the interface. This term increases for lower interface temperature and higher pressure. The vapor and liquid properties of water (thermal conductivities, latent heat of phase change, etc.) as a function of temperature were referenced from the IAPWS formulation [136, 137, 124].

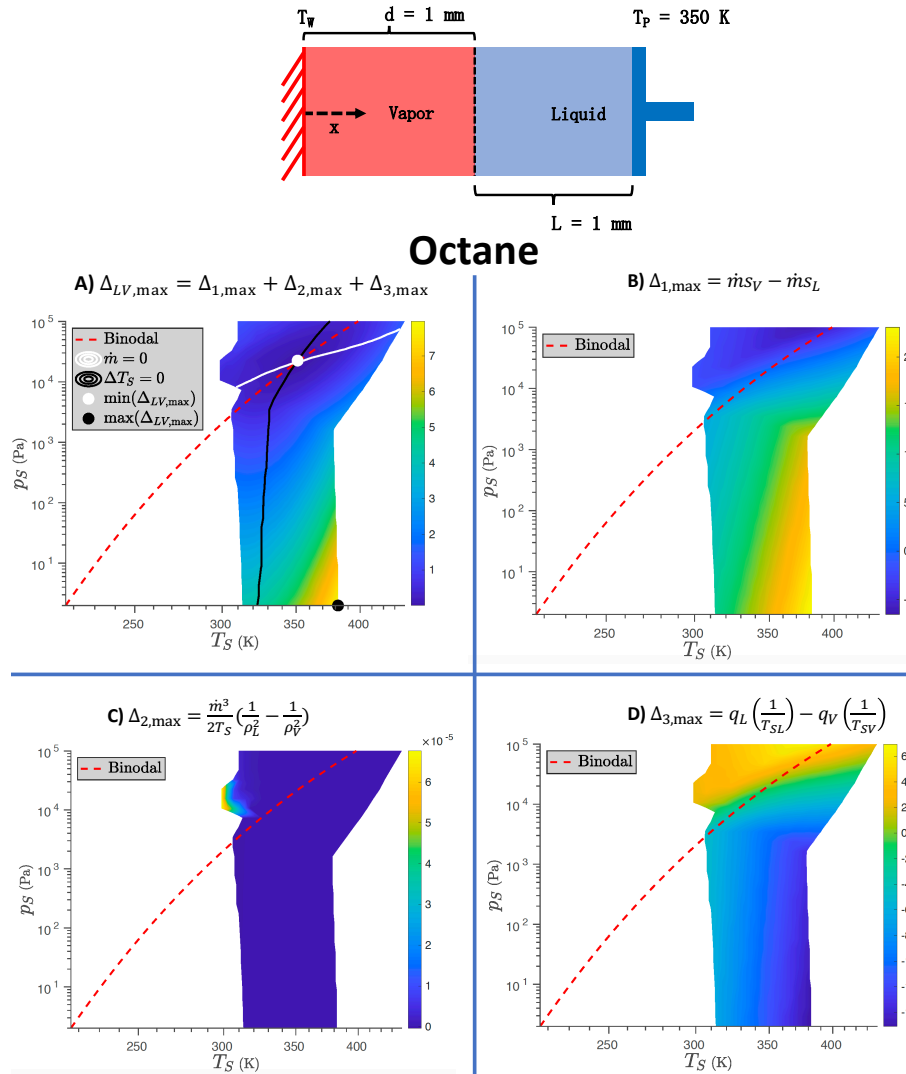


Figure 3.14. For octane, the components of the maximum entropy production rate at the two phase interface are mapped onto the average interfacial pressure and temperature. The width of the vapor and liquid domains are both 1 mm. The piston cooling the liquid reservoir is held at a constant temperature of 350 K, while the wall temperature and piston pressure are varied. **A)** The maximum entropy production rate $\Delta_{LV,max}$ (eqn. 3.24) at the average interface temperature $(T_{SV}^* + T_{SL}^*)/2$ exhibits a global minimum at the intersection of the binodal, continuous interface temperature and zero mass flux curves. **B)** The term $\Delta_{1,max}$, which encapsulates the difference in phase entropies, increases for larger average interface temperature and lower interface pressure. **C)** The second component of the entropy production rate $\Delta_{2,max}$ reflects the kinetic energy contribution. Due to the small mass flux \dot{m} relative to the other quantities, this term is negligible. **D)** The third component of the entropy production rate $\Delta_{3,max}$ is due to heat transfer from the interface. This term increases for lower interface temperature and higher pressure. The vapor and liquid properties of water (thermal conductivities, latent heat of phase change, etc.) as a function of temperature were referenced from the literature [124, 142, 143].

drives the system toward the minimum of the entropy production rate, which occurs at equilibrium. Indeed, the global minimum in the entropy production rate is associated with the equilibrium interfacial temperature and pressure, at the intersection of the two contours $\dot{m} = 0$ and $\Delta T_S = 0$. If the wall temperature is allowed to evolve over time from the initial condition (unfixed) rather than be held to a constant value, the system would eventually relax to this equilibrium state in which the temperature profiles in both phases are constant and equal.

On the shorter time scale, or if all thermodynamic forces are held constant, the associated thermodynamic fluxes adjust in order for the system to achieve the maximum entropy production rate for each specific, average interfacial pressure and temperature plotted in Fig. 3.15C. The minimum entropy production rate principle suggests that a stationary nonequilibrium system with sufficient degrees of freedom will tend toward minimum value of the entropy production rate over the relaxation time scale, whereas the maximum entropy production rate principle tells us that a nonequilibrium system on a shorter time period or under constant thermodynamic forcing will find the state corresponding to the maximum in the entropy production rate as the fluxes vary. Indeed, both principles can apply simultaneously, in that a stationary nonequilibrium system may approach the state associated with the minimum entropy production rate on a longer time scale by taking individual steps over a short time scale that maximize the entropy production rate at each step, while satisfying thermodynamic constraints and governing laws.

Thus, the maximum entropy production rate allows us to accurately pinpoint the interfacial properties of a nonequilibrium system undergoing phase change in a thermodynamically consistent manner. It is the missing condition needed to close the two phase

problem when phase change occurs across the interface. In addition, the minimum entropy production rate informs the trajectory of a stationary phase change system over longer time scales, within the permissible phase space set by the presence of fixed thermodynamic forces or fluxes.

3.6. Conclusion

The maximum entropy production rate at the interface closes the phase change problem by determining the interface temperature and velocity. The predictions from the proposed entropic interface condition well capture nanoscale temperatures and mass fluxes for liquid, vapor and solid phase change at the nanoscale. The condition also accurately predicts experimental data on interface temperature jumps and mass fluxes for different fluids under both turbulent and laminar flows at mesoscale. This agreement suggests that at most length and time scales, the interface properties are dominated by a deterministic thermodynamic principle (that of entropy production maximization) rather than stochastic or transient behavior which must be modeled probabilistically.

The maximum entropy principle can be used directly to design phase change systems to achieve desired mass fluxes or interface properties for the applications discussed prior. It can also be used to model nanoscale and mesoscale effects in continuum level simulations of multiphase flows, where the saturation temperature has been the standard approximation.

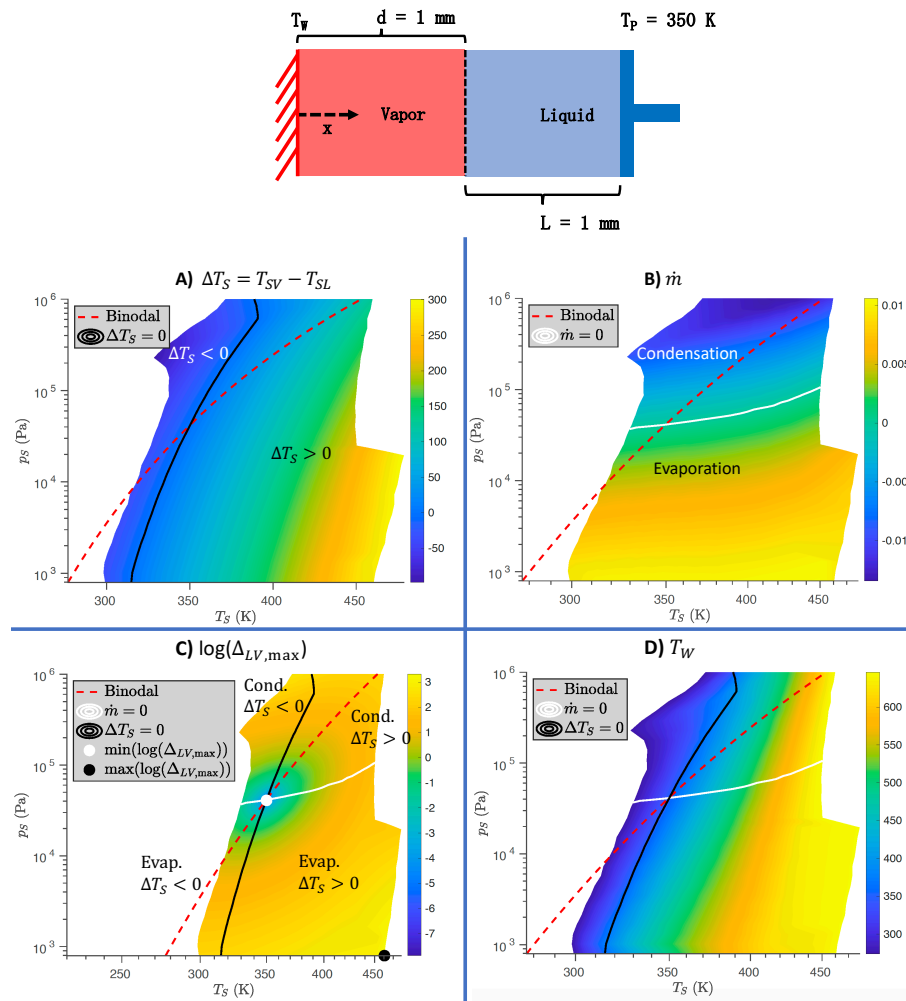


Figure 3.15. The nonequilibrium properties at the two phase interface are mapped onto the average interfacial pressure and temperature. The distance of the interface from the wall d and the distance of the interface to the piston L are both 1 mm, corresponding to the widths of the vapor and liquid domains. The piston cooling the liquid reservoir is held at a constant temperature of 350 K, while the wall temperature and applied piston pressure are both varied. **A)** The temperature jump at the liquid vapor interface is generally nonzero. The interface temperature is only continuous along the black contour. **B)** The mass flux due to phase change across the interface is positive for evaporation and negative for condensation. No phase change occurs along the white contour. **C)** The logarithm of the maximum entropy production rate at each interface pressure and temperature shows that the global minimum is located at equilibrium on the binodal, where the continuous interface temperature and zero mass flux contours intersect. The point of intersection corresponds to a constant temperature profile equal to the far field piston temperature 350 K in the liquid domain. **D)** The wall temperature T_w is varied from 274 K to 646 K at different pressures to obtain the phase diagrams of the interfacial temperature jump, mass flux and entropy production rate. The vapor and liquid properties of water (thermal conductivities, latent heat of phase change, etc.) as a function of temperature were referenced from the IAPWS formulation [136, 137, 124].

3.7. Methods

3.7.1. Finding the interfacial temperature

To use the maximum entropy production rate in determining the interfacial temperatures, we developed the following algorithm.

1.) Obtain the temperature and pressure dependent properties of phases A and B from literature [124, 137], including their entropies $s_{A,B}(T, P)$, thermal conductivities $k_{A,B}(T, P)$, heat capacities, $c_{P-A,B}(T, P)$ and densities $\rho_{A,B}(T, P)$.

2.) Estimate the interfacial heat fluxes. This can be done by assuming a lowest order, linear model for the temperature profiles in each phase. Determine the far field boundary conditions and associated length scales. For instance in a pool boiling scenario for water, the wall temperature T_W , distance d from the wall to the interface, liquid temperature T_P , and distance L between the interface and the liquid held at T_P are natural choices. A pressure condition is also required in either of the two phases. Such boundary conditions can be measured experimentally or set computationally.

If temperature profiles are known a priori, the relevant distributions can be used to precisely determine the interfacial heat fluxes. If flux boundaries instead of Dirichlet conditions are set, the heat fluxes may also be estimated accordingly, though we have not quantified the accuracy of this approach.

3.) For solid or liquid phases, the phase entropies $s_{A,B}$ can be determined using

the temperature and pressure relations given in eqns. 3.23 and 3.27. If a vapor phase can be approximated as an ideal, monatomic gas, eqn. 3.22 offers a suitable relationship for the phase entropy.

4.) In the most general case, determine the entropy production rate Δ as a function of the all possible interface temperatures T_{SA} , T_{SB} , T_S using eqn. 3.17 outlined by Delhaye [120]. We have found that the 1D, massless interface assumptions leading to Δ_{1D} (eqn. 3.21) may provide an adequate estimate in many scenarios. Note that the fluid properties in each phase should be taken at the temperatures and pressures of the interface, meaning that Δ is in general a highly nonlinear function of T_{SA} , T_{SB} , and T_S .

5.) The diffusive time scale $\tau_{D,c}$, $c \in \{A, B\}$ and evolution time scale $\tau_{E,c}$ can be calculated in each phase. Note that $\tau_{D,c} = d_c^2/\alpha_c$ represents the thermal diffusion time scale, such that α_c is the thermal diffusivity and d_c is the relevant length scale occupied by phase $c \in \{A, B\}$. The evolutionary time scale $\tau_{E,c} = d_c/u_S$ is the appropriate length scale in each phase divided by the interface speed u_S . Other than the fixed length scales denoting the present location of the interface, all of the fluid properties in each phase should be evaluated at the appropriate interface temperature.

If $\tau_{E,c} < \tau_{D,c}$, the corresponding interface temperatures are inadmissible; a thermodynamic state cannot be accessed if the thermal relaxation time of either phase exceeds the evolutionary time scale of the interface. The system has “moved on” before the interface temperatures are achieved.

6.) The interface temperatures that maximize the entropy production rate reflect the most probable state observed over sufficient time or multiple iterations- the ensemble average value at the interface.

3.7.2. Molecular dynamics

To gauge interface properties under nanoscale evaporation conditions as set up in Fig. 4.1, we carried out molecular dynamics simulations with LAMMPS [139] software. A total of 32085 SPC/E molecules of liquid water were equilibrated at saturation temperature $T = 373.15$ K in the canonical ensemble with constant pressure (1 atm) imposed by a piston constrained to move only in the direction orthogonal to the bottom surface [164]. The solid surface and piston were constructed using two graphene sheets with armchair lattice orientation, and the interaction between these planes and the SPC/E water molecules was governed by the 6-12 Lennard Jones pair potential with the depth of the potential well fixed at 0.05 kcal/mole [140]. After this equilibration step, the liquid water adjacent to the bottom surface was heated to a target temperature of $T = 575$ K, whereas the liquid adjacent to the piston was held at constant, saturation temperature to simulate nonequilibrium heat transfer conditions [141]. The lateral simulation box size in the plane parallel to the surface and piston was 8 nm by 8 nm. The perpendicular dimension varied as the vapor film thickness evolved in time.

3.8. Author contributions

N.A.P. and T.Y.Z. conceived and planned the research, performed the analyses, and wrote the manuscript.

CHAPTER 4

Cardiovascular disease

Background: What is the physical mechanism that drives aneurysm formation and growth? The question remains fundamentally unresolved. Currently, the clinical diagnosis and treatment of aneurysms is informed by statistical guidelines on the size and growth rate of an aneurysm, along with a holistic consideration of possible symptoms and associated pathologies such as Marfan Syndrome, bicuspid aortic valve, etc. Without knowing the key factors driving aneurysm development, it is difficult to assign meaningful preventative treatment or assess the risk of rupture against the hazards of elective surgical repair. This holds true especially for aneurysms that do not currently satisfy the prevailing surgical intervention guidelines, but nonetheless may experience significant growth or imminent rupture; conversely, aneurysms that exceed an intervention criterion may potentially be stable.

Hypothesis: In this work, we propose a fluid-structure instability that can cause blood vessels to dilate and form aneurysms, or drive existing aneurysms to experience growth. This ab-initio framework leads to a physical parameter that informs the stability of a local vessel cross section. A local dilation that whose parameter exceeds an analytically derived threshold implies that the driving pressure gradient in the blood flow exceeds the restoring effect of the vessel stiffness and blood viscosity; this location is expected to see aneurysm formation or growth.

Methods and Results. A HIPAA-compliant, retrospective study was conducted with 44 patients. The cohort was comprised of patients with magnetic resonance imaging (MRI) scans of the upper and descending aorta. The patient must also have a subsequent follow-up at least one year after the initial MRI scan, where their aneurysm development was reviewed through either MRI, computed tomography (CT) or echocardiogram. The stability parameter was calculated for each aortic cross section for every patient for the earliest MRI data. Patients whose largest parameter value exceeded the analytical threshold was categorized as 'growth expected' (GE) with respect to the proposed instability mechanism. Patients whose largest parameter value did not exceed the threshold was categorized as 'growth not expected', (GNE). This theoretical quantifier was compared with the clinical outcome recorded at follow-up, where patients were categorized as experiencing 'no arteriopathy development' or 'arteriopathy development', which comprises observed aortic diameter growth, surgical intervention, and/or stenosis. A receiving operator characteristic (ROC) curve was generated to gauge the diagnostic capability of the stability parameter. The area under the curve of the ROC analysis was 0.93. No training data was necessary to 'tune' the stability parameter.

Conclusions: The proposed instability mechanism appears to be an important factor in aneurysm growth and formation in many clinical scenarios. It offers accurate prediction of aneurysm development from patient specific data that can inform precise, targeted management of disease progression.

4.1. Introduction

Aneurysms are pathological, localized dilations of a blood vessel that may occur throughout the human body.

Intracranial, thoracic aortic, and abdominal aortic aneurysms (IA, TAA, AAA) are each estimated to occur with a global prevalence of 2 – 5% [144, 145, 146]. Rupture of an aneurysm induces a high rate of mortality and morbidity for the patient. Studies showed that over half of patients with ruptured TAAs or AAAs died before reaching a hospital, with overall mortality ranging from 80 to 100% [147, 148].

For IAs, between 10 to 30% of patients died suddenly away from hospitals [146], and of those admitted for treatment, 45% of patients experienced an outcome categorized as either moderately disabled, severely disabled, vegetative survival, or death on the Glasgow Outcome Disability Scale. Elective surgery can be performed to prevent rupture but also carries the risk of death and complications like paraplegia [147]. Thus, it is vital to accurately determine the risk of aneurysm formation and growth to inform timely treatment.

The standard of care is to recommend elective treatment for aneurysms based on statistical associations between rupture risk and aneurysm size; for TAAs, the chance of rupture increases from 2% for diameters between 4 and 4.9 cm to 7% for diameters above 6 cm, [149] while mean growth rates are between 0.1 to 0.3 cm per year [150]. This informs the current clinical practice, which suggests surgical intervention for aneurysms with diameters larger than a range between 5.5 to 6.0 cm or exhibiting growth rate larger than a range between 0.5 to 1 cm per year, depending on the aneurysm location and patient history [150, 151].

The state of the art to predict aneurysm growth is based on regression analyses for risk factors such as age or smoking history [152]; regression on geometric features such as aneurysm diameter or undulation index [153]; machine learning approaches trained on imaging features such as aneurysm diameter or intraluminal thrombi thickness [154]. These methods are based on establishing a correlation between available clinical data and aneurysm growth rates. As with all regression techniques, the breadth of data used to train the model is the main determinant for performance; with a small training cohort relative to the disease population, the predictive capability of the model becomes extrapolative rather than interpolative.

In this work, we identify a fluid-structure instability that can drive aneurysm formation and growth. The dominant destabilizing terms are the pressure gradient driving blood flow through the blood vessel and the vessel diameter. Meanwhile, the kinematic viscosity of blood and the wall stiffness stabilize the vessel. The competition between these factors reveal an underlying mechanism for aneurysm development as a function of flow and tissue properties. A single dimensionless parameter can be derived from first principles to encapsulate this instability. If the stability parameter at a local cross section of the blood vessel exceeds an analytically derived threshold, an aneurysm is expected to form or grow at the site. Otherwise, the location should remain stable with time.

In a retrospective study of 44 patients with thoracic aortic aneurysms, we show that the stability parameter can be used as a diagnostic biomarker to determine whether an aneurysm grows or stays stable. The only input to calculate the parameter for each patient is a magnetic resonance imaging (MRI) scan taken at a single time point. This analytical determination is then compared with the clinical outcome reported from a

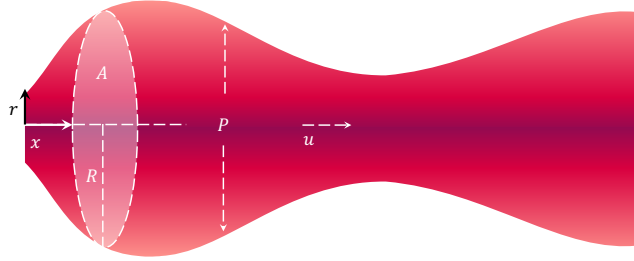


Figure 4.1. The distensible blood vessel is modeled as a one-dimensional system with internal pressure P and velocity u averaged across the radial direction r , which is normal to the centerline coordinate x . The interior area $A = \pi R^2$ varies as a function of both space x and time t .

follow-up at least one year after the baseline MRI. The area under the curve for a receiver operating characteristic analysis is 0.93. No training data is necessary to tune the physical parameter.

4.2. Vessel Instability

A classical model for flow through a blood vessel consists of 1D conservation equations for mass and momentum derived from the Navier-Stokes equations, closed by a constitutive tube law for the variation of pressure with the cross sectional area of the vessel [155, 156]. Here, the pressure gradient is chosen to vary periodically in time with frequency equal to that of the heartbeat cycle, to account explicitly for nonconstant temporal effects[157].

4.2.1. Governing Equations

In 1D, the mass and momentum conservation equations are [155, 156]

$$(4.1) \quad \frac{\partial A}{\partial t} + \frac{\partial(uA)}{\partial x} = 0,$$

$$(4.2) \quad A \frac{\partial u}{\partial t} + \alpha A u \frac{\partial u}{\partial x} = -A \frac{\partial P}{\partial x} + 2\pi\nu \left(r \frac{\partial u}{\partial r} \right)_{r=R},$$

where $A(x, t)$ and $R(x, t)$ denote the cross sectional area and radius, while the pressure $P(x, t)$ and velocity $u(x, t)$ represent values averaged over the radial profiles at each location x and time t . Here, P represents the excess internal pressure over reference pressure outside the vessel, normalized by the fluid density. The kinematic viscosity of blood is ν and its density is ρ .

The viscous term in the momentum equation depends on the radial velocity profile and thus the Womersley number w_o of the flow [155]. It is commonly reformulated as

$$(4.3) \quad 2\pi\nu \left(r \frac{\partial u}{\partial r} \right)_{r=R} = - \underbrace{\left(\frac{2R\tau}{\mu u} \right)}_{\beta} \pi\nu u,$$

where u denote the average fluid velocity, and μ is the dynamic viscosity. The constant β is defined as the flow's shear stress at a nonzero Womersley number $w_0 = R\sqrt{\omega/\nu}$. Here, ω is the angular frequency of the sinusoidal oscillations in time for the velocity u inside the vessel. This factor β therefore captures the relationship between viscous shear stress and the pulsatile flow frequency of the heartbeat cycle. It is determined by using the functional relationships of the wall shear stress $\tau_w = -\mu \left(\frac{u}{r} \right)_{r=R}$ and flow rate Q with w_o [158].

For a parabolic velocity profile corresponding to $w_o = 0$, $\beta = 8$. As w_o increases, the viscous contribution becomes localized in a boundary layer at the wall, leading to a larger value of β for higher frequency flow through the aorta. Figure 4.2 presents β normalized by $\beta = 8$ for a parabolic velocity profile as w_o varies. The initial nonlinear behavior for

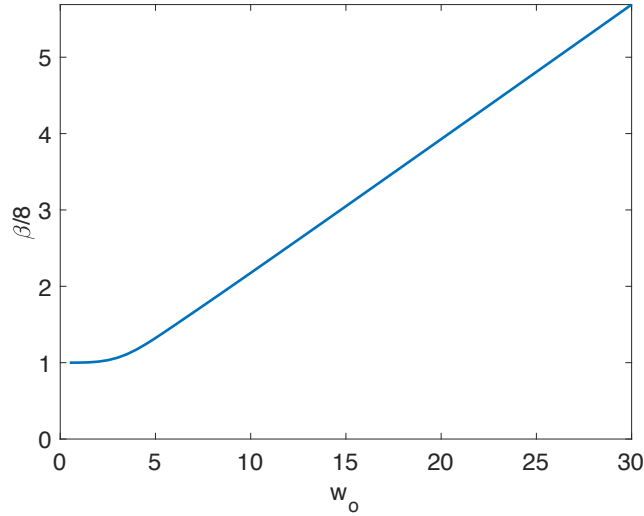


Figure 4.2. The viscous factor β as a function of Womersley number w_o . Here, β has been normalized by its value at $w_o=0$, corresponding to a parabolic velocity profile.

$w_o < 2$ smooths out into a linear relation when $w_o > 2$ and the transient inertial forces are large. This relationship spans the full range of physiological heartbeat frequencies.

For simplicity, the tube law relating pressure to area is taken to be linear

$$(4.4) \quad P = \frac{K_e}{\rho} \left(\frac{A}{A_o} - 1 \right).$$

where K_e is the vessel wall stiffness and A_o is the relaxed area of the vessel corresponding to excess internal pressure $P = 0$.

4.2.2. Base Flow

For pulsatile blood flow, the base, equilibrium solutions for area, pressure, and velocity can be written as the sum of a constant, mean value, and an oscillatory, time-dependent

component

$$(4.5) \quad A_b = A_m + A_\omega(t),$$

$$(4.6) \quad u_b = u_m + u_\omega(t),$$

$$(4.7) \quad -\frac{\partial P_b}{\partial x} = \phi_b = \phi_m + \phi_\omega(t),$$

where A_m , u_m , and ϕ_m are the mean values of area, velocity, and pressure gradient, while A_ω , u_ω , and ϕ_ω are the time dependent, oscillatory components. The oscillatory component of the pressure gradient in the base solution has a real, known amplitude of $\bar{\phi}_\omega$, such that $\phi_\omega(t) = \frac{\bar{\phi}_\omega}{2}(e^{i\omega t} + e^{-i\omega t})$. The base solution for P is obtained by integrating $\frac{\partial P_b}{\partial x}$ with respect to x to give

$$(4.8) \quad P_b = P_m - \left[\phi_m + \frac{\bar{\phi}_\omega}{2}(e^{i\omega t} + e^{-i\omega t}) \right] x$$

If the pressure gradient is sufficiently small with respect to P_m , the term in square brackets can be neglected in the base case for simplicity. This gives a constant pressure profile $P_b \approx P_m$ and thus a constant area profile $A_b \approx A_m$ from the tube law (eqn. 4.4).

The maximum error in assuming constant pressure and area in the base solution can be estimated by $[\phi_m + \bar{\phi}_\omega \cos(\omega t)]x_{max}$, where x_{max} is the length of the ascending aorta. The systolic pressure drop from the ascending to the descending aorta is found on average to be 20 mmHg [166]. With a typical average pressure of $P_m = 100$ mmHg[160], the error in this assumption is approximately 20%.

The oscillatory component of velocity in the base solution takes the form $u_\omega(t) = \frac{1}{2}(\bar{u}_\omega e^{i\omega t} + \bar{u}_\omega^* e^{-i\omega t})$. The base flow is therefore described by the conservation equations

$$(4.9) \quad \frac{\partial u_b}{\partial x} = 0,$$

$$(4.10) \quad A_b \frac{\partial u_b}{\partial t} = -A_b \frac{\partial P_b}{\partial x} - \beta_b \pi \nu u_b,$$

where β_b is the viscous coefficient in the base case. Expanding the momentum equation in terms of the mean and oscillatory terms,

$$(4.11) \quad A_m \frac{\partial u_\omega(t)}{\partial t} = A_m [\phi_m + \phi_\omega(t)] - \beta_b \pi \nu u_m - \beta_b \pi \nu u_\omega(t).$$

Satisfying the momentum equation (eqn. 4.11) for the mean terms ϕ_m and u_m yields

$$(4.12) \quad u_m = \frac{\phi_m A_m}{\beta_b \pi \nu}.$$

Analogously, the magnitude of the oscillatory components are related by

$$(4.13) \quad \bar{u}_\omega = \frac{\bar{\phi}_\omega A_m (\beta_b \pi \nu - i\omega A_m)}{(\beta_b \pi \nu)^2 + (\omega A_m)^2}.$$

Lastly, the tube law gives an expression for the mean pressure

$$(4.14) \quad P_m = \frac{K_e}{\rho} \left(\frac{A_m}{A_o} - 1 \right).$$

4.2.3. Linear stability analysis

The base solutions for the velocity, area and pressure are perturbed by infinitesimal primed quantities

$$(4.15) \quad C = C_b + C'$$

where

$$(4.16) \quad C' = \frac{1}{2} \left(C'_k(t) e^{ikx} + C'^*_k(t) e^{-ikx} \right)$$

for $C \in [A, u, P]$. To conduct a linear stability analysis, the linearized perturbation equations must only contain real terms. First, the time dependent amplitude $C'_k(t)$ associated with each wavenumber k and its conjugate $C'^*_k(t)$ are treated separately to obtain six linearized equations

$$(4.17) \quad \frac{\partial A'_k}{\partial t} + A_b i k u'_k + u_b i k A'_k = 0,$$

$$(4.18) \quad \frac{\partial A'^*_k}{\partial t} + A_b i k u'^*_k + u_b i k A'^*_k = 0,$$

$$(4.19) \quad A_b \frac{\partial u'_k}{\partial t} + A'_k \frac{\partial u_b}{\partial t} + A_b u_b i k u'_k = -A_b i k P'_k - \beta_p \pi \nu u'_k + \phi_b A'_k,$$

$$(4.20) \quad A_b \frac{\partial u'^*_k}{\partial t} + A'^*_k \frac{\partial u_b}{\partial t} - A_b u_b i k u'^*_k = A_b i k P'^*_k - \beta_p \pi \nu u'^*_k + \phi_b A'^*_k,$$

$$(4.21) \quad P'_k = \frac{K_e}{\rho} \frac{A'_k}{A_o},$$

$$(4.22) \quad P'_k{}^* = \frac{K_e}{\rho} \frac{A'_k{}^*}{A_o},$$

where $\phi_b = -\frac{\partial P_b}{\partial x} = \phi_m + \phi_\omega(t)$ is the acceleration due to the pressure gradient in the base solution, and β_p is the viscous coefficient in the perturbed solution. Note that the perturbations are small with respect to the base flow, such that the velocity profile can be approximated as parabolic. Hence, $\beta_p \approx 8$.

Next, each pair of linearized conservation equations (eg. eqn. 4.17 and 4.18) can be added and subtracted to reformulate the perturbation equations in the real C'_r and imaginary components C'_i

$$(4.23) \quad \frac{\partial A'_r}{\partial t} - A_b k u'_i - u_b k A'_i = 0,$$

$$(4.24) \quad \frac{\partial A'_i}{\partial t} + A_b k u'_r + u_b k A'_r = 0,$$

$$(4.25) \quad A_b \frac{\partial u'_r}{\partial t} + A'_r \frac{\partial u_b}{\partial t} - A_b u_b k u'_i = A_b k P'_i - \beta_p \pi \nu u'_r + \phi_b A'_r,$$

$$(4.26) \quad A_b \frac{\partial u'_i}{\partial t} + A'_i \frac{\partial u_b}{\partial t} + A_b u_b k u'_r = -A_b k P'_r - \beta_p \pi \nu u'_i + \phi_b A'_i,$$

$$(4.27) \quad P'_r = \frac{K_e}{\rho} \frac{A'_r}{A_o},$$

$$(4.28) \quad P'_i = \frac{K_e}{\rho} \frac{A'_i}{A_o},$$

where

$$(4.29) \quad C'_r = \frac{1}{2}(C'_k + C'^{*}_k)$$

and

$$(4.30) \quad C'_i = -\frac{i}{2}(C'_k - C'^{*}_k)$$

We can combine the tube law (eqn. 4.27 and 4.28) into the momentum equations (eqn. 4.25 and 4.26) to obtain

$$(4.31) \quad A_b \frac{\partial u'_r}{\partial t} + A'_r \frac{\partial u_b}{\partial t} - A_b u_b k u'_i = A_b k \frac{K_e}{\rho} \frac{A'_i}{A_o} - \beta_p \pi \nu u'_r + \phi_b A'_r$$

$$(4.32) \quad A_b \frac{\partial u'_i}{\partial t} + A'_i \frac{\partial u_b}{\partial t} + A_b u_b k u'_r = -A_b k \frac{K_e}{\rho} \frac{A'_r}{A_o} - \beta_p \pi \nu u'_i + \phi_b A'_i$$

4.2.4. Floquet Analysis

The linearized perturbation equations are parametric, such that the coefficient ϕ_b is a periodic function of time. The heartbeat angular frequency ω imposed in the base solution can drive the perturbations D' , where $D \in [u, A]$ to grow exponentially.

This effect is captured by allowing the perturbations to take the Floquet form[161].

$$(4.33) \quad D'_r = e^{(\mu+i\alpha\omega)t} F(t \bmod 2\pi/\omega)$$

where the function F is periodic in time with period $2\pi/\omega$. The growth rate μ determines the stability of the system. If $\mu < 0$ for all wavenumbers k , the amplitude of all perturbations decay in time; otherwise if $\mu > 0$ for any wavenumber k , the base solution becomes unstable. F can be decomposed as a Fourier sum over all frequency modes of ω to give

$$(4.34) \quad D'_r = \sum_{-\infty}^{\infty} \hat{D}_{r,n} e^{[\mu+i(n+\alpha)\omega]t} \quad D'_i = \sum_{-\infty}^{\infty} \hat{D}_{i,n} e^{[\mu+i(n+\alpha)\omega]t}$$

The partial derivatives of D'_r , D'_i with respect to time become

$$(4.35) \quad \frac{\partial D'_r}{\partial t} = \sum_{-\infty}^{\infty} [\mu + i(n + \alpha)\omega] \hat{D}_{r,n} e^{[\mu+i(n+\alpha)\omega]t} \quad \frac{\partial D'_i}{\partial t} = \sum_{-\infty}^{\infty} [\mu + i(n + \alpha)\omega] \hat{D}_{i,n} e^{[\mu+i(n+\alpha)\omega]t}$$

These perturbation solutions can be substituted into the linearized governing equations (eqn. 4.23, 4.24, 4.25, 4.25, 4.27, and 4.27), yielding the characteristic equations

$$(4.36) \quad [\mu + i(n + \alpha)\omega] \hat{A}_{r,n} - A_m k \hat{u}_{i,n} - u_m k \hat{A}_{i,n} - \frac{k}{2} \bar{u}_\omega \hat{A}_{i,n-1} - \frac{k}{2} \bar{u}_\omega^* \hat{A}_{i,n+1} = 0,$$

$$(4.37) \quad [\mu + i(n + \alpha)\omega] \hat{A}_{i,n} + A_m k \hat{u}_{r,n} + u_m k \hat{A}_{r,n} + \frac{k}{2} \bar{u}_\omega \hat{A}_{r,n-1} + \frac{k}{2} \bar{u}_\omega^* \hat{A}_{r,n+1} = 0,$$

$$(4.38) \quad \begin{aligned} & A_m [\mu + i(n + \alpha)\omega] \hat{u}_{r,n} - A_m u_m k \hat{u}_{i,n} - \frac{A_m k \bar{u}_\omega}{2} \hat{u}_{i,n-1} \\ & - \frac{A_m k \bar{u}_\omega^*}{2} \hat{u}_{i,n+1} + \frac{i\omega \bar{u}_\omega}{2} \hat{A}_{r,n-1} - \frac{i\omega \bar{u}_\omega^*}{2} \hat{A}_{r,n+1} = \\ & \frac{A_m k K_e}{\rho A_o} \hat{A}_{i,n} - \beta_p \pi \nu \hat{u}_{r,n} + \phi_m \hat{A}_{r,n} + \frac{\bar{\phi}_\omega}{2} \hat{A}_{r,n-1} + \frac{\bar{\phi}_\omega}{2} \hat{A}_{r,n+1}, \end{aligned}$$

$$\begin{aligned}
(4.39) \quad & A_m[\mu + i(n + \alpha)\omega]\hat{u}_{i,n} + A_m u_m k \hat{u}_{r,n} + \frac{A_m k \bar{u}_\omega}{2} \hat{u}_{r,n-1} \\
& + \frac{A_m k \bar{u}_\omega^*}{2} \hat{u}_{r,n+1} + \frac{i\omega \bar{u}_\omega}{2} \hat{A}_{i,n-1} - \frac{i\omega \bar{u}_\omega^*}{2} \hat{A}_{i,n+1} = \\
& - \frac{A_m k K_e}{\rho A_o} \hat{A}_{r,n} - \beta_p \pi \nu \hat{u}_{i,n} + \phi_m \hat{A}_{i,n} + \frac{\bar{\phi}_\omega}{2} \hat{A}_{i,n-1} + \frac{\bar{\phi}_\omega}{2} \hat{A}_{i,n+1}.
\end{aligned}$$

4.2.5. Dimensionless Form

To simplify the representation, we introduce the following length and time scales $L \rightarrow \sqrt{A_m}$, $T \rightarrow \frac{2A_m}{\beta_b \pi \nu}$, and a dimensionless group $N_T \rightarrow \frac{K_e A_m^2}{\rho A_o (\frac{\beta_b}{2} \pi \nu)^2}$. The physical parameters in the problem become $\tilde{\mu} = T\mu$, $\tilde{\omega} = T\omega$, $k'' = kL\sqrt{N_T}$, $\tilde{A} = \frac{\hat{A}}{L^2}$, $u'' = \frac{\hat{u}T}{L\sqrt{N_T}}$, $N_m = \frac{\phi_m T^2}{L\sqrt{N_T}}$, and $N_\omega = \frac{\bar{\phi}_\omega T^2}{L\sqrt{N_T}}$. Using these terms, the dimensionless forms of the characteristic equations (eqn. 4.36, 4.37, 4.38 and 4.39) are

$$(4.40) \quad [\tilde{\mu} + i(n + \alpha)\tilde{\omega}]\tilde{A}_{r,n} - k'' u''_{i,n} - \frac{N_m}{2} k'' \tilde{A}_{i,n} - \frac{N_\omega}{2(2 + i\tilde{\omega})} k'' \tilde{A}_{i,n-1} - \frac{N_\omega}{2(2 - i\tilde{\omega})} k'' \tilde{A}_{i,n+1} = 0$$

$$(4.41) \quad [\tilde{\mu} + i(n + \alpha)\tilde{\omega}]\tilde{A}_{i,n} + k'' u''_{r,n} + \frac{N_m}{2} k'' \tilde{A}_{r,n} + \frac{N_\omega}{2(2 + i\tilde{\omega})} k'' \tilde{A}_{r,n-1} + \frac{N_\omega}{2(2 - i\tilde{\omega})} k'' \tilde{A}_{r,n+1} = 0$$

$$\begin{aligned}
(4.42) \quad & [\tilde{\mu} + i(n + \alpha)\tilde{\omega}]u''_{r,n} - \frac{N_m}{2} k'' u''_{i,n} - \frac{N_\omega}{2(2 + i\tilde{\omega})} k'' u''_{i,n-1} \\
& - \frac{N_\omega}{2(2 - i\tilde{\omega})} k'' u''_{i,n+1} + \frac{i\tilde{\omega} N_\omega}{2(2 + i\tilde{\omega})} \tilde{A}_{r,n-1} - \frac{i\tilde{\omega} N_\omega}{2(2 - i\tilde{\omega})} \tilde{A}_{r,n+1} \\
& - k'' \tilde{A}_{i,n} + 2 \frac{\beta_p}{\beta_b} u''_{r,n} - N_m \tilde{A}_{r,n} - \frac{N_\omega}{2} \tilde{A}_{r,n-1} - \frac{N_\omega}{2} \tilde{A}_{r,n+1} = 0
\end{aligned}$$

$$\begin{aligned}
(4.43) \quad & [\tilde{\mu} + i(n + \alpha)\tilde{\omega}]u''_{i,n} + \frac{N_m}{2}k''u''_{r,n} + \frac{N_\omega}{2(2 + i\tilde{\omega})}k''u''_{r,n-1} \\
& + \frac{N_\omega}{2(2 - i\tilde{\omega})}k''u''_{r,n+1} + \frac{i\tilde{\omega}N_\omega}{2(2 + i\tilde{\omega})}\tilde{A}_{i,n-1} - \frac{i\tilde{\omega}N_\omega}{2(2 - i\tilde{\omega})}\tilde{A}_{i,n+1} \\
& + k''\tilde{A}_{r,n} + 2\frac{\beta_p}{\beta_b}u''_{i,n} - N_m\tilde{A}_{i,n} - \frac{N_\omega}{2}\tilde{A}_{i,n-1} - \frac{N_\omega}{2}\tilde{A}_{i,n+1} = 0
\end{aligned}$$

The important parameters describing the oscillatory component of flow through the vessel—including blood viscosity, vessel diameter, pressure driven acceleration, and viscous contribution under pulsatile waveform of the flow—have been collected in a single dimensionless number N_ω . Akin to the role of the Reynolds number in describing the onset of turbulence, the stability parameter tracks the inception of the flutter type instability. The other nondimensional group N_m scales with the mean field velocity u_m and is typically much smaller than N_ω which scales with u_ω , the oscillatory amplitude of the velocity in time.

Here, $\tilde{\omega}$ encapsulates the dimensionless angular frequency of a heart beat cycle. For a solution $x = [\tilde{A}_{r,n}, \tilde{A}_{i,n}, u''_{i,n}, u''_{r,n}]$ to exist, the determinant of the matrix equation $Ax=0$ (eqn. 4.40, 4.41, 4.42 and 4.43) must be identically zero. Satisfying this determinant condition for $\tilde{\mu} = 0$ gives a dispersion relationship between the wavenumber k'' of the perturbation and the dimensionless parameter N_ω along the marginal stability curve. This relationship holds for input values of the oscillatory frequency $\tilde{\omega}$ and mean field group N_m specific to the flow scenario. For values of N_ω below this curve, perturbation amplitudes decay in time, while above this curve the base state becomes unstable.

Fig. 4.3A) plots the dispersion relationship for representative values of the angular frequency $\tilde{\omega} = 5.9$, $N_m = 1.4 \times 10^{-2}$ and $\beta_p/\beta_b = 1.4$ corresponding to human physiology.

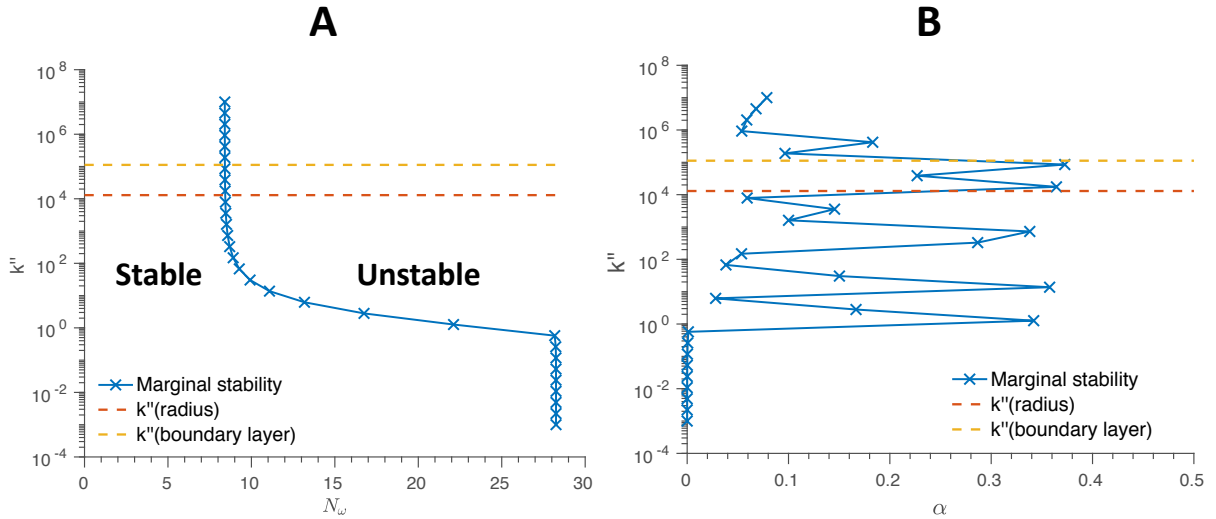


Figure 4.3. **A)** The marginal stability curve depicting the dispersion relationship between the dimensionless wave number k'' of the perturbation mode and the dimensionless parameter N_ω , which encapsulates the blood viscosity, vessel diameter, pressure driven acceleration, and viscous contribution under pulsatile waveform of the flow. For a given k'' , N_ω larger than the value on the marginal stability curve indicates that the system is unstable as the perturbation amplitude will grow, and vice versa. **B)** The imaginary component of the Floquet multiplier α on the marginal stability curve. For small wavenumbers k'' , $\alpha = 0$ indicates that only harmonic cases are relevant. Near order one k'' , the system undergoes a Neimark-Sacker [163] or secondary Hopf bifurcation in which $0 < \alpha < 0.5$.

The marginal stability curve appears to plateau for larger values of the wavenumber k'' but does not asymptote to a constant value even for nanoscale spatial wavelengths, associated with large k'' on the order of 10^{10} . There is thus no value of N_ω below which the system remains unconditionally stable for all k'' .

This may be a limitation of the 1D analysis, as we expect higher wave number modes to be filtered out by viscous effects, especially above the viscous wave number k'' (boundary layer) associated with the boundary layer thickness of flow inside the vessel. The mathematical representation of this limitation is that the viscous coefficient β_p/β_b does not

scale with k'' in eqn. 4.42 and eqn. 4.43. We expect that a full 3D treatment of this problem should allow the marginal stability curve in Fig. 4.3A) to curve back towards larger N_ω for wave numbers above k'' (boundary layer), as is commonly seen in such dispersion relationships [164].

Nonetheless, we note that the inertial regime dominates near the wave number k'' (radius) associated with vessel radius R . Perturbation modes near k'' (radius) correspond to the natural length scale of the system and should be accurately captured by the current analysis given that viscous effects are small in this neighborhood. The variation of N_ω between k'' (radius) and k'' (boundary layer) is typically 0.1% of the mean value. Thus, we select the value of N_ω on the marginal stability curve at k'' (radius) as the the threshold value $N_{\omega,\text{crit}}$ for the system.

Essentially, have used $N_{\omega,\text{crit}}$ at the wave number k'' (radius) to approximate the true, minimum N_ω on the marginal stability curve. A full, 3D analysis of flow through the vessel should be done to determine the error in this approximation; such an undertaking is outside the scope of the present work.

The physical significance of $N_{\omega,\text{crit}}$ lies in what claims we can make about a system exhibiting N_ω relative to this threshold value. If $N_\omega > N_{\omega,\text{crit}}$, the blood vessel will be unstable to a waveband of perturbation modes, whereas below this threshold, the base flow should remain stable.

For completeness, Fig. 4.3B) also displays the imaginary component of the Floquet multiplier α on the marginal stability curve. For small wavenumbers k'' , $\alpha = 0$ indicates that only harmonic cases corresponding to real Floquet exponents are relevant. Near order one k'' , the system undergoes a Neimark-Sacker (NS) [163] or secondary Hopf

bifurcation in which $0 < \alpha < 0.5$. For N_ω above the marginal stability curve, the system transitions from stable periodic oscillations to unstable divergent trajectories through a subcritical NS bifurcation. For N_ω below the marginal stability curve, the system transitions from stable periodic oscillations to quasi-periodic oscillations with secondary frequencies corresponding to nonzero α ; this results from a supercritical NS bifurcation.

4.2.6. Patient-specific instability

To determine the flow stability for a specific patient, the above formulation requires information about the wall stiffness K_e of the blood vessel. This physiological parameter can be found from the pulse wave velocity (PWV) measured from imaging techniques such as MRI scans and echocardiograms. The PWV is the propagation speed of the pulse wave in the aorta and is related to the elastic modulus or stiffness of the aortic wall. This relationship can be derived by transforming the set of simplified governing equations to the standard form of the wave equation [162]. The relevant conservation equations are

$$(4.44) \quad \frac{\partial A}{\partial t} + \frac{\partial Au}{\partial x} = 0,$$

$$(4.45) \quad \frac{\partial u}{\partial t} + u \frac{\partial u}{\partial x} = -\frac{\partial P}{\partial x},$$

where the viscous term has been neglected, and P is the dynamic pressure divided by the blood density. A general tube law is used

$$(4.46) \quad P = \frac{1}{\rho} G(A),$$

where G is some function of the local cross-sectional area. Without adding new notation, we next introduce an invertible change in the independent variables $x \rightarrow x + ut$ and $t \rightarrow t$ such that the velocity u is frozen at the mean value. In the new basis, the conservation equations become

$$(4.47) \quad \frac{\partial A}{\partial t} + A \frac{\partial u}{\partial x} = 0,$$

$$(4.48) \quad \frac{\partial u}{\partial t} + \frac{1}{\rho} \frac{dG}{dA} \frac{\partial A}{\partial x} = 0.$$

Differentiating the mass equation (eqn. 4.47) with respect to time and the momentum equation 4.48) with respect to space give

$$(4.49) \quad \frac{\partial^2 A}{\partial t^2} + A \frac{\partial^2 u}{\partial x \partial t} = 0,$$

$$(4.50) \quad \frac{\partial^2 u}{\partial x \partial t} + \frac{1}{\rho} \frac{dG}{dA} \frac{\partial^2 A}{\partial x^2} = 0,$$

which can be combined to obtain

$$(4.51) \quad \frac{\partial^2 A}{\partial t^2} - \left(\frac{1}{\rho} \frac{dG}{dA} A \right) \frac{\partial^2 A}{\partial x^2} = 0.$$

This is the standard form of the wave equation, where the term in brackets is typically called the propagation speed. It represents the speed of the plane wave solutions to eqn. 4.51. The pulse wave velocity can thus be defined as

$$(4.52) \quad c_{pw}^2 = \frac{1}{\rho} \frac{dG}{dA} A$$

For the purposes of the present analysis, the tube law term appears in the perturbation equations. By expansion around the base pressure P_b and area A_b ,

$$(4.53) \quad P = P_b + P' = P_b + \left. \frac{1}{\rho} \frac{dG}{dA} \right|_b A' = P_b + c_{pw}^2 \frac{A'}{A_b}.$$

We see that no matter which form the tube law $G(A)$ takes, the measured PWV can be used to quantify the vessel's elastic properties. The key dimensionless parameter becomes

$$(4.54) \quad N_\omega = \frac{\bar{\phi}_\omega A_b^{3/2}}{(\frac{\beta_b}{2} \pi \nu)} \sqrt{\frac{\rho A_o}{K_e}} = \frac{\bar{\phi}_\omega A_b}{\frac{\beta_b}{2} \pi \nu c_{pw}}.$$

Using eqn. 4.54, N_ω can now be calculated explicitly from clinical imaging data for each cross section along a blood vessel. The difference between this clinical, patient specific value $N_{\omega, \text{clin}}$ and the critical threshold $N_{\omega, \text{crit}}$ on the marginal stability curve produces an overall stability parameter

$$(4.55) \quad N_{\omega, \text{sp}} = N_{\omega, \text{clin}} - N_{\omega, \text{crit}}.$$

If $N_{\omega, \text{sp}} > 0$, the vessel cross section is expected to grow due to the increase in perturbation amplitude. Otherwise for $N_{\omega, \text{sp}} \leq 0$, the vessel diameter should remain constant in time since all perturbation modes decay. Thus, we have developed an ab-initio theoretical framework to predict the stability of an aortic section depending on a patient's aorta diameter A_b , oscillatory acceleration due to blood pressure $\bar{\phi}_\omega$, pulsatile contribution to wall shear β_b , blood viscosity ν , and blood density ρ . These values can be extracted from clinical imaging (A_b , $\bar{\phi}_\omega$, and β_b) as well as literature ($\nu \approx 4e - 3 \text{ N s/m}^2$ and $\rho \approx 1060 \text{ kg/cm}^3$ [166]).

We propose that the stability parameter $N_{\omega,sp}$ can be used as a physiomarker to forecast aneurysm development. If the stability parameter at a local cross-section of the blood vessel satisfies $N_{\omega,sp} > 0$, we hypothesize that the growth of perturbation modes will trigger the cross-sectional area of the vessel to dilate permanently over time. Otherwise if $N_{\omega,sp} \leq 0$, perturbation amplitudes will decay, and the vessel should remain stable.

4.3. Methodology

To gauge the performance of this physiomarker in analyzing aneurysm growth, a retrospective study was carried out for patients with and without existing aortopathies.

4.3.1. Cohort Selection

A database of patients and indicated for clinical cardiac imaging, including 4D flow MRI, at Northwestern Memorial Hospital between 2011 and 2019 was queried to identify a list of subjects with suspected isolated aortopathy and normal, tricuspid aortic valve (TAV). Exclusion criteria were aortic valve stenosis (mild to severe), ejection fraction lower than 50%, bicuspid aortic valve, history of aortic dissection, or history of valve replacement or aortic repair. Subjects both with and without aortic dilatation — clinical measurement of maximal-area ascending aortic (MAA) or sinus of valsalva (SOV) diameter greater or equal to 4 cm — were included.

An additional group of healthy subjects was assembled as a control cohort. These subjects were drawn from a separate database of prospectively-recruited healthy volunteers who received 4D flow MRI. Subjects eligible for enrollment were 18 and older, and with

no known cardiovascular disease or abnormalities. The cohort for analysis was chosen from the overall group of recruited volunteers to be uniformly distributed by age and sex.

All subjects were included in this study with oversight by and approval from the Northwestern University Institutional Review Board. Patients were enrolled by retrospective chart review and waiver of consent. Healthy subjects were enrolled with prospectively obtained informed consent.

4.3.2. Clinical chart reviews and patient outcomes classification

Clinical patient records were reviewed comprehensively to identify the occurrence or lack of aortic diameter growth or aortic surgery after the 4D flow imaging for each patient. Aortic diameter growth was assessed from radiological measurements taken with CT or MR angiography imaging, which included standardized assessment of MAA and SOV diameter in double-oblique view. Aortic surgery events included any surgical replacement or repair of the aortic valve or any portion of the aorta between sinus and arch. Times between 4D flow imaging and follow-up measurements or surgical events were noted.

Cohort Characteristics. From the database of subjects with clinically indicated cardiac and 4D flow MRI, a total of 119 patients with suspected aortopathy and normal TAV were identified for potential inclusion in this study. Of the patients identified, 26 were excluded due to lack of sufficient follow-up data, which was defined as at least one angiography exam occurring subsequent to the 4D flow imaging analyzed here. A further 18 were excluded for having concurrent conditions, such as history of congenital heart malformations, prior valve repair operations, or genetic connective tissue disorder. The final cohort of patients comprised 75 subjects. The age range in patients was 29 years to 79 years, and 23%

	controls ($n = 100$)	patients ($n = 75$)
age (years)	46.4 ± 15.5 [19,79]	58.5 ± 11.7 [29,79]
sex (female)	51 [51%]	17 [23%]
height (m)	1.71 ± 0.11 [1.30,1.96]	1.77 ± 0.13 [1.40,2.30]
weight (kg)	79.1 ± 17.9 [47.6,142.9]	86.4 ± 18.8 [45.5,140.9]
SOV (mm)	–	41.8 ± 4.8 [32.0,52.0]
MAA (mm)	–	39.1 ± 5.4 [27.0,47.0]

Table 4.1. Characteristics of the study cohort are summarized for age, sex, as mean \pm standard deviation and [minimum,maximum] of range or [percentage] values.

of the patients were female. Additionally, a total of 100 healthy control subjects were identified, and the selections represented a wide range of ages and sexes in the cohort, with subjects aged 19 years to 79 years and 51% of the group female. The cohort demographic characteristic statistics are summarized in table 4.1.

4.3.3. Image Acquisition and Preprocessing

Clinical imaging was performed at 1.5T and 3T (Aera/Avanto/Espreo, Siemens, Germany). Sequence parameters for 4D flow MRI included $1.2\text{--}3.1 \times 1.2\text{--}3.1 \times 1.2\text{--}5.0 \text{ mm}^3$ / 33–45 ms spatial / temporal resolution; $12.4\text{--}40.6 \times 18.0\text{--}50.0 \times 3.8\text{--}17.6 \text{ mm}^3$ field of view; 80–500 cm/s VENC, as appropriate, determined from flow scout image; 2.1–3.0 ms TE, 4.1–5.7 ms TR, 7–25° tip angle; and respiratory navigators for free-breathing scans. Images for all subjects were acquired between January 2011 and December 2019. Pre-processing of 4D flow MRI data included previously-described methods for correction of background phase from eddy currents and Maxwell terms and for velocity phase

un-aliasing [165]. Preprocessing was performed with commercial computational software (MATLAB, Mathworks, Natick, Massachusetts). Following preprocessing, a three-dimensional segmentation of the thoracic aorta was performed using commercial image processing software (Mimics Innovation Suite, Materialize, Leuven, Belgium).

4.3.4. Image Processing

The 4D flow MRI provides information about the three-dimensional geometry of the aorta as well as the velocity field inside it. The 3D geometry is time-averaged from velocity contrast, and therefore remains constant in time. Fig. 4.4(a) shows the time-averaged geometry of an aorta from a 4D flow MRI. The geometry is generated on a Cartesian grid of voxels which have a binary value, i.e., voxels lying outside and inside the aorta have a value of 0 and 1, respectively. The measured velocity field is a function of both space and time.

Our analysis was focused only on the ascending part of the aorta, from the aortic root to just below the three branches at the aortic arch. This region is shown inside the red box in Fig. 4.4 (a) and more clearly zoomed in Fig. 4.4(b). The upper and lower limits of the ascending aorta were segmented manually.

To model the ascending part of the aorta in a one-dimensional model, we find the variation of cross-sectional area and mean velocity along its length. A centerline is first generated through the ascending aorta (Fig. 4.4(b)). Normal planes are then generated. These planes were used to calculate the cross-sectional areas and mean velocities at every point along the centerline. Voxels on each plane are then meshed using Delaunay triangulation (Fig. 4.4(c)). The sum of these triangles is the cross-sectional area A_b of the aorta

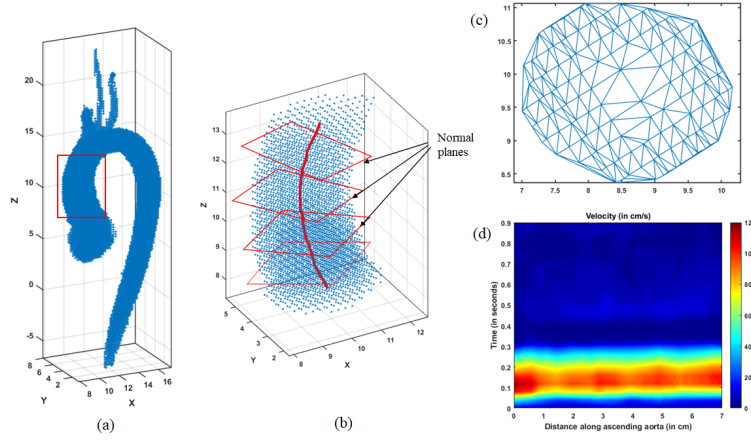


Figure 4.4. Cross-sectional areas and mean velocity field from 4D flow MRI of the aorta. (a) Time-averaged 3D geometry of the aorta. The red box marks the ascending aorta. The axes units are in cm; (b) Point cloud (in blue) showing the ascending aorta. The red curve shows the centerline, and the red boxes show the planes normal to the centerline. These planes are used to calculate the cross-sectional areas and mean velocities. The axes units are in cm; (c) An example of the aorta cross-section on a normal plane. Meshing is done using Delaunay triangulation to calculate the cross-sectional area at the normal plane. The axes units are in cm; (d) Variation of mean velocity as a function of time and length along the ascending aorta.

at a particular centerpoint. The mean velocity at each cross-section are calculated by

$$(4.56) \quad u(x, t) = \frac{1}{N} \sum_i^N \mathbf{v}_i(x, t) \cdot \hat{\mathbf{n}},$$

where u is the mean velocity at the centerline, i represents the i -th point in plane, N is the total number of points, \mathbf{v}_i is the velocity at the i -th point, $\hat{\mathbf{n}}$ is the unit normal to the plane, x is the distance along the centerline, and t is time. The variation of $u(x, t)$ during a cardiac cycle is shown in Fig. 4.4(d).

These velocity profiles can be used to calculate the $\bar{\phi}_b$ via 4.13 as well as the pulse wave velocity c_{pw} [167]. All physiological parameters needed to calculate $N_{\omega,sp}$ can therefore be extracted from MRI imaging.

4.4. Results and Discussion

A total of 71 patients in the case cohort had at least one clinical follow-up visit so that their growth rate could be quantified. These patients also did not exhibit any imaging artifacts in their initial, baseline MRI. The maximum of their SOV and MAA diameters (SOV_{max} and MAA_{max}) recorded during each clinic visit are presented as a time series after their initial MRI at year 0 (Fig. 4.5A, 4.5B). The choice of the maximum diameter rather than the mean value abides by standard clinical practice for radiologists in annotating growth impressions of the patient over time.

The evolution of SOV_{max} is characterized by the maximum rate of change ΔSOV_{max} over sequential follow-up imaging. For the patient specific data in Fig. 4.5A, $\Delta SOV_{max} = 0.39$ cm/year due to a stepwise jump in measured SOV_{max} between years 2 to 3. This growth rate is defined analogously for the maximum MAA diameter; Fig. 4.5B gives $\Delta MAA_{max} = 0.19$ cm/year for the same patient. Although a line could be fit to the data to extract an average growth rate, this approach is not indicative of standard practice. Radiologists typically take the the maximum diameter difference between sequential follow-ups to quantify growth. This method is susceptible to outliers, but the usual approach is to bring in the patient for a second follow-up within a short time period if the growth rate measured differs significant from the patient's prior history.

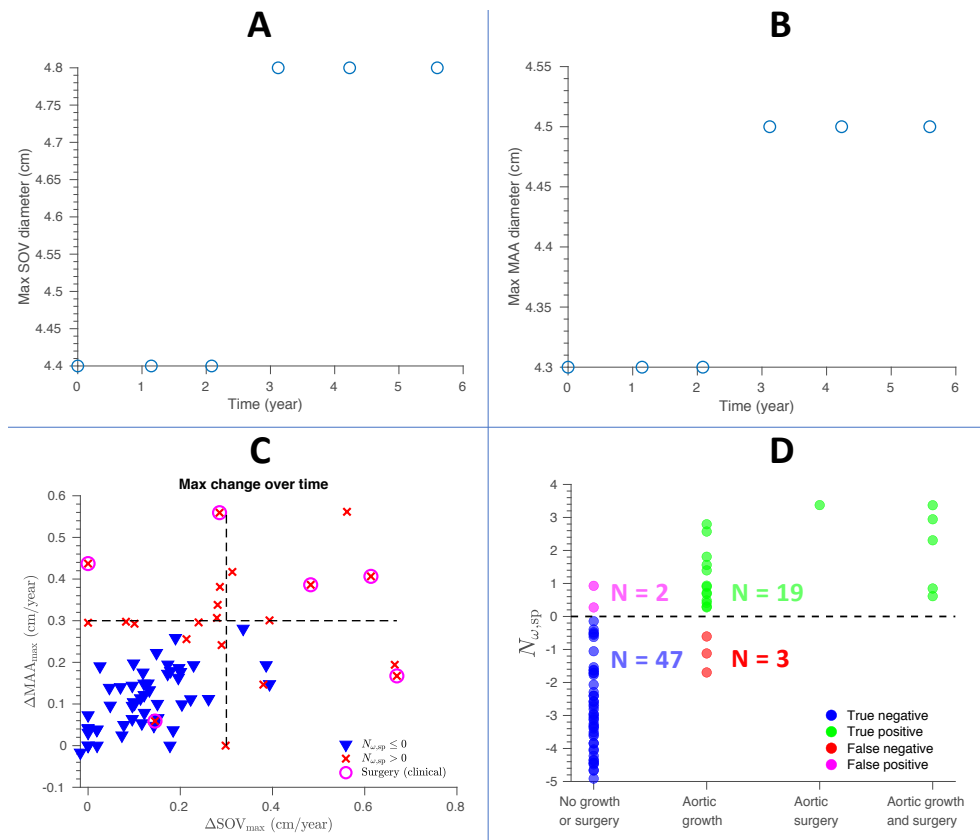


Figure 4.5. **A)** The maximum SOV diameter recorded during each clinical visit. The initial MRI was processed at year 0. **B)** The maximum MAA diameter recorded during each clinical visit. **C)** A phase diagram of patients with follow-up imaging data. The maximum growth rate of their MAA and SOV in (cm/year) are visualized with respect to theoretical prediction $N_{\omega,sp}$. If $N_{\omega,sp} > 0$, the patient's marker is labeled by "x". Otherwise, the data point is labeled by "∇". The circles indicate that the patient experienced a surgical outcome after their initial MRI at year 0. $N_{\omega,sp} > 0$ appears to correlate with larger growth rates for the MAA and SOV. **D)** Each patient has been labeled according to whether $N_{\omega,sp} > 0$ accurately predicts a growth outcome, quantitatively categorized as exhibiting a growth rate in SOV or MAA ≥ 0.29 cm/year. This threshold is considered an indication for more frequent surveillance as it lies outside the range of normal growth rates in the thoracic aorta.

The per patient growth rates for the SOV and MAA are visualized in Fig. 4.5C and compared with our theoretical predictions. Each "x" in Fig. 4.5C denotes $N_{\omega,sp} > 0$, as

calculated from the patient’s MRI image at year 0. This indicates that the ascending aorta is expected to grow due to the flutter type instability. Conversely, each “ ∇ ” represents $N_{\omega,sp} \leq 0$. Since all perturbation modes are damped in this case, the ascending aorta should not be subject to the identified instability. Patients who experienced surgical outcomes after their initial MRI are circled. Growth rates exceeding 0.3 cm/year lie outside the range of normal growth of the thoracic aorta. Dilation of the SOV or MAA above this threshold is clinically recognized as a significant interval increases in aortic dimension and serves as an indication for more frequent surveillance [168]. This threshold for abnormal growth has been included as well in Fig. 4.5C.

We observe that the $N_{\omega,sp}$ appears to correlate with larger growth rates in both the MAA (Pearson correlation of 0.61, with a p-value of 10^{-8}) and SOV (Pearson correlation of 0.62, with a p-value of 4×10^{-9}). Fig. 4.5D shows that by using aortic growth rates of 0.29 cm/year as an indicator of significant growth, the stability parameter $N_{\omega,sp} > 0$ serves as a good binary predictor for the growth outcome of each patient. This threshold of significant growth of 0.29 cm/year is the optimal operating point that maximizes sensitivity and specificity of the physiometer and is remarkably close to the clinical threshold used in practice [168].

The accuracy, sensitivity, and specificity of this proposed physiometer in predicting abnormal growth in the thoracic aorta are 0.93, 0.86, and 0.96, respectively. The area under the curve of a receiver operating characteristic (ROC) analysis is 0.96, which is typically considered “outstanding” for the performance of a binary predictive diagnostic [169]. Additionally, the optimal operating point occurs at the minimum positive value for $N_{\omega,sp}$ for patients with follow-up data, suggesting that the analytically derived threshold

	$N_{\omega,sp} > 0$				$N_{\omega,sp} \leq 0$			
	$\bar{\phi}_\omega$ m/s ²	c_{pw} m/s	A_b cm ²	β none	$\bar{\phi}_\omega$ m/s ²	c_{pw} m/s	A_b cm ²	β none
Patients								
median	7.5915	3.5524	9.1440	25.7694	6.2827	6.5385	9.4793	25.9611
p-value between $N_{\omega,sp}$	0.0027	2×10^{-11}	0.3056	0.4049	-	-	-	-
p-value between cohorts	0.0940	0.0007	0.0115	0.0105	0.0246	3×10^{-5}	3×10^{-5}	7×10^{-6}
Normal subjects								
median	10.7675	5.3595	6.3685	21.8522	6.9409	8.7686	7.7526	24.0146
p-value between $N_{\omega,sp}$	0.0098	0.0042	0.1394	0.0718	-	-	-	-

Table 4.2. Each physiological term that contributes to measuring the stability parameter $N_{\omega,sp}$ is tabulated for both patients and normal subjects—the patient’s aorta diameter A_b , oscillatory acceleration due to blood pressure $\bar{\phi}_\omega$, pulsatile contribution to wall shear β_b , and pulse wave velocity c_{pw} . The one-tailed Wilcoxon rank sum test was used to determine whether the larger median of one population (e.g. patients, $N_{\omega,sp} > 0$) is significantly greater than the smaller median of the other (e.g. patients, $N_{\omega,sp} < 0$). The row of p-values comparing patient and normal subject cohorts is colored red, while the row of p-values comparing $N_{\omega,sp} > 0$ and $N_{\omega,sp} \leq 0$ is colored blue. Rejection of the null hypothesis at the 5% level is colored purple.

$N_{\omega,crit}$ accurately describes the onset of the underlying instability. No training data set was necessary to “tune” the calculation of the physiometer.

4.4.1. Normal subject and patient cohorts

Next, the distributions of the stability parameter $N_{\omega,sp}$ in both the normal subject cohort and the patient cohort are examined. A few salient points are reported here.

As seen in Fig. 4.6, the median physiomer value for the normal subject cohort is shown to be significantly ($p = 2 \times 10^{-7}$) smaller than that for the patient cohort, via a one-tailed Wilcoxon rank sum test. This agrees with the inclusion criteria used to establish the patient and normal subject cohorts, suggesting that the physiomer discriminates the abnormal features driving aneurysm growth. The sample size of both cohorts exceed 32, the value required to establish a difference in their median values at a significance level of ($p < 0.005$) with 90% statistical power.

Table 4.2 shows the breakdown of component physiological properties that make up the physiomer $N_{\omega,sp}$ for the two cohorts. In the normal subject cohort, a positive stability parameter $N_{\omega,sp} > 0$ can be caused by two significant factors. The first is larger ($p = 0.0098$) blood flow acceleration $\bar{\phi}_{\omega}$ driven by the oscillatory pressure gradient during the cardiac cycle. Normal subjects with unstable physiomer $N_{\omega,sp} > 0$ exhibit larger $\bar{\phi}_{\omega}$ compared to normal subjects with a stable physiomer $N_{\omega,sp} \leq 0$ in a one-tailed Wilcoxon rank sum test. The second factor is smaller ($p = 0.0042$) pulse wave velocity c_{pw} , which indicates lower aortic stiffness. Such aortic walls distend farther under the same pressure gradient compared to aortas characterized by larger c_{pw} .

In the patient cohort, a positive stability parameter $N_{\omega,sp} > 0$ is also driven by a significantly larger ($p = 0.0027$) acceleration $\bar{\phi}_{\omega}$ and smaller ($p = 2 \times 10^{-11}$) pulse wave velocity. This suggests that the main factors underlying aneurysm growth and formation in both patients with existing aortopathies and normal subjects are similar. However, a feature by feature comparison shows that that the physiological properties in the two cohorts differ significantly across the board.

First, the aortic areas A_b for both stable $N_{\omega,sp} \leq 0$ and unstable $N_{\omega,sp} > 0$ patients are significantly larger than that for subjects. This agrees with the selection criteria for the two cohorts, in that patients were indicated for cardiac imaging due to possible aortopathies. Similarly, the pulse wave velocities for stable $N_{\omega,sp} \leq 0$ and unstable $N_{\omega,sp} > 0$ patients are significantly smaller than that for subjects. This suggests that as aneurysms dilate towards larger sizes, the aortic wall weakens and becomes less stiff. Such a process can form a self-reinforcing cycle since the thinning of the intimal wall during aneurysm expansion decreases the elastic modulus, which induces farther dilation when $N_{\omega,sp} > 0$.

Next, we note the wall shear coefficients β due to pulsatile flow for both stable $N_{\omega,sp} \leq 0$ and unstable $N_{\omega,sp} > 0$ patients are significantly larger than that for subjects. This difference arises from the larger pulsatile frequency ω observed in patients, which reduces the width of the viscous boundary layer but also increases the resulting wall shear stress. In patients, Cliff's delta $\delta_C = 0.0280$ between the stable $N_{\omega,sp} \leq 0$ and unstable $N_{\omega,sp} > 0$ populations. This means that distance between the two distributions for β is negligible, suggesting that this wall shear does not play a significant role in driving aneurysm growth for larger aneurysms. In normal subjects, however, Cliff's delta $\delta_C = 0.3605$ between the stable $N_{\omega,sp} \leq 0$ and unstable $N_{\omega,sp} > 0$ populations. Thus, wall shear contributes more significantly to triggering the flutter instability for small aneurysm sizes during the formative stage.

Lastly, Table 4.2 shows that the pressure driven acceleration $\bar{\phi}_\omega$ for the stable $N_{\omega,sp} \leq 0$ population of patients is significantly larger than that for stable subjects. This may arise due to both the expansion in aortic dimensions as well as blood pressure management prescribed clinically for patients with aortopathies. For patients, the Cliff's delta $\delta_C =$

0.7608 for the difference in pulse wave velocity c_{pw} , while $\delta_C = 0.3199$ for the difference in acceleration $\bar{\phi}_\omega$ between the stable $N_{\omega,sp} \leq 0$ and unstable $N_{\omega,sp} > 0$ populations. Meanwhile for normal subjects, the Cliff's delta $\delta_C = 0.6473$ for the difference in pulse wave velocity c_{pw} , while $\delta_C = 0.5736$ for the difference in acceleration $\bar{\phi}_\omega$.

Thus, unstable $N_{\omega,sp} > 0$ aneurysms in patients are driven more significantly by the smaller pulse wave velocity, while unstable aneurysms in normal subjects are induced more significantly by larger pressure driven acceleration. We have pinpointed a fundamental difference between the growth mode of large aneurysms in patients and the development process of small aneurysms in normal subjects, which may arise from both disease progression and clinical treatment.

4.4.1.1. Age and gender partitioning. Next, we bin the patient and normal subject cohorts into different age and gender groups. Unsurprisingly, we see significant difference in the physiometer $N_{\omega,sp}$ between the two cohorts. The stability parameter is larger in the patient cohort for both male and female subjects in the age groups (Age < 40) and (60 ≤ Age), indicating greater growth in aneurysms for patients. This suggests that neither age nor gender are confounding factors for the different physiometer $N_{\omega,sp}$ distributions in the two cohorts.

In the patient population, the physiometer is systematically though not significantly larger for females than males in each age group. This

[?]

Each of the age stratified categories (Age < 40, 40 ≤ Age < 60, and 60 ≤ Age) showed a significantly smaller median physiometer value (p<0.005) for the subject population than for the corresponding category in the patient population, for ages 30 and up. This

suggests that age is not a confounding factor for the different $N_{\omega,sp}$ distributions in the two cohorts.

Considering the normal subject cohort only, the median physiomer value was significantly smaller ($p < 0.005$) for subjects of ages < 60 , compared to those with ages ≥ 60 . Additionally, the median physiomer value measured for men was significantly larger ($p < 0.005$) than for women. This complies with clinical observation that that the risk of developing TAAs increases with age, and is greater for men than women [149]. These observed population markers for TAAs appear to agree with the general distribution of $N_{\omega,sp}$.

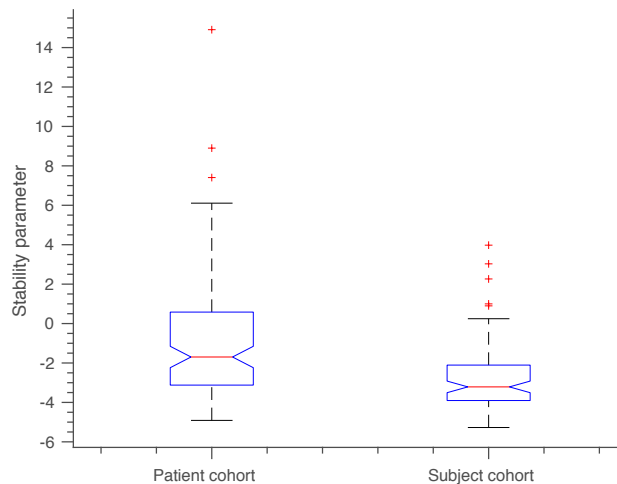


Figure 4.6. **A)** The distribution of the stability parameter $N_{\omega,sp}$ in the patient and normal subject cohorts. The median physiomer value for the normal subject cohort is shown to be significantly ($p < 0.005$) smaller than that for the patient cohort, via a one-tailed Wilcoxon rank sum test.

	$N_{\omega,sp}$		
	Age < 40	$40 \leq \text{Age} < 60$	$60 \leq \text{Age}$
Patients			
median (female)	-1.7870	-1.5444	-0.1496
p-value between genders	0.5301	0.4590	0.3085
p-value (female) between age groups	0.3304	0.2720	0.4492
p-value (female) between cohorts	0.0485	0.0608	0.0035
median (male)	-1.9003	-1.6373	-1.7122
p-value (male) between age groups	0.2706	0.3807	0.4516
p-value (male) between cohorts	0.0089	0.1154	0.0017
Normal subjects			
median (female)	-2.9578	-3.3852	-3.6360
p-value between genders	0.5066	0.0860	0.3365
p-value (female) between age groups	0.2843	0.1160	0.0633
median (male)	-3.2141	-2.7179	-4.0342
p-value (male) between age groups	0.2661	0.0076	0.0296

Table 4.3. The stability parameter $N_{\omega,sp}$ stratified by age and gender. The one-tailed Wilcoxon rank sum test was used to determine whether the larger median of one population (e.g. patients, Age < 40, female) is significantly greater than the smaller median of the other (e.g. normal subjects, Age < 40, female). The row of p-values comparing patient and normal subject cohorts is colored red, while the row of p-values comparing genders is colored blue. The row of p-values comparing each age group is colored green; note that the p-value beneath Age < 40 tests the age groups Age < 40 and $40 \leq \text{Age} < 60$, the p-value beneath $40 \leq \text{Age} < 60$ tests the age groups $40 \leq \text{Age} < 60$ and $40 \leq \text{Age}$, and the p-value beneath $60 \leq \text{Age}$ tests the age groups $60 \leq \text{Age}$ and Age < 40. Rejection of the null hypothesis at the 5% level is colored purple.

4.5. Conclusion

To summarize, we analyzed the growth of aortic aneurysms from first principles by conducting a linear stability analysis of the integral-averaged mass and momentum conservation equations describing the evolution of blood flow velocity through an elastic vessel with time and spatially varying cross-sectional area. The perturbation equations around the base flow gives us a matrix equation relating the temporal growth rate of each perturbation mode to its wave number. Floquet theory is used to account for the parametric effect of the heartbeat frequency—essentially, the time varying blood velocity waveform.

The important parameters describing the flow through the vessel—including viscosity, vessel diameter, pressure driven acceleration, etc.—are collected in a single dimensionless number, which we call the stability parameter. Akin to the role of the Reynolds number in describing the onset of turbulence, the stability parameter tracks the inception of the flutter type instability. If the stability parameter at a local cross-section of the blood vessel exceeds an analytically derived threshold, the growth of perturbation modes will trigger the cross-sectional area of the vessel to dilate. We therefore hypothesize that an aneurysm will form or grow at the site. Otherwise, perturbation amplitudes will decay in time, and the location should remain stable.

Through comparison with imaging data extracted from clinical visits, we've shown that the proposed stability parameter can be used as a physiomarker to forecast aneurysm growth. The only input to calculate the parameter for each patient was a baseline magnetic resonance imaging (MRI) scan taken during the initial visit. We found that patients who were predicted by this physiomarker to experience permanent aortic dilation were

significantly more likely to exhibit aneurysm growth and surgical outcomes rather than stable aneurysm sizes at clinical follow-up.

In summary, our work shows that the ab-initio physiomaerker can both predict the quantitative, time-dependent behavior of aneurysm evolution in patients from a single image as well as capture the observed qualitative population trends in subjects without an existing record of cardiac disease. Thus, we have initiated validation of both the diagnostic capability of the physiomaerker as well as its role as a fundamental mechanistic precursor to aneurysm formation and growth.

4.6. Author Contributions

Conceptualization- N.A.P. and T.Y.Z.; planning and supervision- N.A.P., M.M., T.Y.Z., and E.M.I.J; theoretical analysis- N.A.P., T.Y.Z., and G.E.; clinical methodology- M.M., E.M.I.J., B.A., T.Y.Z., S.H., and G.E.; writing- N.A.P., M.M., T.Y.Z., G.E., E.M.I.J., and S.H.

References

- [1] Bragg, M., Broeren, A. & Blumenthal, L. Iced-airfoil aerodynamics. *Progress in Aerospace Sciences* **41**, 323 – 362 (2005). URL <http://www.sciencedirect.com/science/article/pii/S0376042105000801>. DOI <http://dx.doi.org/10.1016/j.paerosci.2005.07.001>.
- [2] Barber, S., Wang, Y., Jafari, S., Chokani, N. & Abhari, R. S. The impact of ice formation on wind turbine performance and aerodynamics. *Journal of Solar Energy Engineering* **133**, 011007–011007 (2011). URL <http://dx.doi.org/10.1115/1.4003187>.
- [3] Antonini, C., Innocenti, M., Horn, T., Marengo, M. & Amirfazli, A. Understanding the effect of superhydrophobic coatings on energy reduction in anti-icing systems. *Cold Regions Science and Technology* **67**, 58 – 67 (2011). URL <http://www.sciencedirect.com/science/article/pii/S0165232X11000401>. DOI <http://dx.doi.org/10.1016/j.coldregions.2011.02.006>.
- [4] Jung, S., Tiwari, M. K., Doan, N. V. & Poulikakos, D. Mechanism of supercooled droplet freezing on surfaces. *Nature Communications* **3**, 615 EP – (2012). URL <http://dx.doi.org/10.1038/ncomms1630>.
- [5] Farhadi, S., Farzaneh, M. & Kulinich, S. Anti-icing performance of superhydrophobic surfaces. *Applied Surface Science* **257**, 6264 – 6269 (2011). URL <http://www.sciencedirect.com/science/article/pii/S0169433211002480>. DOI <http://dx.doi.org/10.1016/j.apsusc.2011.02.057>.
- [6] Kulinich, S. A., Farhadi, S., Nose, K. & Du, X. W. Superhydrophobic surfaces: Are they really ice-repellent? *Langmuir* **27**, 25–29 (2011). URL <http://dx.doi.org/10.1021/la104277q>. DOI 10.1021/la104277q. PMID: 21141839, <http://dx.doi.org/10.1021/la104277q>.
- [7] Subramanyam, S. B., Rykaczewski, K. & Varanasi, K. K. Ice adhesion on lubricant-impregnated textured surfaces. *Langmuir* **29**, 13414–13418 (2013). URL <http://dx.doi.org/10.1021/la402456c>. DOI 10.1021/la402456c. PMID: 24070257, <http://dx.doi.org/10.1021/la402456c>.

- [8] Stone, H. A. Ice-phobic surfaces that are wet. *ACS Nano* **6**, 6536–6540 (2012). URL <http://dx.doi.org/10.1021/nn303372q>. DOI 10.1021/nn303372q. PMID: 22876765, <http://dx.doi.org/10.1021/nn303372q>.
- [9] Findenegg, G. H., Jähnert, S., Akcakayiran, D. & Schreiber, A. Freezing and melting of water confined in silica nanopores. *ChemPhysChem* **9**, 2651–2659 (2008). URL <https://onlinelibrary.wiley.com/doi/abs/10.1002/cphc.200800616>. DOI 10.1002/cphc.200800616. <https://onlinelibrary.wiley.com/doi/pdf/10.1002/cphc.200800616>.
- [10] Alba-Simionesco, C. *et al.* Effects of confinement on freezing and melting. *Journal of Physics: Condensed Matter* **18**, R15 (2006). URL <http://stacks.iop.org/0953-8984/18/i=6/a=R01>.
- [11] González Solveyra, E., de la Llave, E., Scherlis, D. A. & Molinero, V. Melting and crystallization of ice in partially filled nanopores. *The Journal of Physical Chemistry B* **115**, 14196–14204 (2011). URL <http://dx.doi.org/10.1021/jp205008w>. DOI 10.1021/jp205008w. PMID: 21863824, <http://dx.doi.org/10.1021/jp205008w>.
- [12] Szedlak, A., Blanchard, A. V., Kostinski, A. B. & Cantrell, W. H. The Temperature Dependence of Water’s Latent Heat of Freezing. AGU Fall Meeting Abstracts (2009).
- [13] Çengel, Y. & Boles, M. *Thermodynamics: an engineering approach*. McGraw-Hill series in mechanical engineering (McGraw-Hill Higher Education, 2006). URL <https://books.google.com/books?id=5-hSAAAAMAAJ>.
- [14] Patankar, N. A. Supernucleating surfaces for nucleate boiling and dropwise condensation heat transfer. *Soft Matter* **6**, 1613–1620 (2010). URL <http://dx.doi.org/10.1039/B923967G>. DOI 10.1039/B923967G.
- [15] Jones, P. R., Elliott, A. R. & Patankar, N. A. Sustaining superheated liquid within hydrophilic surface texture. *Langmuir* **32**, 12947–12953 (2016). URL <http://dx.doi.org/10.1021/acs.langmuir.6b02665>. DOI 10.1021/acs.langmuir.6b02665. PMID: 27802595, <http://dx.doi.org/10.1021/acs.langmuir.6b02665>.
- [16] Varanasi, K. K., Deng, T., Smith, J. D., Hsu, M. & Bhate, N. Frost formation and ice adhesion on superhydrophobic surfaces. *Applied Physics Letters* **97**, 234102 (2010). URL <http://dx.doi.org/10.1063/1.3524513>. DOI 10.1063/1.3524513. <http://dx.doi.org/10.1063/1.3524513>.
- [17] Molinero, V. & Moore, E. B. Water modeled as an intermediate element between carbon and silicon. *The Journal of Physical Chemistry B* **113**, 4008–4016 (2009).

- URL <http://dx.doi.org/10.1021/jp805227c>. DOI 10.1021/jp805227c. PMID: 18956896, <http://dx.doi.org/10.1021/jp805227c>.
- [18] Li, K. *et al.* Viscosity of interfacial water regulates ice nucleation. *Applied Physics Letters* **104**, 101605 (2014). URL <https://doi.org/10.1063/1.4868255>. DOI 10.1063/1.4868255.
- [19] Coasne, B., Galarneau, A., Pellenq, R. J. M. & Di Renzo, F. Adsorption, intrusion and freezing in porous silica: the view from the nanoscale. *Chem. Soc. Rev.* **42**, 4141–4171 (2013). URL <http://dx.doi.org/10.1039/C2CS35384A>. DOI 10.1039/C2CS35384A.
- [20] Moore, E. B., de la Llave, E., Welke, K., Scherlis, D. A. & Molinero, V. Freezing, melting and structure of ice in a hydrophilic nanopore. *Phys. Chem. Chem. Phys.* **12**, 4124–4134 (2010). URL <http://dx.doi.org/10.1039/B919724A>. DOI 10.1039/B919724A.
- [21] Laio, A. & Gervasio, F. L. Metadynamics: a method to simulate rare events and reconstruct the free energy in biophysics, chemistry and material science. *Reports on Progress in Physics* **71**, 126601 (2008). URL <http://stacks.iop.org/0034-4885/71/i=12/a=126601>.
- [22] Meuler, A. J. *et al.* Relationships between water wettability and ice adhesion. *ACS Applied Materials & Interfaces* **2**, 3100–3110 (2010). URL <http://dx.doi.org/10.1021/am1006035>. DOI 10.1021/am1006035. PMID: 20949900, <http://dx.doi.org/10.1021/am1006035>.
- [23] Marrink, S.-J., Berger, O., Tieleman, P. & Jähnig, F. Adhesion forces of lipids in a phospholipid membrane studied by molecular dynamics simulations. *Biophysical Journal* **74**, 931 – 943 (1998). URL <http://www.sciencedirect.com/science/article/pii/S0006349598740160>. DOI [http://dx.doi.org/10.1016/S0006-3495\(98\)74016-0](http://dx.doi.org/10.1016/S0006-3495(98)74016-0).
- [24] Beck, J. S. *et al.* A new family of mesoporous molecular sieves prepared with liquid crystal templates. *Journal of the American Chemical Society* **114**, 10834–10843 (1992). URL <http://dx.doi.org/10.1021/ja00053a020>. DOI 10.1021/ja00053a020. <http://dx.doi.org/10.1021/ja00053a020>.
- [25] Wang, L., Han, X., Li, J., Zheng, D. & Qin, L. Modified mcm-41 silica spheres filled polydimethylsiloxane membrane for dimethylcarbonate/methanol separation via pervaporation. *Journal of Applied Polymer Science* **127**, 4662–4671 (2013). URL <http://dx.doi.org/10.1002/app.38046>. DOI 10.1002/app.38046.

- [26] Ding, N. *et al.* Partitioning mof-5 into confined and hydrophobic compartments for carbon capture under humid conditions. *Journal of the American Chemical Society* **138**, 10100–10103 (2016). URL <http://dx.doi.org/10.1021/jacs.6b06051>. DOI 10.1021/jacs.6b06051. PMID: 27477091, <http://dx.doi.org/10.1021/jacs.6b06051>.
- [27] Gadipelli, S., Patel, H. A. & Guo, Z. An ultrahigh pore volume drives up the amine stability and cyclic co₂ capacity of a solid-amine@carbon sorbent. *Advanced Materials* **27**, 4903–4909 (2015). URL <http://dx.doi.org/10.1002/adma.201502047>. DOI 10.1002/adma.201502047.
- [28] Plimpton, S. Fast parallel algorithms for short-range molecular dynamics. *Journal of Computational Physics* **117**, 1 – 19 (1995). URL <http://www.sciencedirect.com/science/article/pii/S002199918571039X>. DOI <http://dx.doi.org/10.1006/jcph.1995.1039>.
- [29] Gangtao Liang and Issam Mudawar. Review of spray cooling – part 2: High temperature boiling regimes and quenching applications. *International Journal of Heat and Mass Transfer*, 115:1206 – 1222, 2017.
- [30] Ivan U. Vakarelski, Jeremy O. Marston, Derek Y. C. Chan, and Sigurdur T. Thoroddsen. Drag reduction by leidenfrost vapor layers. *Phys. Rev. Lett.*, 106:214501, May 2011.
- [31] Ali Hashmi, Yuhao Xu, Benjamin Coder, Paul A. Osborne, Jonathon Spafford, Grant E. Michael, Gan Yu, and Jie Xu. Leidenfrost levitation: beyond droplets. *Scientific Reports*, 2:797 EP –, 11 2012.
- [32] Gary G Wells, Rodrigo Ledesma-Aguilar, Glen McHale, and Khellil Sefiane. A sublimation heat engine. *Nature Communications*, 6:6390, 03 2015.
- [33] Hyuk-min Kwon, James C. Bird, and Kripa K. Varanasi. Increasing leidenfrost point using micro-nano hierarchical surface structures. *Applied Physics Letters*, 103(20):201601, 2018/07/12 2013.
- [34] N. Zuber. On the stability of boiling heat transfer. *Trans. Am. Soc. Mech. Engrs.*, Vol: 80, 4 1958.
- [35] P. J. Berenson. Film-boiling heat transfer from a horizontal surface. *Journal of Heat Transfer*, 83(3):351–356, 08 1961.

- [36] V.P. Carey. *Liquid Vapor Phase Change Phenomena: An Introduction to the Thermophysics of Vaporization and Condensation Processes in Heat Transfer Equipment*. Taylor & Francis, 1992.
- [37] P. Spiegler, J. Hopenfeld, M. Silberberg, C. F. Bumpus, and A. Norman. Onset of stable film boiling and the foam limit. *International Journal of Heat and Mass Transfer*, 6(11):987–989, 1963.
- [38] Arthur W Adamson. Potential distortion model for contact angle and spreading. ii. temperature dependent effects. *Journal of Colloid and Interface Science*, 44(2):273–281, 1973.
- [39] A. Segev and S. G. Bankoff. The role of adsorption in determining the minimum film boiling temperature. *International Journal of Heat and Mass Transfer*, 23(5):637–642, 1980.
- [40] Eskil Aursand, Stephen H. Davis, and Tor Ytrehus. Thermocapillary instability as a mechanism for film boiling collapse. 852:283–312, 2018.
- [41] Seol Ha Kim, Ho Seon Ahn, Joonwon Kim, Massoud Kaviany, and Moo Hwan Kim. Dynamics of water droplet on a heated nanotubes surface. *Applied Physics Letters*, 102(23):233901, 2019/04/16 2013.
- [42] Corey Kruse, Troy Anderson, Chris Wilson, Craig Zuhlke, Dennis Alexander, George Gogos, and Sidy Ndao. Extraordinary shifts of the leidenfrost temperature from multiscale micro/nanostructured surfaces. *Langmuir*, 29(31):9798–9806, 08 2013.
- [43] K. J. Baumeister and F. F. Simon. Leidenfrost temperature—its correlation for liquid metals, cryogenes, hydrocarbons, and water. *Journal of Heat Transfer*, 95(2):166–173, 05 1973.
- [44] Adam Huang and Daniel D. Joseph. Instability of the equilibrium of a liquid below its vapour between horizontal heated plates. 242:235–247, 1992.
- [45] L.C. Burmeister. *Convective Heat Transfer*. Wiley-Interscience publication. Wiley, 1993.
- [46] Anne-Laure Biance, Christophe Clanet, and David Quéré. Leidenfrost drops. *Physics of Fluids*, 15(6):1632–1637, 2018/07/04 2003.
- [47] Son G, Dhir VK (1998) Numerical Simulation of Film Boiling Near Critical Pressures With a Level Set Method. *Journal of Heat Transfer* 120(1):183–192.

- [48] L M. Mack. *Boundary-layer linear stability theory*, volume -1. 05 1984.
- [49] H L Reed, W S Saric, and D Arnal. Linear stability theory applied to boundary layers. *Annual Review of Fluid Mechanics*, 28(1):389–428, 2019/06/08 1996.
- [50] Hans Lyklema and J. Lyklema. *3 - Pair Interactions*, volume 4, pages 3–1–3–190. Academic Press, 2005.
- [51] Sean Eichenlaub, Carly Chan, and Stephen P. Beaudoin. Hamaker constants in integrated circuit metalization. *Journal of Colloid and Interface Science*, 248(2):389–397, 2002.
- [52] Jacob N. Israelachvili. *Chapter 13 - Van der Waals Forces between Particles and Surfaces*, pages 253–289. Academic Press, San Diego, 2011.
- [53] Calum J. Drummond and Derek Y. C. Chan. van der waals interaction, surface free energies, and contact angles: Dispersive polymers and liquids. *Langmuir*, 13(14):3890–3895, 07 1997.
- [54] David B. Hough and Lee R. White. The calculation of hamaker constants from lift-shitz theory with applications to wetting phenomena. *Advances in Colloid and Interface Science*, 14(1):3–41, 1980.
- [55] E.W. Lemmon, M.O. McLinden, and D.G. Friend. *NIST Chemistry WebBook, NIST Standard Reference Database Number 69, Eds. P.J. Linstrom and W.G. Mallard*. Gaithersburg MD, 2012.
- [56] Korean thermophysical properties data bank. Chemical Engineering Research Information Center. <http://www.thermo.org/research/kdb/>
- [57] Amir Faghri and Yuwen Zhang. *Transport Phenomena in Multiphase Systems*, pages 954–1005. Academic Press, Boston, 2006.
- [58] Hyungdae Kim, Bao Truong, Jacopo Buongiorno, and Lin-Wen Hu. On the effect of surface roughness height, wettability, and nanoporosity on leidenfrost phenomena. *Applied Physics Letters*, 98(8):083121, 2018/06/27 2011.
- [59] Ivan U. Vakarelski, Neelesh A. Patankar, Jeremy O. Marston, Derek Y. C. Chan, and Sigurdur T. Thoroddsen. Stabilization of leidenfrost vapour layer by textured superhydrophobic surfaces. *Nature*, 489:274 EP –, 09 2012.

- [60] Guangming Liu and Vincent S J Craig. Macroscopically flat and smooth superhydrophobic surfaces: heating induced wetting transitions up to the leidenfrost temperature. *Faraday Discuss*, 146:141–151, 2010.
- [61] JoséM. Fernández-Varea and Rafael Garcia-Molina. Hamaker constants of systems involving water obtained from a dielectric function that fulfills the f sum rule. *Journal of Colloid and Interface Science*, 231(2):394–397, 2000.
- [62] Paul R. Jones, Chihpin (Andrew) Chuang, Tao Sun, Tom Y. Zhao, Kamel Fezzaa, Juan C. Takase, Dileep Singh, and Neelesh A. Patankar. High-speed x-ray imaging of the leidenfrost collapse. *Scientific Reports*, 9(1):1598, 2019.
- [63] Plimpton S (1995) Fast parallel algorithms for short-range molecular dynamics. *Journal of Computational Physics* 117(1):1 – 19.
- [64] Fabio L Leite, Carolina C Bueno, Alessandra L Da Róz, Ervino C Ziemath, and Osvaldo N Oliveira. Theoretical models for surface forces and adhesion and their measurement using atomic force microscopy. *International journal of molecular sciences*, 13(10):12773–12856, 10 2012.
- [65] J. D. Bernardin and I. Mudawar. The leidenfrost point: Experimental study and assessment of existing models. *Journal of Heat Transfer*, 121(4):894–903, 11 1999.
- [66] A A Mills and N F Sharrock. Rate of evaporation of n-alcohols from a hot surface: Nukiyama and leidenfrost temperatures. *European Journal of Physics*, 7(1):52, 1986.
- [67] A A Mills and J D Fry. Rate of evaporation of hydrocarbons from a hot surface: Nukiyama and leidenfrost temperatures. *European Journal of Physics*, 3(3):152, 1982.
- [68] H. Linke, B. J. Alemán, L. D. Melling, M. J. Taormina, M. J. Francis, C. C. Dow-Hygelund, V. Narayanan, R. P. Taylor, and A. Stout. Self-propelled leidenfrost droplets. *Phys. Rev. Lett.*, 96:154502, Apr 2006.
- [69] Ran Li, Zhongwei Huang, Xiaoguang Wu, Pengsen Yan, and Xianwei Dai. Cryogenic quenching of rock using liquid nitrogen as a coolant: Investigation of surface effects. *International Journal of Heat and Mass Transfer*, 119:446–459, 2018.
- [70] Juan J. Carbajo. A study on the rewetting temperature. *Nuclear Engineering and Design*, 84(1):21–52, 1985.
- [71] Niroh Nagai and Shigefumi Nishio. Leidenfrost temperature on an extremely smooth surface. *Experimental Thermal and Fluid Science*, 12(3):373–379, 1996.

- [72] Nishio Shigefumi. Prediction technique for minimum-heat-flux (mhf)-point condition of saturated pool boiling. *International Journal of Heat and Mass Transfer*, 30(10):2045–2057, 1987.
- [73] G. S. Emmerson and C. W. Snoek. The effect of pressure on the leidenfrost point of discrete drops of water and freon on a brass surface. *International Journal of Heat and Mass Transfer*, 21(8):1081–1086, 1978.
- [74] A. Sakurai, M. Shiotsu, and K. Hata. Effects of system pressure on minimum film boiling temperature for various liquids. *Experimental Thermal and Fluid Science*, 3(4):450–457, 1990.
- [75] Tom Y. Zhao, Paul R. Jones, and Neelesh A. Patankar. Thermodynamics of sustaining liquid water within rough icephobic surfaces to achieve ultra-low ice adhesion. *Scientific Reports*, 9(1):258, 2019.
- [76] Vishal Talari, Prakhar Behar, Yi Lu, Evan Haryadi, and Dong Liu. Leidenfrost drops on micro/nanostructured surfaces. *Frontiers in Energy*, 12(1):22–42, 2018.
- [77] P. J. Berenson. Film-boiling heat transfer from a horizontal surface. *Journal of Heat Transfer*, 83(3):351–356, 08 1961.
- [78] K. J. Baumeister and F. F. Simon. Leidenfrost temperature—its correlation for liquid metals, cryogenes, hydrocarbons, and water. *Journal of Heat Transfer*, 95(2):166–173, 05 1973.
- [79] V.P. Carey. *Liquid Vapor Phase Change Phenomena: An Introduction to the Thermophysics of Vaporization and Condensation Processes in Heat Transfer Equipment*. Taylor & Francis, 1992.
- [80] P.K. Kundu and I.M. Cohen. *Fluid Mechanics*. Elsevier Science, 2010.
- [81] Anne-Laure Bianco, Christophe Clanet, and David Quéré. Leidenfrost drops. *Physics of Fluids*, 15(6):1632–1637, 2018/07/04 2003.
- [82] Jones PR, Elliott AR, Patankar NA (2016) Sustaining superheated liquid within hydrophilic surface texture. *Langmuir* 32(48):12947–12953.
- [83] Shiomi J (2014) Nonequilibrium molecular dynamics methods for lattice heat conduction calculations. *Annual Review of Heat Transfer* 17:177–203.

- [84] Hadjiconstantinou NG (2006) The limits of navier-stokes theory and kinetic extensions for describing small-scale gaseous hydrodynamics. *Physics of Fluids* 18(11):111301.
- [85] Thomas Ederth. Computation of lifshitz-van der waals forces between alkylthiol monolayers on gold films. *Langmuir*, 17(11):3329–3340, 05 2001.
- [86] Fabio Villa, Marco Marengo, and Joël De Coninck. A new model to predict the influence of surface temperature on contact angle. *Scientific Reports*, 8(1):6549, 2018.
- [87] Skripov, V. P., Kondor, R., Slutzkin, D. (1974). *Metastable liquids* (Vol. 6). New York: Wiley.
- [88] Skripov, V. P., Sinitsyn, E. N., Pavlov, P. A., Ermakov, G. V., Muratov, G. N., Bulanov, N. V., Baidakov, V. G. (1988). Thermophysical properties of liquids in the metastable (superheated) state.
- [89] Skripov, V. P. (1992). Metastable states. *J. Non-Equilib. Thermodyn.*, 17(3), 193-236.
- [90] Bradfield, Walter S. “Liquid-solid contact in stable film boiling.” *Industrial & Engineering Chemistry Fundamentals* 5.2 (1966): 200-204.
- [91] H. Ohtake, Y. Koizumi, Study on propagative collapse of a vapor film in film boiling (mechanism of vapor-film collapse at wall temperature above the thermodynamic limit of liquid superheat), *Int. J. Heat Mass Transfer* 47 (2004) 1965–1977.
- [92] Zvirin, Y., R HEWITT, G., Kenning, D. B. R. (1990). Boiling on free-falling spheres: drag and heat transfer coefficients. *Experimental Heat Transfer*, 3(3), 185-214.
- [93] Yagov, V. V., Lexin, M. A., Zabiroy, A. R., & Kaban’kov, O. N. (2016). Film boiling of subcooled liquids. Part I: Leidenfrost phenomenon and experimental results for subcooled water. *International Journal of Heat and Mass Transfer*, 100, 908-917
- [94] Yagov, V. V., Zabiroy, A. R., Kaban’kov, O. N., & Minko, M. V. (2017). Heat transfer during cooling of high temperature spheres in subcooled water at different pressures. *International Journal of Heat and Mass Transfer*, 110, 219-230.
- [95] Yagov, V. V., Zabiroy, A. R., & Kanin, P. K. (2018). Heat transfer at cooling high-temperature bodies in subcooled liquids. *International Journal of Heat and Mass Transfer*, 126, 823-830.

- [96] H. Yeom, H. Jo, G. Johnson, K. Sridharan, M. Corradini, Transient pool boiling heat transfer of oxidized and roughened Zircaloy-4 surfaces during water quenching, *Int. J. Heat Mass Transf.* 120 (2018) 435–446.
- [97] Hyuk-min Kwon, James C. Bird, and Kripa K. Varanasi. Increasing leidenfrost point using micro-nano hierarchical surface structures. *Applied Physics Letters*, 103(20):201601, 2018/07/12 2013.
- [98] Velasco S, Santos M, White J (2015) Extended corresponding states expressions for the changes in enthalpy, compressibility factor and constant-volume heat capacity at vaporization. *The Journal of Chemical Thermodynamics* 85:68 – 76.
- [99] Morgan DL, Kobayashi R (1994) Extension of pitzer csp models for vapor pressures and heats of vaporization to long-chain hydrocarbons. *Fluid Phase Equilibria* 94:51 – 87.
- [100] Lienhard JH (1982) Corresponding States Correlations of the Spinodal and Homogeneous Nucleation Limits. *Journal of Heat Transfer* 104(2):379–381.
- [101] J. D. Bernardin and I. Mudawar. The leidenfrost point: Experimental study and assessment of existing models. *Journal of Heat Transfer*, 121(4):894–903, 11 1999.
- [102] Calum J. Drummond and Derek Y. C. Chan. van der waals interaction, surface free energies, and contact angles: Dispersive polymers and liquids. *Langmuir*, 13(14):3890–3895, 07 1997.
- [103] Paul R. Jones, Chihpin (Andrew) Chuang, Tao Sun, Tom Y. Zhao, Kamel Fezzaa, Juan C. Takase, Dileep Singh, and Neelesh A. Patankar. High-speed x-ray imaging of the leidenfrost collapse. *Scientific Reports*, 9(1):1598, 2019.
- [104] Plimpton S (1995) Fast parallel algorithms for short-range molecular dynamics. *Journal of Computational Physics* 117(1):1 – 19.
- [105] L.C. Burmeister. *Convective Heat Transfer*. Wiley-Interscience publication. Wiley, 1993.
- [106] Huber ML (2018) Models for viscosity, thermal conductivity, and surface tension of selected pure fluids as implemented in refprop v10.0.
- [107] Abdullah Alkhudhiri, Naif Darwish, and Nidal Hilal. Membrane distillation: A comprehensive review. *Desalination*, 287:2–18, 2012.

- [108] Ioan Sarbu and Calin Sebarchievici. A comprehensive review of thermal energy storage. *Sustainability*, 10(1), 2018.
- [109] Marco Simonelli, Nesma Aboulkhair, Mircea Rasa, Mark East, Christopher Tuck, Ricky Wildman, Otto Salomons, and Richard Hague. Towards digital metal additive manufacturing via high-temperature drop-on-demand jetting. *Additive Manufacturing*, 30:100930, 10 2019.
- [110] Geoffrey W. Burr, Matthew J. Breitwisch, Michele Franceschini, Davide Garetto, Kailash Gopalakrishnan, Bryan Jackson, Bülent Kurdi, Chung Lam, Luis A. Las-tras, Alvaro Padilla, Bipin Rajendran, Simone Raoux, and Rohit S. Shenoy. Phase change memory technology. *Journal of Vacuum Science & Technology B*, 28(2):223–262, 2019/12/31 2010.
- [111] Damir Juric and Grétar Tryggvason. Computations of boiling flows. *International Journal of Multiphase Flow*, 24(3):387–410, 1998.
- [112] Vijay K. Dhir. Mechanistic Prediction of Nucleate Boiling Heat Transfer—Achievable or a Hopeless Task? *Journal of Heat Transfer*, 128(1):1–12, 10 2005.
- [113] V. K. Badam, V. Kumar, F. Durst, and K. Danov. Experimental and theoretical investigations on interfacial temperature jumps during evaporation. *Experimental Thermal and Fluid Science*, 32(1):276–292, 2007.
- [114] Elizaveta Ya. Gatapova, Irina A. Graur, Oleg A. Kabov, Vladimir M. Aniskin, Maxim A. Filipenko, Felix Sharipov, and Lounès Tadríst. The temperature jump at water –air interface during evaporation. *International Journal of Heat and Mass Transfer*, 104:800–812, 2017.
- [115] Ichiro Tanasawa, James P. Hartnett, Thomas F. Irvine, and Young I. Cho. *Advances in Condensation Heat Transfer*, volume 21, pages 55–139. Elsevier, 1991.
- [116] C. A. Ward and D. Stanga. Interfacial conditions during evaporation or condensation of water. *Phys. Rev. E*, 64:051509, Oct 2001.
- [117] Roderick Dewar. Information theory explanation of the fluctuation theorem, maximum entropy production and self-organized criticality in non-equilibrium stationary states. 36(3):631–641, 2003.
- [118] Robert K Niven. Minimization of a free-energy-like potential for non-equilibrium flow systems at steady state. *Philosophical transactions of the Royal Society of London. Series B, Biological sciences*, 365(1545):1323–1331, 05 2010.

- [119] Berkeley CA (United States). Dept. of Mechanical Engineering) Carey, V. P. (California Univ. *Liquid-vapor phase-change phenomena*. New York, NY (United States); Hemisphere Publishing, United States, 1992.
- [120] J. M. Delhaye. Jump conditions and entropy sources in two-phase systems. local instant formulation. *International Journal of Multiphase Flow*, 1(3):395–409, 1974.
- [121] L. Meinhold-Heerlein. Surface conditions for the liquid-vapor system, taking into account entropy production caused by mass and energy transport across the interface. *Phys. Rev. A*, 8:2574–2585, Nov 1973.
- [122] Álvarez ME, Bourouis M. Modelling of Coupled Heat and Mass Transfer in a Water-Cooled Falling-Film Absorber Working with an Aqueous Alkaline Nitrate Solution. *Energies*, 2021; 14(7):1804.
- [123] Tom Y. Zhao and Neelesh A. Patankar. The thermo-wetting instability driving leidenfrost film collapse. *Proceedings of the National Academy of Sciences*, page 201917868, 05 2020.
- [124] E.W. Lemmon, M.O. McLinden, and D.G. Friend. *NIST Chemistry WebBook, NIST Standard Reference Database Number 69*, Eds. P.J. Linstrom and W.G. Mallard. Gaithersburg MD, 2012.
- [125] L. M. Martyushev and V. D. Seleznev. Maximum entropy production principle in physics, chemistry and biology. *Physics Reports*, 426(1):1–45, 2006.
- [126] Leonid M. Martyushev. The maximum entropy production principle: two basic questions. *Philosophical Transactions of the Royal Society B: Biological Sciences*, 365(1545):1333–1334, 2020/07/24 2010.
- [127] G. W. Paltridge. The steady-state format of global climate. *Quarterly Journal of the Royal Meteorological Society*, 104(442):927–945, 2020/07/24 1978.
- [128] Vladislav V. Levchenko, Ronan Fleming, Hong Qian, and Daniel A. Beard. An annotated english translation of ‘kinetics of stationary reactions’ [m. i. temkin, dokl. akad. nauk sssr. 152, 156 (1963)], 2010.
- [129] Robert G. Endres. Entropy production selects nonequilibrium states in multistable systems. *Scientific Reports*, 7(1):14437, 2017.
- [130] Vincent Holten, David T. Limmer, Valeria Molinero, and Mikhail A. Anisimov. Nature of the anomalies in the supercooled liquid state of the mw model of water. *The Journal of Chemical Physics*, 138(17):174501, May 2013.

- [131] Tianbao Wang and Min Chen. Determining interface temperature during rapid freezing of supercooled water. *Journal of Aircraft*, 55(3):1269–1275, 2020/06/04 2017.
- [132] G. Fang and C. A. Ward. Temperature measured close to the interface of an evaporating liquid. *Phys. Rev. E*, 59:417–428, Jan 1999.
- [133] Fei Duan, C. A. Ward, V. K. Badam, and F. Durst. Role of molecular phonons and interfacial-temperature discontinuities in water evaporation. *Phys. Rev. E*, 78:041130, Oct 2008.
- [134] G. Fang and C. A. Ward. Examination of the statistical rate theory expression for liquid evaporation rates. *Phys. Rev. E*, 59:441–453, Jan 1999.
- [135] C A Ward and Fei Duan. Turbulent transition of thermocapillary flow induced by water evaporation. *Phys Rev E Stat Nonlin Soft Matter Phys*, 69(5 Pt 2):056308, May 2004.
- [136] M. L. Huber, R. A. Perkins, D. G. Friend, J. V. Sengers, M. J. Assael, I. N. Metaxa, K. Miyagawa, R. Hellmann, and E. Vogel. New international formulation for the thermal conductivity of h₂o. *Journal of Physical and Chemical Reference Data*, 41(3):033102, 2020/06/28 2012.
- [137] W. Wagner and A. Pruß. The iapws formulation 1995 for the thermodynamic properties of ordinary water substance for general and scientific use. *Journal of Physical and Chemical Reference Data*, 31(2):387–535, 2020/06/28 2002.
- [138] L M Martyushev, A S Nazarova, and V D Seleznev. On the problem of the minimum entropy production in the nonequilibrium stationary state. *Journal of Physics A: Mathematical and Theoretical*, 40(3):371–380, dec 2006.
- [139] Steve Plimpton. Fast parallel algorithms for short-range molecular dynamics. *Journal of Computational Physics*, 117(1):1 – 19, 1995.
- [140] Tom Y. Zhao, Paul R. Jones, and Neelesh A. Patankar. Thermodynamics of sustaining liquid water within rough icephobic surfaces to achieve ultra-low ice adhesion. *Scientific Reports*, 9(1):258, 2019.
- [141] Junichiro Shiomi. Nonequilibrium molecular dynamics methods for lattice heat conduction calculations. *Annual Review of Heat Transfer*, 17:177–203, 01 2014.
- [142] M. L. Huber and R. A. Perkins. Thermal conductivity correlations for minor constituent fluids in natural gas: n-octane, n-nonane and n-decane. *Fluid Phase Equilibria*, 227(1):47–55, 2005.

- [143] M. McLinden and J. Splett. Certification report for srm 2214: Density of iso-octane for extended ranges of temperature and pressure, 2016-10-17 2016.
- [144] Andrew M Jersey and David M Foster. *Cerebral Aneurysm*. Northwell Health; North Shore University Hospital, Jan 2020.
- [145] Dan Laukka, Emily Pan, Terhi Fordell, Kemal Alpay, Melissa Rahi, Jussi Hirvonen, Jaakko Rinne, and Jarmo Gunn. Prevalence of thoracic aortic aneurysms and dilatations in patients with intracranial aneurysms. *J Vasc Surg*, 70(6):1801–1808, Dec 2019.
- [146] Xi Li, Ge Zhao, Jian Zhang, Zhiquan Duan, and Shijie Xin. Prevalence and trends of the abdominal aortic aneurysms epidemic in general population—a meta-analysis. *PLoS One*, 8(12):e81260, 2013.
- [147] G Johansson, U Markström, and J Swedenborg. Ruptured thoracic aortic aneurysms: a study of incidence and mortality rates. *J Vasc Surg*, 21(6):985–988, Jun 1995.
- [148] Michael Gawenda and Jan Brunkwall. Ruptured abdominal aortic aneurysm: the state of play. *Dtsch Arztebl Int*, 109(43):727–732, Oct 2012.
- [149] Gregory A Kuzmik, Adam X Sang, and John A Elefteriades. Natural history of thoracic aortic aneurysms. *J Vasc Surg*, 56(2):565–571, Aug 2012.
- [150] M A Coady, J A Rizzo, G L Hammond, G S Kopf, and J A Elefteriades. Surgical intervention criteria for thoracic aortic aneurysms: a study of growth rates and complications. *Ann Thorac Surg*, 67(6):1922–1926, Jun 1999.
- [151] Investigators MA3RS Study. Aortic wall inflammation predicts abdominal aortic aneurysm expansion, rupture, and need for surgical repair. *Circulation*, 136(9):787–797, Aug 2017.
- [152] Sarah Geisbüsch, Angelina Stefanovic, Deborah Schray, Irina Oyfe, Hung-Mo Lin, Gabriele Di Luozzo, and Randall B Griep. A prospective study of growth and rupture risk of small-to-moderate size ascending aortic aneurysms. *J Thorac Cardiovasc Surg*, 147(1):68–74, Jan 2014.
- [153] Anirudh Chandrashekar, Ashok Handa, Pierfrancesco Lapolla, Natesh Shivakumar, Elisha Ngetich, Vicente Grau, and Regent Lee. Prediction of abdominal aortic aneurysm growth using geometric assessment of computerised tomography images acquired during the aneurysm surveillance period. *Annals of Surgery*, Publish Ahead of Print, 2020.

- [154] Kenichiro Hirata, Takeshi Nakaura, Masataka Nakagawa, Masafumi Kidoh, Seitaro Oda, Daisuke Utsunomiya, and Yasuyuki Yamashita. Machine learning to predict the rapid growth of small abdominal aortic aneurysm. *J Comput Assist Tomogr*, 44(1):37–42, Jan/Feb 2020.
- [155] Karim Azer and Charles S Peskin. A one-dimensional model of blood flow in arteries with friction and convection based on the womersley velocity profile. *Cardiovasc Eng*, 7(2):51–73, Jun 2007.
- [156] Xiao-Fei Wang, Shohei Nishi, Mami Matsukawa, Arthur Ghigo, Pierre-Yves Lagrée, and Jose-Maria Fullana. Fluid friction and wall viscosity of the 1d blood flow model. *Journal of Biomechanics*, 49(4):565–571, 2016.
- [157] J R WOMERSLEY. Method for the calculation of velocity, rate of flow and viscous drag in arteries when the pressure gradient is known. *The Journal of physiology*, 127(3):553–563, 03 1955.
- [158] X. He, D. N. Ku, and J. E. Moore. Simple calculation of the velocity profiles for pulsatile flow in a blood vessel using mathematica. *Annals of Biomedical Engineering*, 21(5):557–558, 1993.
- [159] Seda Aslan, Paige Mass, Yue-Hin Loke, Linnea Warburton, Xiaolong Liu, Narutoshi Hibino, Laura Olivieri, and Axel Krieger. Non-invasive prediction of peak systolic pressure drop across coarctation of aorta using computational fluid dynamics. *Annual International Conference of the IEEE Engineering in Medicine and Biology Society. IEEE Engineering in Medicine and Biology Society. Annual International Conference*, 2020:2295–2298, 07 2020.
- [160] Ethel M Frese, Ann Fick, and H Steven Sadowsky. Blood pressure measurement guidelines for physical therapists. *Cardiopulmonary physical therapy journal*, 22(2):5–12, 06 2011.
- [161] Paul M. Lion. Stability of linear periodic systems. *Journal of the Franklin Institute*, 281(1):27–40, 1966.
- [162] Yinji Ma, Jungil Choi, Aurélie Hourlier-Fargette, Yeguang Xue, Ha Uk Chung, Jong Yoon Lee, Xiufeng Wang, Zhaoqian Xie, Daeshik Kang, Heling Wang, Seungyong Han, Seung-Kyun Kang, Yisak Kang, Xinge Yu, Marvin J. Slepian, Milan S. Raj, Jeffrey B. Model, Xue Feng, Roozbeh Ghaffari, John A. Rogers, and Yonggang Huang. Relation between blood pressure and pulse wave velocity for human arteries. *Proceedings of the National Academy of Sciences*, 115(44):11144, 10 2018.

- [163] L. Xie, S. Baguet, B. Prabel, and R. Dufour. Bifurcation tracking by harmonic balance method for performance tuning of nonlinear dynamical systems. *Mechanical Systems and Signal Processing*, 88:445–461, 2017.
- [164] T. Y. Zhao and N. A. Patankar. The thermo-wetting instability driving leidenfrost film collapse. *Proceedings of the National Academy of Sciences*, 117(24):13321, 06 2020.
- [165] J Bock, BW Kreher, Jürgen Hennig, and Michael Markl. Optimized pre-processing of time-resolved 2d and 3d phase contrast mri data. In *Proceedings of the 15th Annual meeting of ISMRM, Berlin, Germany*, page 3138, Berlin, Federal Republic of Germany, 2007.
- [166] Aslan S, Mass P, Loke YH, Warburton L, Liu X, Hibino N, Olivieri L, Krieger A. Non-invasive Prediction of Peak Systolic Pressure Drop across Coarctation of Aorta using Computational Fluid Dynamics. *Annu Int Conf IEEE Eng Med Biol Soc.* 2020 Jul;2020:2295-2298.
- [167] Markl, M., Wallis, W., Brendecke, S., Simon, J., Frydrychowicz, A. and Harloff, A. Estimation of global aortic pulse wave velocity by flow-sensitive 4D MRI. *Magn. Reson. Med.*, 63: 1575-1582, 2010
- [168] Kuijpers JM, Mulder BJ. Aortopathies in adult congenital heart disease and genetic aortopathy syndromes: management strategies and indications for surgery. *Heart.* 2017 Jun;103(12):952-966.
- [169] Mandrekar JN. Receiver operating characteristic curve in diagnostic test assessment. *J Thorac Oncol.* 2010 Sep;5(9):1315-6
- [170] Staarmann B, Smith M, Prestigiacomo CJ. Shear stress and aneurysms: a review. *Neurosurg Focus.* 2019 Jul 1;47(1):E2.
- [171] K. E. Boczar, K. Cheung, M. Boodhwani, L. Beauchesne, C. Dennie, S. Nagpal, K. Chan, and T. Coutinho. Sex differences in thoracic aortic aneurysm growth. *Hypertension*, 73(1):190–196, 2021/08/06 2019.